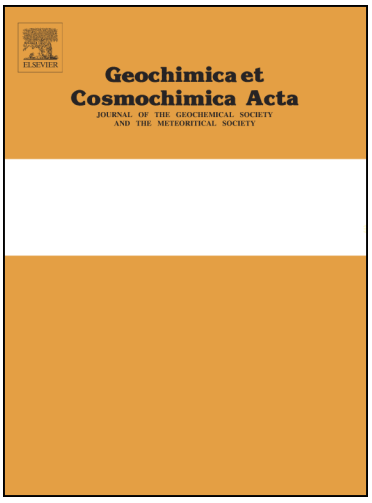

Petrology and oxygen isotopic composition of large igneous inclusions in ordinary chondrites: Early solar system igneous processes and oxygen reservoirs

Alex M. Ruzicka, Richard C. Greenwood, Katherine Armstrong, Kristy L. Schepker, Ian A. Franchi

PII: S0016-7037(19)30030-4
DOI: https://doi.org/10.1016/j.gca.2019.01.017
Reference: GCA 11090

To appear in: *Geochimica et Cosmochimica Acta*

Received Date: 3 October 2018
Accepted Date: 9 January 2019

Please cite this article as: Ruzicka, A.M., Greenwood, R.C., Armstrong, K., Schepker, K.L., Franchi, I.A., Petrology and oxygen isotopic composition of large igneous inclusions in ordinary chondrites: Early solar system igneous processes and oxygen reservoirs, *Geochimica et Cosmochimica Acta* (2019), doi: https://doi.org/10.1016/j.gca.2019.01.017

Petrology and oxygen isotopic composition of large igneous inclusions in ordinary chondrites: Early solar system igneous processes and oxygen reservoirs*

Alex M. Ruzicka[1], Richard C. Greenwood[2], Katherine Armstrong[1,3], Kristy L. Schepker[1], Ian A. Franchi[2]

[1] Portland State University, Department of Geology and Cascadia Meteorite Laboratory, 17 Cramer Hall, 1721 SW Broadway, Portland, OR, USA (Corresponding author)

[2] Planetary Sciences Research Institute, The Open University, Walton Hall, Milton Keynes, MK7 6AA, UK

[3] Now at: Universität Bayreuth, Bayrisches Geoinstitut, D-95440, Bayreuth, DE

January 8, 2018

*Paper dedicated to the memory of Lawrence A. Taylor

Abstract. Large (>3.5 mm and up to 4 cm across) igneous inclusions poor in metal and sulfide are a minor but not uncommon component in ordinary chondrites, and have implications for the nature of physiochemical and melting processes in the early solar system. We obtained petrographic-chemical data for forty-two large igneous inclusions in ordinary chondrites of various groups (H, L, LL) and petrographic types (3-6) and oxygen isotope data for a subset of twelve of these inclusions and their host chondrites. Different inclusions formed both before and after the thermal metamorphism experienced by their host chondrites. The bulk chemical compositions of the inclusions vary broadly around whole-rock chondrite composition, comprise four main chemical types and some other variants, and show little evidence of having formed as igneous differentiates. Oxygen isotope compositions overlap ordinary chondrite compositions and are related to inclusion chemical type. Most prevalent in type 3 and 4 chondrites are inclusions, often droplets, of the vapor-fractionated (*Vfr*) chemical type, either enriched in refractory lithophile elements, or depleted in volatile lithophile elements, or both. These inclusions have low $\Delta^{17}O$ (~0.1-0.6‰) and high $\delta^{18}O$ (~4-8‰) values and formed in reservoirs with $\Delta^{17}O$ lower than their hosts, primarily as evaporative melts and mixtures that probably experienced kinetic isotopic fractionation. Another chemical type (*Unfr+K*) has unfractionated abundances of lithophile elements except for being strongly enriched in K, a signature also found in some impact melts from melt rocks and melt breccias. These inclusions formed by impact melting of chondritic material and accompanying K enrichment. Inclusions with unfractionated (*Unfr*) lithophile element abundances are present in type 3-6 chondrites and are prevalent in type 5 and 6. Some are spatially associated with coarse metal-sulfide nodules in the chondrites and likely formed by *in situ* impact melting. Others were melted prior to thermal metamorphism and were chemically but not isotopically homogenized during metamorphism; they are xenoliths that formed in oxygen reservoirs different than the hosts in which they were metamorphosed. The latter inclusions provide evidence for nebular or collisional mixing of primitive materials prior to thermal metamorphism of

asteroid bodies, including transport of H-like source materials to the L body, LL-like source materials to the L body, and low-$\Delta^{17}O$ materials to the LL body. Feldspar-rich (*FldR*) inclusions have compositions similar to melt pockets and could have formed by disequilibrium melting and concentration of feldspar during an impact event to form large droplets or large masses. Overall, the results of this study point to important and varied roles for both "planetary" impact melting and "nebular" evaporative melting processes to form different large igneous inclusions in ordinary chondrites. Chondrules may have formed by processes similar to those inferred for large inclusions, but there are important differences in the populations of these objects.

1. INTRODUCTION

Light or dark colored inclusions that have igneous textures, low metal and sulfide contents, and which are unusually large (up to 4 cm across) compared to chondrules, are a distinctive, but not uncommon component in ordinary chondrites. They have been variably described as macrochondrules (Binns, 1967; Bridges and Hutchison, 1997; Weyrauch and Bischoff, 2012), megachondrules (Ruzicka et al., 1998), large igneous clasts or fragments (Fodor and Keil, 1975; Rubin et al., 1981; Wlotzka et al., 1983; Bridges and Hutchison, 1997; Ruzicka et al., 1995, 1998; Crowther et al., 2018), melt rock clasts (Fodor et al., 1980; Keil et al., 1980; Rubin et al., 1983a, b; Rubin, 1985; Metzler et al., 2011), pebbles (Hutchison et al., 1988), large igneous-textured enclaves (LITEs, Jamsja and Ruzicka, 2010), or simply and generically, inclusions (Yanai et al., 1983; Sack et al., 1994; Nakamura et al., 1994; Ruzicka et al., 2000, 2012a).

Three different mechanisms have been proposed for the origin of inclusions. This includes: (1) formation as unusually large chondrules (Binns, 1967; Bridges and Hutchison, 1997; Ruzicka et al., 1998, 2000; Weyrauch and Bischoff, 2012); (2) formation as impact melts (Fodor and Keil, 1975; Fodor et al., 1980; Keil et al., 1980; Rubin et al., 1981, 1983; Wlotzka et al., 1983; Rubin, 1985; Bridges and Hutchison, 1997; Ruzicka et al., 1998, 2000; Jamsja and Ruzicka, 2010); and (3)

formation as igneous differentiates (Hutchison et al., 1988; Kennedy et al., 1992; Sack et al., 1994; Bridges et al., 1994, 1995; Ruzicka et al., 1995; 2012a; Bridges and Hutchison, 1997). A recent variant of the third model is derivation of inclusions from early, possibly substantially melted, asteroidal magmaspheres (Crowther et al., 2018). These formation mechanisms obviously have very different implications for physical and thermal processes.

The purpose of the present study was to better define the origin of large inclusions in ordinary chondrites, and their implications for igneous processes and oxygen isotope reservoirs in the early solar system, based on chemical-petrographic and oxygen isotope data. This report describes the largest dataset of chemical and oxygen isotope compositions for large inclusions to date, roughly doubling the number of inclusions previously analyzed for these properties, as summarized by Ruzicka et al. (2000). Preliminary work was reported by Armstrong (2014) and Ruzicka et al. (2016).

2. SAMPLES AND METHODS

Samples for study included forty-two inclusions ~3.5-20 mm across visible in exposed surfaces of H, L, and LL chondrites of various petrographic types (3-6), from which polished thin or thick sections and bulk samples were available or could be prepared (Table 1). No other selection criteria were applied, although effort was made to analyze especially large inclusions or those present in weakly-metamorphosed (type 3) chondrites. Three inclusions from three separate pieces of QUE 97008 (QUE-I1, QUE-I3, QUE-I4) and two inclusions from separate pieces of MET 00489 (MET-I1, MET-I2) (Table 1) were treated as potentially different lithologies. Virtually all of the inclusions are depleted in metal and sulfide (compared to the host chondrites), all are much larger than chondrules in the host meteorites, and all are igneous (most commonly microporphyritic) in texture. Samples from the Cascadia Meteorite Laboratory (CML), American Museum of Natural History (AMNH), and Johnson Spacecraft Center (JSC) Antarctic Meteorite collection were studied (Table 1). Various techniques were used. These included: optical microscopy (OM), scanning electron microscopy

(SEM), electron microprobe analysis (EMPA), and laser fluorination and mass spectrometry of bulk samples for analysis of oxygen isotopes. Bulk compositions were determined by modal reconstruction. Mean uncertainties in bulk compositions, including propagated uncertainties in both phase compositions and modes, are ~3-4% relative for Si and Mg, ~7-10% for FeO and Al, ~14-17% for Ca, Na, and Fe(metal), ~21-26% for Cr, Mn, P, S, and Fe(sulfide), ~32-34% for Ti and Ni, and ~42% for K. System precision (2σ) for $\delta^{17}O$, $\delta^{18}O$ and $\Delta^{17}O$ is ±0.05‰, ±0.09‰ and ±0.02‰, respectively. Further details about experimental techniques are provided in the Electronic Annex.

For comparison, metal-sulfide poor areas of impact melts in four chondrites were studied using OM-SEM methods identical to those used for inclusions. These include two melt rocks (NWA 6454 and NWA 6579) and two melt breccias (NWA 5964 and NWA 6580). NWA 6579 (sample CML 0358) is classified as an L-group melt rock based on both metal compositions (Garvie, 2012) and olivine compositions (this work). NWA 6454 (CML 0273) also was classified as an L-group melt rock based on metal compositions (Garvie, 2012), but based on olivine compositions (this work) it is more likely an H-group melt rock. NWA 5964 (CML 0175) is an L3-6 breccia with abundant impact melt, and NWA 6580 (CML 0371) contains abundant impact melt along with an L-group genomict breccia clast. In hand specimens, impact melt comprises ~100% of the NWA 6456 and NWA 6579 stones (300 g and 99 g, respectively), ~40% of the NWA 5964 stone (105 g), and ~95% of the NWA 6580 stone (also 105 g).

3. RESULTS

Table 1 summarizes sizes, textures, mineralogies, shapes (forms), ferromagnesian mineral Fe-Mg homogeneity, and chemical types for all forty-two inclusions studied by OM and SEM techniques. The average bulk compositions of various chemical types of inclusions is given in Table 2, and the bulk compositions of ordinary chondrite impact melts are compared to inclusions in Table 3. Oxygen isotope compositions for aliquots of sixteen inclusions and their hosts are presented in Table 4. More

details on textures, mineralogies, phase compositions, modal compositions, and bulk compositions of individual inclusions are given in the Electronic Annex (Tables A1, A2, A3). Additional data, including images for most of these inclusions, can be found elsewhere (Appendix A of Armstrong, 2014).

3.1 Bulk chemical fractionations and chemical types

Bulk chemical fractionations and chemical types of inclusions are described first as they provide a useful framework.

3.1.1 Chemical fractionations

Virtually all inclusions are depleted in partly siderophile-chalcophile elements compared to chondrite, and our data provide a good estimate of the extent of this depletion. The average (inclusion)/(L chondrite) concentration ratio of S, Fe(sulfide), Fe(metal), and Ni (Table 2) is 0.18, 0.18, 0.17, and 0.23, respectively. This implies that the average inclusion can be described by loss of ~80% sulfide and metal from an L chondrite composition.

In contrast, lithophile element abundances in inclusions are generally similar to chondrites, although there are some significant variations as described below. The average (inclusion)/(L chondrite) concentration ratio on a metal-and-sulfide-free basis is 1.0 within $\pm 1\sigma$ for all lithophiles (Si, Ti, Al, Cr, FeO, Mn, Mg, Ca, Na, and K) (Table 2). This implies inclusions as a whole have broadly chondritic silicate compositions. Even so, refractory elements (Al, Ti, Ca) are slightly enriched in average inclusion, and FeO and Na are slightly depleted in average inclusion, on a metal-and-sulfide-free basis compared to average L chondrite (Table 2). Thus, inclusions are slightly fractionated in lithophile elements.

The extent and nature of lithophile element fractionations vary for different inclusions. Among the forty-two inclusions studied, bulk compositions (Table A3) can be grouped into four main chemical types (each with multiple inclusions) as well as some other less common variants (Table 1).

3.1.2 Unfr chemical type

Thirteen inclusions are chemically similar to average ordinary chondrite and have relatively unfractionated lithophile element abundances (*Unfr* type, Fig. 1a, Table 2). Compared to average ordinary chondrite, the average compositions of *Unfr* inclusions are only slightly enriched in lithophile elements, and are significantly depleted in elements with chalcophile-siderophile tendency (Fig. 1a). These compositions can be readily explained by melting of ordinary chondrite followed by metal-sulfide loss, enriching the lithophiles slightly. In *Unfr* inclusions, average P and Fe abundances are similarly depleted compared to average ordinary chondrite (Fig. 1a), implying that both elements behaved in partly siderophile fashion during inclusion formation.

3.1.3 Unfr+K chemical type

Four inclusions have nearly unfractionated lithophile element abundances except for being strongly enriched in K_2O (0.23-0.99 wt%, *Unfr+K* type, Fig. 1b, Table 2). The composition of these *Unfr+K* inclusions are similar to some impact melts in L chondrite melt rocks and melt breccias (Fig. 1b, Table 3). The average K contents of the four *Unfr+K* inclusions and four impact melts studied are (coincidentally) identical, and indeed the average compositions for all lithophile and siderophile-chalcophile elements in both are the same within $\pm 1\sigma$ for all elements except Cr, which is only slightly lower in the inclusions (Fig. 1b, Table 3). In contrast, the average K content of all forty-two inclusions is only 22 ± 18% of that of the four impact melts (Table 3). This highlights the chemical distinctiveness of *Unfr+K* inclusions and their especially close chemical resemblance to definite impact melts.

3.1.4 Vfr chemical type

Most numerous (18 of 42 inclusions) are vapor-fractionated (*Vfr*) inclusions, which have lithophile element abundances that vary according to volatility (50% condensation temperatures). Compared to average ordinary chondrite, the average composition of all eighteen *Vfr* inclusions is

enriched in refractory elements (Al, Ti, Ca), near-chondritic in elements of intermediate volatility (Mg, Si, Cr, Mn), and progressively depleted in volatile Na and K (Fig. 1c). This implies that *Vfr inclusions or their precursor materials experienced either high-temperature condensation or evaporation*.

There is considerable variation in the compositions of *Vfr* inclusions. Five different subtypes can be identified. Like *Vfr* inclusions overall, the average *Vfr(mono)* subtype (six examples) shows a monotonic decrease in the abundances of progressively more volatile elements (Fig. 1e). In contrast, the average *Vfr(RE)* subtype (five examples) is significantly enriched (~3-5 x CI chondrite) in refractory elements (Al, Ti, Ca) only, and similar to ordinary chondrite abundances for other lithophile elements (Fig. 1f). This pattern suggests *Vfr(RE)* inclusions incorporate an excess of a refractory component. The average *Vfr(AD)* subtype (6 examples) is alkali depleted (~0.3-0.4 x CI chondrite), but otherwise similar to ordinary chondrite for elements of intermediate volatility (Si-Mn) and only somewhat enriched (~2 x CI chondrite) in more refractory elements such as Al, Ca and Mg (Fig. 1g). *Vfr(AD)* inclusions are notably less depleted in siderophile-chalcophile elements than other *Vfr* inclusions (Fig. 1e-g). Finally, the *Vfr(int)* subtype (one inclusion, Par-I2) has a bowed abundance pattern with maxima (~2 x CI chondrite) for elements of intermediate volatility (Si, Cr, Mn) and progressively lower abundances for both increasingly more volatile elements Na and K (to ~0.4 x CI chondrite) and increasingly more refractory elements Mg, Ca, Ti and Al (to ~1 x CI chondrite) (Fig. 1e). This suggests the concentration of an intermediate-volatility component. Thus, although all *Vfr* inclusions appear to have undergone vapor fractionation, the style of fractionation was not the same for different inclusions.

3.1.5 FldR chemical type

Four inclusions (*FldR* type) are rich in those elements that concentrate in feldspar, including Al, Ca, Na, and K (Fig. 1d). Three of these (4859-I4, 7870-I1, Etr-I1) are rich in plagioclase (~22-32 area%), whereas the fourth (Rgl-I1) is rich in feldspathic glass (~35 area%) (Table A2). They are also

enriched in Ti (Fig. 1d), which does not concentrate in feldspar but which is associated with it in the form of Ti-oxide (3 of 4 contain ilmenite, up to 0.2 area% in Rgl-I1) and Ti-bearing Ca-rich pyroxene (3 of 4 contain Ca-pyroxene, 3.1-5.2 area%) (Table A2).

3.1.6 Other chemical variants

The final three inclusions are represented by one member only. The abundance pattern for Tdk-I1 (*FldP* type) is somewhat complementary to feldspar-rich inclusions, being poor in those elements that concentrate in feldspar (Al, Na, K) (Fig. 1h). Unique Jgo-I1 is rich in both albitic feldspar and chromite (high Al, Cr, Na and K), and unlike most inclusions is not significantly depleted in metal (it has near-chondritic Ni, Fe, P) (Fig. 1h). The last inclusion (Obl-I1) is designated as chemically undefined, as it was located at the edge of section with a possibly larger part unsampled, and contains coarse olivine, features that could make the derived composition unrepresentative (Armstrong, 2014).

3.1.7 Normative compositions

The bulk compositions of the silicate-rich fractions of inclusions are expressed in terms of normative minerals in Fig. 2. *Normative compositions of inclusions cluster around ordinary chondrite composition and bear no relationship to cotectics or reaction boundaries* (Fig. 2). This is in contrast to three inclusions in Buzzard Coulee (H4) that were interpreted as igneous differentiates (Bz-1, Bz-2, Bz-3; Ruzicka et al., 2012a) (Fig. 2). The inclusions in this study instead more closely resemble the normative compositions of ferromagnesian chondrules in ordinary chondrites (Grossman et al., 1988).

Some inclusions are notably rich in normative plagioclase, including inclusions of the *FldR* type, *Vfr(RE)* type, and unique Jgo-I1 (Fig. 2). In this regard these compositions fall into the projected field of melt pockets, which are produced by localized shock melting (Stöffler et al., 1991) (Fig. 2). This is somewhat misleading, as the projection of Fig. 2 does not show differences in Na-Ca feldspar

proportions. *Vfr(RE)* inclusions are rich in Ca-feldspar component unlike most melt pockets; only *FldR* inclusions and Jgo-I1 are rich in Na-rich feldspar component similar to melt pockets.

FldP inclusion Tdk-I1 has less normative feldspar than other inclusions (Fig. 2). The normative olivine / orthopyroxene ratio for this inclusion overlaps that of ordinary chondrites (Fig. 2).

Other inclusions vary less in normative feldspar and more in normative olivine/pyroxene ratio, or lie close to chondrite compositions. For example, the normative compositions of *Unfr* and *Vfr(AD)* inclusions overlap each other, and vary in normative olivine/orthopyroxene at roughly chondritic normative plagioclase (Fig. 2). *Vfr(mono)* inclusions vary most in normative olivine and tend to be olivine-poor, whereas the *Vfr(int)* inclusion Par-I2 is the most orthopyroxene-normative inclusion (Fig. 2). Finally, *Unfr+K* inclusions and chondrite impact melts overlap in normative composition and lie close to bulk ordinary chondrite (Fig. 2).

3.1.8 Distribution of chemical types by petrographic types of hosts

Figure 3 shows the distribution of inclusion chemical types according to petrographic type of the host. *Type 3 and 4 chondrites are dominated by inclusions of the Vfr type and also contain inclusions of the Unfr, Unfr+K, and FldR types* (Fig. 3). The proportions of these inclusions are roughly the same in type 3 and 4 chondrites although the statistics are much better for type 3 (Fig. 3). *Type 5 and 6 chondrites are dominated by inclusions of the Unfr type* (in both type 5 and 6 hosts) and also contain *Vfr* (in type 5), *FldR* (in type 5), *FldP* (in type 5), the undefined Obl-I1 (in type 5), and the unique Jgo-I1 (in type 6) (Fig. 3).

3.2 Texture, mineralogy, phase compositions

The textures, mineralogies, and phase compositions of large inclusions are given in Table A1 and in more abbreviated form in Table 1. Representative images are shown in Fig. 4 (*Unfr* and *Unfr+K* inclusions) and Fig. 5 (*Vfr*, *FldR*, and Jgo-I1). Average olivine, pyroxene, and feldspar compositions are plotted in Fig. 6.

3.2.1 Texture and mineralogy

Inclusions contain phases typical of ordinary chondrites. This includes olivine, low-Ca pyroxene (sometimes of the clinoenstatite variety but more often orthopyroxene), calcic pyroxene (including pigeonite, augite, or diopside), plagioclase, more-or-less feldspathic glass, and accessory chromite, ilmenite, merrillite, Cl-apatite, troilite, and FeNi metal of differing Ni content. Rare minerals include Al-spinel (7869-I1), feldspathoid (partly replacing plagioclase in Lut-I1), and calcite weathering product in veins (7871-I1). Abundant feldspathic glass is not always restricted to inclusions in type 3 hosts, for example occurring in 4686-I1 (H4 host) and in 7873-I1 (H5-6) (Fig. 4c). Feldspathic glass occurs together with feldspar in Etr-I1 (L5 host). Some maskelynite (glass with plagioclase composition) appears to be present in 8232-I1, McK-I1, McK-I2, and PVM-I1, based on composition and smooth, crack-poor appearance described for maskleynite (Chen and El Goresy, 2000). Clinoenstatite is present in inclusions from type 3 and 4 chondrites, including Cyn-I1 (L4 host), Par-I2 (LL3.6 host), the three QUE inclusions (QUE-I1, QUE-I2, QUE-I3, L3.05 host), and in the cores of pyroxene grains in MET-I1 (L3.6 host). Pigeonite is present in inclusions from type 3 chondrites only (MET-I2, MET-I3, Par-I1, Par-I2, QUE-I1, QUE-I3, QUE-I4). Augite and diopside are widely present.

Textures in *Unfr* inclusions are dominated (10 of 13 examples) by variants of olivine microporphyries. Most typical are objects with equant olivine phenocrysts ~0.1-1 mm across, such as Arm-I1 (Fig. 4a). Finer-grained microporphyry variants have equant olivine phenocrysts typically ≤0.1 mm across, such as Glk-I1 (Fig. 4b). This inclusion also is internally brecciated, with glassy melt veins and melt pockets of mafic (rich in normative pyroxene) composition cross-cutting and enclosing regions with microporphyritic texture and more feldspathic mesostasis (Fig. 4b). 7873-I1 is a microporphry variant that has portions with spinifex-like texture (elongate and intersecting olivine

phenocrysts) (Fig. 4c). Other textures shown by *Unfr* inclusions include cryptocrystalline (Par-I3), barred olivine-pyroxene (Obl-I2), and skeletal olivine-pyroxene (7871-I1).

Margins of these inclusions are varied, and can appear broken, marked by a shock vein (e.g., Glk-I1, 7873-I1), or containing internal rims of pyroxene, pyroxene + troilite, pyroxene + olivine, olivine + feldspar, feldspar + chromite, or in the case of Obl-I2, a curved olivine shell similar to that typically observed in barred olivine chondrules. Glk-I1 has a rounded margin and was described as an unusually large chondrule by Prinz et al. (1988), but it is entirely bounded by shock veins, has what appears to be a brecciated margin, and shows no internal textural features suggestive of crystallization as a droplet. This suggests Glk-I1 is best described as a rounded clast. Among *Unfr* inclusions, only Obl-I2 is interpreted as being clearly a droplet, and has a texture similar to barred olivine chondrules except on a coarser scale.

A noteworthy feature of some Unfr inclusions is their association with coarse (1-7 mm across), compact metal or troilite nodules or grains. Coarse metal-sulfide nodules are located in the host adjacent to *Unfr* inclusions PVM-I1 (Hutson et al., 2013) and 7873-I1 (Fig. 4c). A coarse troilite nodule is located in Oberlin not far from Obl-I1 and Obl-I2, and coarse sulfide is present in NWA 4859 (Jamsja and Ruzicka, 2010), not far from 4859-I18 (*Unfr* inclusion) and 4859-I4 (*FldR* inclusion). Rounded coarse metal-sulfide nodules are also present *within* Glk-I1 and 4859-I18.

There are four examples of *Unfr+K* inclusions. 869-I1 is a fine-grained olivine microporphyry (Fig. 4d), whereas MET-I2 and Dim-I1 (Fig. 4e) are somewhat coarser olivine microporphyries. All chiefly contain olivine phenocrysts set in glassy mesostases. Dim-I1 also contains sub-millimeter domains with granular olivine or barred olivine textures, as well as a ~2 x 3-mm-diameter, sharply-defined, type 3 chondrite clast apparently deep within its interior. 8231-I1 occurs in multiple pieces in NWA 8231. The main portion contains olivine poikilitically enclosed in coarser (~0.5 mm across) low-Ca pyroxene oikocrysts, with areas interstitial to the oikocrysts containing fine-grained olivine,

augite, plagioclase, troilite and phosphate (Fig. 4f). Augite tends to be located in finer-grained portions at the edges of the oikocrysts. Chondrite patches occur deep within the main portion of 8231-I1, and one rounded coarse (~1 x 1.5 mm diameter) metal nodule is present within the inclusion near its margin. All of these inclusions have brecciated margins (e.g., Dim-I1, Fig. 4e; 869-I1, top of Fig. 4d), but in one location, 869-I1 appears to merge into the host and engulf chondrules in an apparently intrusive contact (right of Fig. 4d). 869-I1 is located adjacent to a shock-blackened (metal-and-troilite inclusion-rich) area.

The textures of all *Unfr+K* inclusions and some *Unfr* inclusions such as Glk-I1 are similar to those observed in the four chondrite impact melts studied. Impact melts in NWA 5964, NWA 6454, and NWA 6580 are fine-grained olivine microporphyries with olivine phenocrysts set in glassy mesostasis, similar to the textures of 869-I1, MET-I2, Dim-I1, and Glk-I1. The olivine phenocryst grain sizes in 869-I1 and Glk-I1 (≤100 μm across) are especially similar to the impact melts. NWA 6579 impact melt contains regions of coarser (~0.1-0.2 mm across) low-Ca pyroxene oikocrysts that poikilitically enclose olivine and are zoned to Ca-rich margins, with areas interstitial to low-Ca pyroxene containing fine-grained olivine and feldspar, similar to the texture of 8231-I1.

All of the impact melts contain coarse metal-sulfide nodules, reminiscent of the nodules found within inclusions 8231-I1, Glk-I1, 4859-I18, and close to PVM-I1 and 7873-I1. NWA 5964 impact melt further contains chondrite patches deep within melt areas, similar to Dim-I1 and 8231-I1.

Vfr inclusions have highly varied textures. They include microporphyritic olivine (Fig. 5a) and finer-grained variants, microporphyritic pyroxene (Fig. 5a) and finer-grained varieties, microporphyritic olivine-pyroxene (mode olivine > pyroxene) or microporphyritic pyroxene-olivine (olivine < pyroxene), porphyritic olivine-pyroxene with some olivine grains > 1 mm across (Fig. 5c), poikilitic pyroxene-olivine (Fig. 5d), fine skeletal olivine (Fig. 5b) or skeletal olivine-pyroxene, cryptocrystalline, and fine granular olivine. Some inclusions have a hybrid texture, including

microporphyritic pyroxene – barred olivine, barred olivine with granular olivine rim, and skeletal olivine-pyroxene with granular olivine rim. There is no obvious difference in texture-mineralogy for different *Vfr* subtypes.

Vfr inclusions contain a larger proportion of drop-formed objects than other inclusion types. Such drop-formed inclusions have not only a predominantly curved margin but also internal textures with radial or concentric arrangements of minerals that suggest they crystallized as molten droplets. These droplets have a variety of chemical types and textures. Examples include Rfd-I1 (*Vfr(mono)*, fine skeletal olivine-pyroxene with granular pyroxene rim; Fig. 5b) and Par-I2 (*Vrf(int)*, microporphyritic pyroxene, with olivine enclosed in pyroxene; Fig. 5a). Other drop-formed inclusions are 7869-I1 (*Vfr(AD)*, fine granular olivine with pyroxene-rich rim), 7872-I1 (*Vfr(RE)*, barred olivine with granular olivine rim), KrC-I1 (*Vfr(RE)*, cryptocrystalline), and Lut-I1 (*Vfr(mono)*, fine skeletal olivine-pyroxene with granular olivine rim). The drop-formed *Vfr* inclusions are good examples of what can be termed "macrochondrules" (Bridges and Hutchison, 1997; Weyrauch and Bischoff, 2012) or "megachondrules" (Ruzicka et al., 1998). Other *Vfr* inclusions show less evidence of having crystallized as droplets but do contain rims of different mineralogy or texture. This includes for example Par-I1, which contains low-Ca pyroxene along only its edge (Fig. 5a). In detail the margin of Par-I1 is broken and some of the low-Ca pyroxene as well as other portions appear to have been removed. However, the presence of a partial rim suggests that only mild brecciation affected Par-I1. Other *Vfr* inclusions with rims include 4872-I1 (granular olivine rim) and McK-I2 (pyroxene rim). *Vfr* inclusions such as these may have formed as droplets.

Most *Vfr* inclusions, like other inclusions, have irregularly-shaped or clearly broken margins. QUE-I4 is noteworthy not only for obvious broken margins but also for containing internal breccia contacts, along which changes in texture occur (Fig. 5c). Microfaults also occur elsewhere in the

inclusion, which truncate zoned pyroxene grains but which do not appear to cross-cut the adjacent feldspathic mesostasis (Fig. 5c).

The four *FldR* inclusions show a variety of textures. This includes porphyritic olivine (Etr-I1, Fig. 5e), microporphyritic olivine-pyroxene (4859-I4), fine microporphyritic olivine (Rgl-I1), and skeletal olivine (7870-I1). 7870-I1 has a concentric arrangement of olivine crystals and circular form, and clearly crystallized as a melt droplet. Etr-I1 contains one curving rim with concentrically aligned crystals and may be a droplet fragment.

Etr-I1 (Fig. 5e) is notable not only for having a large proportion of feldspar in mesostasis, but also a significant amount of coarse merrillite (6.2 area%) (Table A2) and thus a P-rich composition (1.69 wt% P_2O_5) (Table A3). Diopside occurs as rims on low-Ca pyroxene grains farther from the merrillite but is not present closer to the merrillite (Fig. 5e). This suggests that Ca was scavenged to make phosphate that locally inhibited the formation of diopside. Etr-I1 is much more feldspathic and phosphatic than the inclusion in Etter studied by Rubin et al. (1983a).

The single *FldP* object, Tdk-I1, is a fine-grained radial pyroxene droplet. As in radial pyroxene chondrules, low-Ca pyroxene in Tdk-I1 appears to have nucleated on the edge of the object and grown inward. This inclusion resembles some macrochondrules (Weyrauch and Bischoff, 2012).

The chemically unique Jgo-I1 inclusion has a distinctive texture. It contains olivine of different crystal habits, including barred olivine domains (parallel, elongate olivine) in some places, microporphyritic olivine domains elsewhere, and a single coarse (up to 4 mm diameter) equant olivine grain that is heavily fractured and veined but identified as a single grain based on crystallographic orientation and continuity of fracture patterns (Fig. 5f). The mesostasis of Jgo-I1 is feldspar-rich and merges with a feldspathic rim (Fig. 5f). Other minerals are intergrown with the feldspar in the inclusion, including chromite, metal, troilite, and phosphate. The feldspar-chromite association in Jgo-

I1 also occurs elsewhere in the host and resembles chromite-plagioclase assemblages in ordinary chondrites that have been interpreted as shock melts (Rubin, 2003).

Distinctive multimillimeter-to-submillimeter-sized grains of olivine and domains with barred-olivine-like texture are found in various inclusions of different chemical types, not just Jgo-I1. Coarse olivine is also present in Obl-I1 (~1 mm-diameter equant grains), *FldR* inclusion Etr-I1 (~2 mm-long tabular grains; Fig. 5e), and *Vfr(RE)* inclusion QUE-I4 (~3 mm-long tabular grains; extending off left side of Fig. 5c). Barred-olivine-like domains can have olivine arranged in circular shells ("donuts"—Jamsja and Ruzicka, 2010), or in parallel bars, or both (Fig. 1a). These features are reminiscent of barred olivine chondrules but occur wholly within inclusions. The best examples are in *FldR* inclusion 4859-I4 (object LITE4 of Jamsja and Ruzicka, 2010) and unique Jgo-I1, but they also occur in *Unfr* inclusions (Arm-I1—Fig. 1a, PVM-I1), *Unfr+K* inclusion Dim-I1, and *Vfr* inclusions (Khr-I1, McK-I1, Par-I1).

3.2.2 Phase compositions

Average endmember phase compositions (Fa, Wo/Wo/En, Ab/Or/An) for olivine, pyroxene, and feldspathic phases in inclusions overlap those found in equilibrated ordinary chondrites (EOCs, type 4-6 ordinary chondrites), especially for olivine and low-Ca pyroxene (Fig. 6). A variety of inclusion types (*Unfr*, *Unfr+K*, *Vfr*, *FldR*) contain normally zoned olivine grains with cores that are more magnesian (~$Fa_{5\text{-}15}$), and three *Vfr* inclusions contain more magnesian low-Ca pyroxene (MET-I1, clinoenstatite grain cores, $Wo_{0.6\pm0.6}$ $Fs_{11.5\pm1.4}$; Lut-I1, $Wo_{3.1\pm1.9}$ $Fs_{10.9\pm3.2}$; Rfd-I1, $Wo_{2.1\pm0.5}$ $Fs_{11.1\pm1.1}$), but *no inclusions were found that have low-FeO olivine (Fa<10) or low-FeO Ca-poor pyroxene (Fs<10) throughout*.

Among inclusions that contain olivine with magnesian cores, all but two, the *Unfr* inclusions 7873-I1 (Fig. 4c) and 4686-I1, occur in chondrites with type 3 lithologies. 7873-I1 has normally zoned olivine (cores $Fa_{10.9\pm2.0}$, rims $Fa_{19.9\pm1.8}$) despite being in an H5-6 host with equilibrated olivine (NWA

7873, $Fa_{18.5\pm0.4}$, Ruzicka et al., 2015). Similarly, 4686-I1 has normally zoned grains (cores $Fa_{11.7\pm1.9}$, rims $Fa_{18.0\pm1.7}$) despite being in an H4 host with equilibrated olivine (NWA 4686, $Fa_{17.7}$, Connolly et al., 2007).

Some inclusions of different chemical types have homogenous olivine more uniform and sometimes of different composition than the hosts in which they occur. These include *FldR* inclusion 7870-I1 ($Fa_{25.1\pm0.4,}$ mean and ±1σ) in an L4 host (NWA 7870, $Fa_{25.3\pm1.2}$, Ruzicka et al., 2015); *Unfr+K* inclusion 8231-I1 (Fig. 4f, $Fa_{21.0\pm0.2}$) in an H4-6 host (NWA 8231, $Fa_{19.4\pm0.4}$, Ruzicka et al., 2017); *Vfr* inclusions 7872-I1 ($Fa_{24.4\pm0.3}$) in an L3 host (NWA 7872, $Fa_{25.9\pm5.4}$, Ruzicka et al., 2015) and KrC-I1 ($Fa_{22.0\pm0.5}$) in an L4 host (Kramer Creek); and *Unfr* inclusions 8141-I1 ($Fa_{24.5\pm0.4}$) in an L3-6 host (NWA 8141, type 3 portion $Fa_{21.1\pm10.1}$, and granoblastic type 6 clast $Fa_{25.3\pm0.6}$, Ruzicka et al., 2015) and Par-I3 ($Fa_{29.5\pm0.3}$) in an LL3.6 host (Parnallee). The uniform Fa contents in these inclusions probably were not established by *in situ* equilibration with their hosts.

Most zoned olivine grains in inclusions have normal zoning patterns with magnesian cores and ferroan rims, but some *Unfr* and *Unfr+K* inclusions also contain reversely zoned grains. This includes *Unfr* inclusion Glk-I1 (Fig. 4b), and *Unfr+K* inclusions 869-I1 (Fig. 4c) and Dim-I1 (Fig. 4e). Fayalite contents in magnesian cores, and in ferroan cores and rims, differ somewhat between inclusions (Glk-I1: magnesian cores $Fa_{9.4\pm0.8}$, ferroan cores and rims $Fa_{18.1\pm2.2}$; 869-I1: magnesian cores $Fa_{11.4\pm0.9}$, ferroan cores and rims $Fa_{23.1\pm2.8}$; Dim-I1: magnesian cores $Fa_{5.3\pm1.4}$, ferroan cores and rims $Fa_{18.2\pm4.4}$). Some of the reversely zoned grains in all three of these inclusions are fragments, as evident from discontinuous zoning patterns (Fig. 4b, 4d, 4e). In 869-I1, some of the normally zoned grains also have discontinuous zoning. Grain fragmentation in Glk-I1 is also evident from interrupted sulfide vein or inclusion trails in olivine, a distinctive feature in this inclusion that occurs in both reversely and normally zoned grains (Fig. 4b).

Most inclusions have feldspar or glass with relatively low K content (Or < 9 mol%) (Fig. 6b). For these, Ab/An ratios vary widely, and systematically between inclusion chemical types. *Plagioclase tends to be sodic in Unfr and FldR inclusions (Ab_{78-84}), and calcic in Vfr inclusions (Ab_{13-65})* (Fig. 6b). The former are close to EOC values, whereas the latter are depleted in Na (Fig. 6b). However, some *Vfr* inclusions (7872-I1, QUE-I3, McK-I1) contain feldspathic glass that is much more sodic (Ab_{87-88}) than the plagioclase in these inclusions (Fig. 6b). The opposite pattern is shown by glasses in *Unfr* (7873-I1, 4686-I1, Glk-I1) and *FldR* (Rgl-I1) inclusions, which are less sodic (Ab_{35-70}) than plagioclase in other *Unfr* and *FldR* inclusions (Fig. 6b).

Feldspathic phases with higher K contents occur in some inclusions. These include glasses in *Unfr+K* inclusions (MET-I2, 869-I1, and Dim-I1) with Or ~15-34 mol%, and feldspar in *Unfr+K* inclusion 8231-I1 ($Ab_{82.7\pm1.6}$ $Or_{13.6\pm1.9}$) (Fig. 6b). Thus, *all Unfr+K inclusions have feldspathic phases with elevated Or contents*, consistent with their bulk enrichment in K. In addition, potassic glass with Or ~25 mol% occurs in *FldR* inclusion Etr-I1 (Fig. 6b).

In inclusions that contain plagioclase and glass of different composition, the compositions straddle that of feldspar in EOCs. For example, in *FldR* inclusion Etr-I1, Or contents in plagioclase ($Or_{1.1\pm0.1}$) are notably lower than in EOCs, and Or contents in glass are much higher, with a tie line between the two extending approximately through the EOC range (Fig. 6b). Similarly, the *Vfr* inclusions 7872-I1, McK-I1 and QUE-I3 all have plagioclase much more calcic than in EOCs, but glasses that are less calcic (Fig. 6b). This suggests for these inclusions *a possible redistribution of Na-Ca-K between plagioclase and a glass or melt phase,* from a chondritic feldspar composition. However, bulk *Vfr* inclusions are depleted in alkalis relative to Ca (Fig. 1), suggesting they had subchondritic alkali contents prior to any redistribution between plagioclase and glass or melt.

Impact melts have olivine, pyroxene, and feldspathic phase compositions broadly similar to those in some inclusions (Fig. 5). In the melt rocks, most olivine grains tend to be not strongly zoned.

They have overall compositions resembling olivine in L chondrites (NWA 6579: $Fa_{24.7\pm1.7}$) or H chondrites (NWA 6554: $Fa_{17.7\pm1.7}$). In NWA 6554, however, some olivine grains have strong normal zoning and some have reverse zoning. In the melt breccias, olivine grains are zoned strongly, with both normal and reverse patterns (NWA 5964: magnesian grain cores $Fa_{11.3\pm0.9}$, ferroan grain cores and rims $Fa_{25.9\pm3.3}$, NWA 6580: magnesian grain cores $Fa_{11.1\pm1.0}$, ferroan grain cores and rims $Fa_{23.3\pm4.7}$). The Fa ranges and patterns of olivine zoning in the melt breccias resemble strongly zoned olivine found in some inclusions, especially *Unfr* inclusion Glk-I1 and *Unfr+K* inclusions 869-I1 and Dim-I1 (Fig. 6a).

Pyroxene was analyzed in the two melt rocks. NWA 6579 contains cores of low-Ca pyroxene ($Wo_{2.6\pm0.9}$ $Fs_{19.1\pm0.9}$) zoned to rims of augite ($Wo_{31.1\pm2.6}$ $Fs_{14.7\pm1.2}$). NWA 6454 contains small grains of low-Ca pyroxene ($Wo_{2.7\pm1.5}$ $Fs_{16.2\pm1.8}$) and pigeonite ($Wo_{10.4\pm2.8}$ $Fs_{16.8\pm1.6}$) forming overgrowths on olivine. These compositions fall in the EOC range for low-Ca pyroxene or are generally similar to the compositions of augite and pigeonite found in some *Vfr* and *Unfr* inclusions (Fig. 6a).

Feldspathic glasses of two compositions occur in the analyzed impact melts. L melt rock NWA 6579 has glass of EOC-like feldspar composition ($Ab_{81.9\pm2.1}$ $Or_{6.9\pm1.3}$), similar to glasses in some *Unfr* and *FldR* inclusions and the *FldP* inclusion (Fig. 6b). The remaining impact melts have more potassic glasses (NWA 6454: $Ab_{21.4\pm5.0}$ $Or_{15.0\pm3.5}$; NWA 5964: $Ab_{24.0\pm0.3}$ $Or_{23.8\pm0.2}$; NWA 6580: $Ab_{25.6\pm0.2}$ $Or_{24.7\pm0.2}$), which are chemically similar to glass in the two *Unfr+K* inclusions 869-I1 and Dim-I1 (Fig. 6b). There is an especially close chemical match between glass in melt rock NWA 6454 and in Dim-I1 (Fig. 6b).

3.3 Oxygen isotopic compositions of inclusions and their hosts

Oxygen isotope compositions for various aliquots of inclusions and their hosts are given in Table 4. $\delta^{18}O$ and $\Delta^{17}O$ values are plotted for all inclusions in Fig. 7a, and for various inclusion-host pairs in Fig. 7b-d. For these plots, mass-dependent fractionation such as expected for igneous

processes involves left-right shifts parallel to the terrestrial fractionation (TF) line, and mass-independent fractionation involves any shift not parallel to this line.

Oxygen isotope compositions for inclusions are broadly similar to ordinary chondrites. The isotopic compositions of inclusions overlap EOC fields (Clayton et al., 1991) but extend well past them (Fig. 7a). They also overlap "large chondrules" separated from ordinary chondrites, which also broadly overlap but extend past EOC ranges (Clayton et al., 1991) (Fig. 7a).

Oxygen isotope compositions of inclusions are related to their chemical types, rather than host groups. *All analyzed Vfr inclusions lie outside the EOC fields at lower* $\Delta^{17}O$ *and/or higher* $\delta^{18}O$ *values* (Fig. 7a). In contrast, most *Unfr* and *Unfr+K* inclusions overlap the EOC fields (7871-I1, 4686-I1, 8645-I1, 4859-I18, 869-I1, 8231-I1), although three lie clearly outside these fields (Obl-I2, MET-I2, Dim-I1) (Fig. 7a).

$\Delta^{17}O$ values of inclusions and their hosts can be either similar or dissimilar to one another. Similar values are shown for some *Unfr* and *Unfr+K* inclusions and their hosts (Fig. 7b). Oxygen isotope compositions are nearly the same for 869-I1 and its host NWA 869, and for 8231-I1 and its host NWA 8231 (Fig. 7b). Dim-I1 and host Dimmitt have similar $\Delta^{17}O$ values but differ mainly in $\delta^{18}O$ (higher for inclusion), consistent with mass fractionation (Fig. 7b). For both 4859-I18 and host NWA 4859, and 4686-I1 and host NWA 4686, $\Delta^{17}O$ values are slightly, but noticeably, higher (by ~0.10-0.15‰) in the inclusions.

Other *Unfr* and *Unfr+K* inclusions show larger shifts in $\Delta^{17}O$ compared to their hosts (Fig. 7c). *Unfr+K* inclusion MET-I2 has an oxygen isotope composition that lies outside the EOC range, with $\Delta^{17}O$ ~0.8‰ lower than its host MET 00489 (Fig. 7c). Two aliquots of *Unfr* inclusion Obl-I2 lie outside the EOC range and on a possible mixing line, ~0.5-0.9‰ lower in $\Delta^{17}O$ than seven analyzed aliquots of its host Oberlin, which cluster tightly within the LL field (Fig. 7c). *Unfr* inclusion 7871-I1 has an oxygen isotope composition that partly overlaps the H4-6 field, ~0.25‰ lower in $\Delta^{17}O$ than two

analyzed aliquots of host NWA 7871, which falls within the LL4-6 field (Fig. 7c). For these three inclusions, $\Delta^{17}O$ values are lower in inclusions than in hosts. The opposite pattern is shown by 8645-I1, which lies at the extreme high-$\Delta^{17}O$ range for LL4-6, with $\Delta^{17}O$ ~0.3‰ higher than two analyzed samples of host NWA 8645, which falls within the L4-6 field (or extreme low-$\Delta^{17}O$ end of LL4-6) (Fig. 7c).

All *Vfr* inclusions have $\Delta^{17}O$ values much lower than their hosts (Fig. 7d). Depending on the particular aliquots, $\Delta^{17}O$ differences between inclusion and host range from ~0.5-1‰ for MET-I1, from ~0.2-0.4‰ for MET-I3, from ~0.4‰ for Lut-I1, from ~0.3-0.5‰ for Rfd-I1, and from ~0.2-0.4‰ for QUE-I1, QUE-I3, and QUE-I4.

Vfr inclusions are sometimes isotopically homogenous and sometimes heterogeneous. The three QUE inclusions have nearly identical oxygen isotope compositions, with five of six analyses in multiple aliquots forming a tight field (Fig. 7d), despite being potentially different inclusions from separate fragments of the QUE 97008 host meteorite. In contrast, MET-I1 aliquots range widely in isotopic compositions, with two analyses falling close to the TF line and showing apparent mass fractionation (in replicate analyses), and the other two aliquots having compositions more similar to the QUE cluster (Fig. 7d)

Among thirteen chondrites analyzed for oxygen isotopes, five (all L or LL chondrites) do not plot in the groups expected based on their classifications and the data of Clayton et al. (1991). Lut 005 (classified LL3.7/3.8; Hutson et al., 2014; Ruzicka et al., 2017) and found in the hot Lut desert of Iran (Pourkhorsandi et al., 2013, 2016), has $\delta^{18}O$ values ~2‰ higher than LL4-6 (Fig. 7d). Richfield (classified LL3.7 and found in Kansas; Rubin et al., 1996) is isotopically heterogeneous, but has $\Delta^{17}O$ more appropriate to the L4-6 oxygen field (Fig. 7d). QUE 97008 (classified L3.05 and found in Antarctica; Grossman, 1999) also appears to be heterogeneous, and falls within the H4-6 range (Fig. 7d). MET 96515 (classified L3.5 and found in Antarctica; Grossman, 1999) has low $\delta^{18}O$ values that

place it outside the typical ordinary chondrite range (Fig. 7d). NWA 7871 (L6) appears to be homogenous, but plots within the LL4-6 field when both $\delta^{18}O$ and $\Delta^{17}O$ are considered (Fig. 7c).

These discrepancies can be largely explained by terrestrial weathering effects. Terrestrial weathering can affect oxygen isotope compositions in part because oxidation and hydration of metal during weathering introduces oxygen from the terrestrial environment (Bland et al., 2000, 2006). Such weathering of ordinary chondrites in non-Antarctic environments typically causes shifts to higher $\delta^{18}O$ and lower $\Delta^{17}O$ (Clayton et al., 1991; Stelzner et al., 1999; Bland et al., 2000), whereas weathering in Antarctic environments causes shifts to lower $\delta^{18}O$ and lower $\Delta^{17}O$ (Bland et al., 2000; Greenwood et al., 2012). The oxygen data are consistent with hot desert weathering for Lut 005, cold desert weathering for MET 96515 and QUE 97008, and weathering in a more temperate climate for Richfield. For NWA 7871, LL was considered an alternate acceptable designation to L based on silicate compositions and metal contents (Ruzicka et al., 2015). An LL6 designation for NWA 7871 is preferred as it would be more consistent with the somewhat high $\delta^{18}O$ value, but this value could have been increased by hot desert weathering, making the classification of NWA 7871 uncertain. NWA 4686 (H4) could have experienced a modest weathering-related fractionation. Compared to the inclusion it contains, the host is much more weather-stained, and has slightly lower $\Delta^{17}O$ (by ~0.15‰) and somewhat higher $\delta^{18}O$ (by ~0.6‰) (Fig. 7b). This is consistent with hot-desert weathering preferentially affecting the host, but not so significantly that the host was shifted completely out of the H field (Fig. 7b).

In all of these meteorites, there is no evidence that oxygen isotopic compositions of inclusions were significantly affected by terrestrial weathering (Electronic Annex). This could be caused in part by the low porosities of inclusions (apart from cracking possibly produced by sample preparation), which should make them more impervious to weathering than the more porous and presumably more

permeable chondrite hosts. Furthermore, as metal contents in inclusions are low, there is less opportunity for addition of terrestrial oxygen during oxidation and hydration of metal.

4. DISCUSSION

Below we discuss the implications of bulk compositions for the role of igneous differentiation (Sec. 4.1), the implications of mineral-chemical and textural data for metamorphism (Sec. 4.2), the implications of oxygen isotope data for source materials and mixing processes (Sec. 4.3), the mechanisms for creating inclusions (Sec. 4.4), and the possible relationship between large inclusions and chondrules (Sec. 4.5).

4.1 Bulk compositions and the role of igneous differentiation

Bulk composition data rule out a major role for igneous differentiation among the large inclusions studied. The inclusions have igneous textures and broadly ordinary-chondrite-like bulk chemical and isotopic compositions (Sec. 3.1, 3.3), suggesting they formed by crystallization of melts similar to ordinary chondrites in composition.

As important as the chondritic *average* composition are the bulk chemical fractionations shown by different groups of inclusions (Fig. 1). Such fractionations suggest that inclusions cannot all be simply explained as complete melts of chondrite. Only the *Unfr* type (Sec. 3.1.2) matches a complete melt, whereas other types vary around chondritic composition in different ways (Fig. 1, 2). Processes such as equilibrium or fractional melting, or equilibrium or fractional crystallization, should create fractionations between compatible (Mg) and incompatible elements (Al, Ti, K, Na), and compositions that are related to peritectics, cotectics, or reaction boundaries. These are generally not observed, suggesting that the variations cannot be explained by igneous differentiation. The *FldR* chemical type (Sec. 3.1.5) comes closest to being similar to that expected for a partial melt of chondrite, in that it is low in Mg relative to incompatible elements (Fig. 1d). However, inclusions in this group are too rich in normative olivine and too low in Si to correspond to an equilibrium or fractional melt (i.e.,

compositions extend to the upper left of ordinary chondrite in Fig. 2, not towards peritectic R or the olivine-pyxroxene phase boundary where partial melts of chondrite would lie).

The inability of igneous differentiation processes to explain the bulk compositions of inclusions in this study contrasts sharply with what has been previously interpreted for some inclusions in ordinary chondrites. These inclusions mostly have been described in terms of igneous rock lithologies, including microgabbro (Kennedy et al., 1992), troctolite (Hutchison et al., 1988; Sack et al., 1994; Nakamura et al., 1994), harzburgite (Nakamura et al., 1994), silica-rich pyroxenite (Ruzicka et al., 1995, 2012a), andesite (Ruzicka et al., 2012a), and granitoid (Bischoff et al., 1993; Terada and Bischoff, 2009) or a finer-grained variant of this. Other clasts rich in cristobalite, tridymite, feldspar, or nepheline also have been interpreted as differentiates (Bridges et al., 1995a, b). *Although evidence suggests that such igneous differentiates do occur in chondrites, based on this work they are not predominant.*

4.2 Petrographic-chemical data and the role of metamorphism

Petrographic and mineral chemical data provide constraints on metamorphic processes affecting inclusions, including the timing of inclusion melting relative to thermal metamorphism. Fe-Mg homogeneity in olivine and low-Ca pyroxene (taking an operational definition of homogeneity to be <1 mol% Fa or Fs standard deviation of mean compositions; Table 1) could indicate metamorphic re-equilibration. Textural blurring of inclusion-host contacts (Table 1) can be taken as evidence for *in situ* metamorphism. In contrast, glassy mesostases, zoned grains, and pigeonite (Sec. 3.2) indicate minimal metamorphism. Based on such data, Table 5 shows inferences for metamorphism and the relative timing of melting and metamorphic events for inclusions. Inclusions are grouped into five different cases.

Case 1— *Three inclusions formed after thermal metamorphism of their hosts.* Inclusions 4686-I1 and 7873-I1 contain zoned olivine grains, glassy mesostases, and sharp contacts with hosts, which

have chemically uniform olivine appropriate to petrographic type 4 to 6 metamorphism (Case 1a). 869-I1 has similar characteristics but has one margin that texturally intergrades with host containing type 3-6 material, suggesting inclusion formation after mixing of metamorphic grades and localized melting of host by intrusion of hot inclusion melt (Case 1b).

Case 2— Two inclusions were chemically homogenized, but not *in situ*. 8231-I1 was melted and homogenized to olivine Fa contents different than that of the homogenous type 4-6 host, and probably was introduced into the host while largely cold, leading to sharp inclusion-host contacts (Case 2a). 8141-I1 was similarly melted and homogenized, but has a partly broken and partly blurred contact with the host, and occurs in type 3-6 host (Case 2b). This inclusion was metamorphosed prior to late brecciation and mixing to create the type 3-6 host and the partly broken margins of the inclusion.

Case 3—*Seventeen inclusions were melted before metamorphism.* Eight inclusions have slight inhomogeneity in olivine and pyroxene and some blurred contacts with equilibrated hosts (Case 3a), whereas nine have homogeneous olivine and pyroxene with some blurred contacts with equilibrated hosts (Case 3b) (Table 5). All of these inclusions were probably metamorphosed *in situ*, differing only in the extent of their re-equilibration (more for Case 3b).

Case 4—Four inclusions (7870-I1, 7872-I1, KrC-I1, Par-I3) have olivine and low-Ca pyroxene compositions more uniform than the type 3 or 4 hosts in which they occur, sharp contacts with their hosts, and textures compatible with rapid crystallization (7870-I1: skeletal olivine, L4 host; 7872-I1: barred olivine, L3.7 host; KrC-I1: cryptocrystalline, L4 host; Par-I3: cryptocrystalline, LL3.6 host) (Table 1). These four inclusions are inferred to have cooled rapidly during crystallization to result in relatively unzoned grains.

Case 5— Sixteen inclusions occur in type 3 hosts and show no evidence they experienced significant metamorphism (Table 5). They contain zoned phenocrysts with sharp inclusion-host

contacts, and sometimes contain pigeonite or subcalcic augite that could have crystallized under igneous conditions.

Of the seventeen inclusions melted prior to metamorphism (Cases 3a and 3b, Table 5), seven are *Unfr* types found in type 5 or 6 hosts (8645-I1, Arm-I1, Arm-I2, PVM-I1, 4859-I18, 7871-I1, 8232-I1, Obl-I2). For these inclusions, *open-system chemical exchange may have resulted in relatively unfractionated abundances of lithophiles.*

Other Case 3 inclusions are not *Unfr* type and could have largely preserved their bulk chemical formation signatures. This includes the *Vfr(mono)* inclusions Cyn-I1 (L4 host) and Tdk-I2 (H5 host), the *Vfr(AD)* inclusions McK-I1 and McK-I2 (L4 host), the *FldR* inclusions 4859-I4 (LL5 host) and Etr-I1 (L5 host), *FldP* inclusion Tdk-I1 (H5 host), and the unique Jgo-I1 inclusion. *The presence of non-Unfr types of inclusions among those that were melted prior to metamorphism suggests that bulk chemical signatures were not always converted into Unfr as a result of metamorphism.*

The overall mineralogy of inclusions, reflected in their normative compositions, might be relatively resistant to change by metamorphism. For instance, the *FldR* and *FldP* inclusions owe their chemical signatures to an over- or under-abundance of a feldspar component, and Jgo-I1 owes its bulk chemical signature to both excess feldspar and chromite. Given that these minerals grow larger during thermal metamorphism in chondrites (e.g., Huss et al., 2006), they are stable during metamorphism and would be resistant to metamorphic destruction.

However, the *Vfr(AD)* inclusions, which are depleted in alkalis but otherwise relatively unfractionated, might be expected to be more susceptible to metamorphic obliteration, as they would require only an influx of Na and K in glass or feldspar (presumably exchanging with Ca and Al) to become the *Unfr* type. Metamorphism might explain why no examples of such inclusions occur in type 5 or 6 chondrites, only two occur in type 4 (McK-I1, McK-I2, both from McKinney), and four occur in type 3. Aside from alkalis, the *Vfr(AD)* type strongly resembles *Unfr* inclusions in terms of

overall normative compositions and trend (Fig. 2). This implies that some *Unfr* inclusions may have been of *Vfr(AD)* type prior to open-system metamorphic exchange.

Other Unfr inclusions obtained their unfractionated abundances upon formation. These include inclusions 4686-I1 and 7873-I1, which were melted after metamorphism (Case 1, Table 5).

Among inclusions representing early melting events, most are in L and LL hosts (Table 5). For the H-group, only Tamdahkt (H5) was found to contain inclusions (Tdk-I1 and Tdk-I2) that formed prior to metamorphism. A similar analysis of melt rock clasts of presumed impact origin also found group differences between the timing of melting events relative to metamorphism, with more examples of pre-metamorphic melting in L and LL than in H chondrites (Rubin et al., 1983a). This was ascribed to differences in impact histories, with less exposure of early impact-melted material in the H chondrite body as a result of less large-scale impact reworking (Rubin et al., 1983a). This may be related to a higher proportion of solar-gas-bearing (regolithic) breccias in H chondrites than L and LL chondrites (Bischoff et al., 2018). In any case, *our results support the conclusion that L and LL chondrites incorporated a relatively large number of early-formed melts compared to H chondrites.*

4.3 Oxygen isotope implications for reservoirs, xenoliths, and mixing processes

Oxygen isotopic data for inclusions and their hosts sometimes show small differences in $\Delta^{17}O$, and sometimes show large differences (Sec. 3.3). Differences in $\Delta^{17}O$ (= host – inclusion) are plotted in Fig. 8, which emphasizes different patterns for various inclusion/host pairs. These data have implications for inclusion petrogenesis, which is discussed below and summarized in Table 6.

4.3.1 Small shifts in $\Delta^{17}O$

Inclusions and hosts with small shifts in $\Delta^{17}O$ include *Unfr+K* inclusions 869-I1, 8231-I1, and Dim-I1, and *Unfr* inclusions 4686-I1 and 4859-I18 (Fig. 7b, 8). The overall oxygen isotopic compositions are especially similar between inclusions 869-I1 and host NWA 869, and between 8231-I1 and host NWA 8231-I1 (Fig. 7b, 8). Slight weathering of host may account for the small difference

in $\Delta^{17}O$ between 4686-I1 and host (Sec. 3.3), and may also account for a similar change between 4859-I18 and host (Fig. 8). *Oxygen isotope data for the three Unfr+K and two Unfr inclusions suggest they formed by melting of their hosts* (Table 6).

4.3.2 Large shifts in $\Delta^{17}O$

Inclusions and hosts with large $\Delta^{17}O$ shifts include *Unfr* inclusions Obl-I2, 7871-I1 and 8645-I1, *Unfr+K* inclusion MET-I2, and *Vfr* inclusions MET-I1, MET-I3, QUE-I1, QUE-I3, QUE-I4, Lut-I1, and Rfd-I1 (Fig. 7c-d, 8). In each of these cases except for 8645-I1, $\Delta^{17}O$ is higher in host than inclusion (Fig. 8). All except 7871-I1 and 8645-I1 have distinctive oxygen isotope compositions that plot well outside of the EOC fields at lower $\Delta^{17}O$ and mostly higher $\delta^{18}O$ values (Fig. 7c-d). We infer that *most inclusions with oxygen isotopic compositions significantly different than their hosts formed in lower-$\Delta^{17}O$ reservoirs prior to becoming incorporated in ordinary chondrite parent bodies.*

A shift to higher $\Delta^{17}O$ from inclusion to host now appears to be part of a pattern that continues from earlier reports (Rubin et al., 1981; Prinz et al., 1984; Mayeda et al., 1987; Hutchison et al., 1988; Ruzicka et al., 1995; Bridges and Hutchison, 1997; Almeida et al., 2017), although there are counterexamples (Rubin et al., 1983a; Casanova et al., 1987; Herd et al., 2013), as in this study. For the former case of inclusions with lower $\Delta^{17}O$ than their hosts, previous work has shown: (1) two low-$\Delta^{17}O$ inclusions (~0.35-0.47‰, similar to MET-I2 and MET-I3 of this study) in the L6 chondrite Y-793241 (Mayeda et al., 1987); (2) three inclusions with H-like oxygen isotopic composition in the Bovedy (L3), Y-75097 (L6), and Barwell (L5) chondrites (Rubin et al., 1981; Mayeda et al., 1987; Hutchison et al., 1988; Bridges and Hutchison, 1997); and (3) inclusion Bo-1 with H-like $\Delta^{17}O$ (~0.7‰) but much higher $\delta^{18}O$ (Fig. 7a) in Bovedy (Ruzicka et al., 1995). *That so many of the inclusions melted in a lower-$\Delta^{17}O$ reservoir prior to incorporation into their host ordinary chondrites could reflect a temporal change in the environment in which they formed*. This should be tested by dating inclusions analyzed for oxygen isotopes.

A mostly one way change to increasing $\Delta^{17}O$ is consistent with a variety of data for chondrite components such as chondrules and refractory inclusions (Clayton, 1993; Bridges et al., 1998; Wasson et al., 2004; Krot et al., 2005, 2006; Ruzicka et al, 2007). This could indicate that large igneous inclusions formed in reservoirs undergoing the same sort of changes as reflected in these other chondrite components. Such apparently systematic changes among different chondritic components suggests a global, probably nebular, environment in which $\Delta^{17}O$ was increasing. However, this inference is tempered by observations of the reverse case of inclusions with higher $\Delta^{17}O$ than their hosts (see below, for 8645-I1), as well as with similar $\Delta^{17}O$ to their hosts (Sec. 4.3.1). Moreover, previous work found evidence that framework silicates and glass in clasts and chondrules have lower ^{16}O than in mafic minerals as a result of preferential gas-solid exchange, suggesting that isotopic exchange processes depended on mineralogy (Bridges et al., 1995a, 1998, 1999).

Regardless of a possible temporal change in oxygen reservoirs, *inclusions with large $\Delta^{17}O$ shifts provide evidence for nebular or collisional mixing or transport of primitive materials*. Transport sometimes occurred prior to thermal metamorphism of asteroid bodies. For example, *the three Unfr inclusions 7871-I1, 8645-I1, and Obl-I2 appear to be xenoliths that formed in a different oxygen isotope reservoir than in which they were later metamorphosed.* All of these inclusions were melted prior to *in situ* metamorphism in parent bodies, during which time mafic minerals in the inclusions were largely to completely homogenized in Fe-Mg (Sec. 4.2, Table 5). However, the oxygen isotopic compositions of the inclusions were less re-equilibrated, preserving evidence that the inclusions formed in different environments and were subsequently transported. 7871-I1 was melted in an H-like oxygen reservoir (Fig. 7c), and was then transported to an LL (or L) source region where it was metamorphosed (Fig. 8, Table 6). 8645-I1 was melted in an LL-like oxygen reservoir (Fig. 7c), and was then transported to an L source region (Fig. 8, Table 6). Obl-I2 was melted in a distinctive low-$\Delta^{17}O$ environment similar to that which produced *Vfr* inclusions (Fig.7c), and was then transported

into an LL source region (Fig. 8, Table 6). This inclusion shows evidence for partial re-equilibration of oxygen isotopic compositions with the host (Fig. 7c).

Aside from the metamorphosed xenoliths, large $\Delta^{17}O$ shifts occur in type 3 chondrites for seven *Vfr* inclusions (MET-I1, MET-I3, Lut-I1, Rfd-I1, and the QUE trio) and a single *Unfr+K* inclusion (MET-I2) (Fig. 8). Each avoided significant metamorphism (Table 5), and each was transported from the distinctive low-$\Delta^{17}O$ environment in which they formed to L or LL parent bodies (Fig. 8, Table 6). *The Vfr (and MET-I2) inclusions can be regarded as weakly metamorphosed xenoliths, significantly different in isotopic composition than the typical composition of their host groups.*

4.4 Origins of inclusions

Oxygen isotopic and chemical-petrographic data together suggest multiple origins for inclusions. These are outlined below according to inclusion chemical type. Fig. 9 compares the bulk compositions of inclusions to other materials in terms of key element ratios and serves as a framework for this section and the next.

4.4.1 Unfr+K inclusions

High K contents in *Unfr+K* inclusions result in them having distinctively high values of (Na/Mg + K/Mg) at roughly chondritic Al/Mg (Fig. 9). They include four inclusions studied here (869-I1, 8231-I1, Dim-I1, MET-I2) and probably the centimeter-sized lithic clasts in the Krähenberg (LL5) and Bhola (LL3-6) chondrites studied by Wloztka et al. (1983). Rubin (1985) and Bridges and Hutchison (1997) also identified melt rocks and clasts with elevated K contents.

We conclude that *Unfr+K inclusions formed by impact melting of chondritic protoliths*, supporting previous assertions regarding K-rich fragments (Wlotzka et al., 1983; Rubin, 1985; Bridges and Hutchison, 1997). The evidence mostly relies on similarities between *Unfr+K* inclusions and known impact melts.

(1) The bulk chemical composition of the inclusions, including their distinctive enrichment in K, resembles those found in some impact melts (Fig. 1b, 9). The latter include melt rocks and melt rock breccias of ordinary chondrites studied here (Sec. 3.1.3, 3.1.7, Table 2), as well as the melt breccia Chico (Bogard et al., 1995; Norman and Mittlefehldt, 2002), and terrestrial impactites (Yakovlev and Parfenova, 1980; Grieve, 1978).

(2) The textures and mineralogies of the inclusions, including microporphyritic and poikilitic textures, olivine phenocryst sizes, often glassy mesostases, occasional presence of metal-sulfide nodules, and sometime presence of unmelted interior chondritic patches or clasts, are similar to those in impact melts (Sec. 3.2.1).

(3) The composition of glass (in 869-I1, Dim-I1) is distinctive (Na-poor, K-rich) and similar to those in impact melts (Sec. 3.2.2).

(4) The zoning patterns and overall Fa contents in olivine (in 869-I1, Dim-I1, MET-I2), including both normal and reverse patterns, are similar to those in impact melts (Sec. 3.2.2). We suggest that the ferroan cores of some grains are relict ferroan grains incorporated from the host that were not destroyed by melting. The magnesian cores of other grains are either relict magnesian grains or early-crystallizing grains from the melts.

(5) Evidence for broken olivine crystals set in glass (in 869-I1, Dim-I1) (Sec. 3.2.2) is suggestive of mechanical deformation before solidification was complete. Sharp discontinuities in zoning patterns of broken grains imply minimal post-brecciation diffusion, suggesting rapid crystallization.

(6) There is evidence in one inclusion (869-I1) for *in situ* melting of host, adjacent to a shock blackened area (Sec. 3.2.1).

(7) Oxygen isotopic compositions of three of four inclusions overlap ordinary chondrites in general, and the hosts in particular, consistent with the melting of host chondrites (H chondrite

protolith for Dim-I1 and 8231-I1, L chondrite protolith for 869-I1; Sec. 4.4.1). For MET-I2, the oxygen isotope composition implies a protolith reminiscent of that inferred for the IIE silicate-bearing irons Netschaëvo, Techado, and Garhi Yasin (Bild and Wasson, 1977; Rubin, 1990; McDermott et al., 2016). However, high precision analyses indicate that the postulated "HH" body of these irons has $\Delta^{17}O \sim 0.58\text{-}0.59‰$ (McDermott et al., 2016), much higher than for MET-I2 ($\Delta^{17}O \sim 0.34‰$). Thus, MET-I2 was not derived from the "HH" body, but rather a different one.

The reason for the K enrichment in *Unfr+K* inclusions and some impact melts is unclear. Two possibilities for K fractionation in impact products have been discussed: (1) Na-K metasomatic exchange between impact-heated rock and vapor (Wlotzka et al., 1983), and (2) Na-K fractionation during formation of maskelynite, a shock-produced feldspar glass (Chen and El Goresy, 2000).

Wlotzka et al. (1983) noted that although K contents in two lithic fragments they studied were high compared to hosts, Na contents were lower, a pattern similar to that observed here. This was attributed to Na-K exchange between crystalline feldspar and vapor (Wlotzka et al., 1983), such as has been observed in experiments (Orville, 1962). But it is not obvious how this would explain K enrichment in glassy areas devoid of crystalline feldspar. It might require diffusion between hot inclusion melt or glass and surrounding feldspar-bearing chondrite host, for which there is little evidence.

Maskelynite is typically enriched in K compared to unmelted feldspar (Chen and El Goresy, 2000). This might be caused by fractionation of Na and K at high shock pressures, with Na partitioning into the high pressure polytype majorite, and K partitioning into vapor and then into melt that ultimately quenched as maskelynite (Chen and El Goresy, 2000). However, no maskelynite or high-pressure phases were observed in *Unfr+K* inclusions, and the mostly unfractionated composition of *Unfr+K* inclusions suggests nearly complete melting of chondrite, not the melting of feldspathic material alone envisioned for maskelynite.

Thus, neither of the proposed mechanisms for impact-induced K fractionation completely accounts for *Unfr+K* inclusions. Instead, *exchange of K between melt and vapor that results in K enrichment in melt, and not necessarily requiring the presence of crystalline feldspar or the formation of maskelynite, would be consistent with the observations.*

4.5.2 Unfr inclusions

Inclusions of the *Unfr* type resemble bulk chondrite in lithophile element abundances. This is true both for inclusions whose bulk compositions were possibly affected by open system exchange during thermal metamorphism (Case 3, Table 5) as well as for other inclusions that may have formed with unfractionated compositions (Sec. 4.2) (Fig. 9). Some impact melts have similar compositions (Fig. 9).

We suggest a dual origin for Unfr inclusions: (1) impact melting of chondritic hosts without K enrichment; and (2) metamorphism of earlier-formed melts. Some inclusions can be placed in one group or the other; others fit into both groups.

An impact melt origin is indicated for at least five *Unfr* inclusions.

(1) 4686-I1 was formed by melting of an H-chondrite target similar to the host (Sec. 4.4) after metamorphism (Sec. 4.2), which strongly suggests impact melting.

(2) 7873-I1 was melted after H chondrite metamorphism (Sec. 4.2), probably by *in situ* melting that also expelled immiscible metal and sulfide liquid to form a large adjacent nodule (Fig. 4c).

(3) A similar process is inferred for creating PVM-I1 and its adjacent nodule (Fig. 4c of Hutson et al., 2013), although here melting occurred prior to or during metamorphism in the L chondrite parent body (Sec. 4.2). *In situ* shock melting for PVM-I1 and 7873-I1 is supported by evidence for strong shock in the two host meteorites (Hutson et al., 2013; Ruzicka et al., 2017).

(4) Impact melting of LL-like host is consistent with oxygen isotope data for 4859-I18 and its host (Table 6) and consistent with the conclusions of Jamsja and Ruzicka (2010) for inclusions in NWA 4859.

(5) An impact melt origin is strongly suggested for Glk-I1 (Fig. 4b) on the basis of olivine phenocryst grain sizes, presence of metal-sulfide nodule, and olivine zoning patterns (which all resemble impact melts—Sec. 3.2.1, 3.2.2), evidence for breaking of crystals prior to melt solidification (Sec. 3.2.2), and other evidence for internal deformation, including areas of mafic glass that separate clasts (Fig. 4b). The latter could be produced by a separate episode of deformation and melting, or in the later stages of the same event that created the original inclusion.

Most *Unfr* inclusions experienced metamorphism. The large proportion of this type of inclusion in type 5 and 6 hosts (Fig. 3), as well as the high proportion of *Unfr* inclusions with equilibrated EOC-like compositions of phases (Fig. 6) and blurred inclusion-host contacts (Table 5), suggest that many of the *Unfr* inclusions in high-type chondrites were strongly affected by metamorphism. More specifically, a metamorphic origin partly obscuring an earlier history is suggested for Obl-I2, 7871-I1, and 8645-I1. These inclusions have oxygen-isotopic compositions suggesting they are xenoliths (Sec. 4.4), but mineral compositions and blurred inclusion-host contacts suggesting *in situ* metamorphism (Sec. 4.2). The latter could have resulted in open-system exchange that changed bulk compositions to create an *Unfr* inclusion. This is particularly true of Obl-I2, a megadroplet that resembles other *Vfr* inclusions in form as well as in oxygen isotopic composition. 7871-I1 also may have originated as a *Vfr* megadroplet, based on a texture (and granular olivine rim) similar to *Vfr* megadroplets Lut-I1 and 7872-I1.

4.4.3 FldR and Jgo-I1 inclusions

The four *FldR* inclusions (4859-I4, 7870-I1, Etr-I1, Rgl-I1) and unique Jgo-I1 inclusion are rich in a Na-feldspar component, resulting in superchondritic Al/Mg and (Na/Mg + K/Mg) values (Fig. 9).

We suggest that the FldR and Jgo-I1 inclusions formed by non-equilibrium shock melting and concentration of a feldspar component. Their compositions resemble melt pockets (Fig. 2, 9), which were produced by *in situ* shock melting (Dodd and Jarosewich, 1982; Rubin, 1985; Stöffler et al., 1991), as well as the compositions of partial melts in disequilibrium experiments (Feldstein et al., 2001; Lunning et al., 2017), although some of the melt pockets and experimental melts are more silica-rich. None of the inclusions have the compositions one would expect of equilibrium partial melting. Thus, disequilibrium melting is implied.

Mechanisms for creating *FldR* inclusions and Jgo-I1 appear to have varied somewhat. Inclusions 4859-I4, 7870-I1, and Etr-I1 lie on approximate mixing line between ordinary chondrite and plagioclase, suggesting their compositions can be explained simply by selective melting and concentration of feldspar. Inclusions Rgl-I1 and Jgo-I1 have elevated normative plagioclase as well as being poor in silica (low normative quartz), plotting closer in Fig. 2 to the olivine-plagioclase join. For these inclusions, and for reasons uncertain, enrichment in feldspar must be accompanied by removal of silica or low-Ca pyroxene.

7870-I1 is drop-formed and could have crystallized as a free-floating droplet. It may thus be an example of a large impact melt spherule.

In contrast, the unique texture and composition of Jgo-I1 (Fig. 5f) is interpreted as being partly aggregational in nature. The different domains of barred olivine, coarse olivine, and microporphyritic olivine connected by plagioclase + Cr-spinel bands could have formed by the aggregation of different-textured units by shock-produced feldspathic melt. These textural units would have included coarse-grained protolith and possibly partly melted chondrules. The mesostasis of Jgo-I1 is similar to

chromite-plagioclase assemblages common in many EOCs and attributed to shock melting (Rubin, 2003), but the exact mechanism in creating such assemblages is not known. A partly aggregational origin for Jgo-I1 is consistent with high siderophile element contents (Fig. 1h) and placement of metal between textural domains (Fig. 5f), which can be explained by the entrapment of metallic liquid between more solidified domains.

4.4.4 Vfr inclusions

Vfr inclusions have superchondritic Al/Mg and subchondritic (Na/Mg + K/Mg) (Fig. 9). They clearly formed at elevated temperature by vapor fractionation processes (Sec. 3.1.4). Many, perhaps all, originated as droplets, although most *Vfr* inclusions do not show actual drop form and would have to be brecciated (Sec. 3.2.1).

The compositions of most *Vfr* inclusions approach those expected for equilibrium condensates or residues or chondritic systems (Fig. 9). In detail, most inclusions have compositions that appear to lie on mixing lines between an ordinary chondrite (e.g., L chondrite) composition and different condensate/residue compositions (Fig. 9). These condensate/residue compositions can be created at different temperatures, highest for *Vfr(RE)* inclusions, lowest for *Vfr(AD)* inclusions, and mostly intermediate for *Vfr(mono)* inclusions (Fig. 9).

The mixing lines can be interpreted in different ways. They could represent (1) physical mixtures of refractory and chondritic material, (2) refractory material produced by evaporation that back-reacted with chondritic composition following evaporation, or (3) disequilibrium residue compositions of chondrites produced by rapid heating. We infer that *most Vfr inclusions formed primarily as evaporative melts and mixtures.*

For *Vfr(RE)* inclusions such as QUE-I4 (Fig. 5c), we suggest a physical mixture of refractory material with a chondritic component. This would explain the superchondritic abundances of the most refractory elements (Al, Ti, Ca) and near-chondritic abundances of other lithophile elements, including

alkali elements (Fig. 1f). It is also consistent with the textures of the QUE trio of inclusions, which have both coarser and finer-grained components as well as evidence for internal brecciation that could have physically mixed different components (Fig. 5c). The refractory material in the QUE inclusions resides in mesostasis glass, feldspar, and Ca-pyroxene overgrowths, whereas the non-refractory material consists of coarse-grained olivine and low-Ca pyroxene. Therefore, coarse ferromagnesian precursors may have been mixed with refractory melt. This refractory melt could have originated as an evaporative residue; alternatively, it could have originated by melting of a discreet refractory component of unknown identity. Oxygen isotope data imply that all of the QUE inclusions formed from the same batch of material (Fig. 7d), which must have been large to be found in multiple pieces of the same meteorite. In contrast, fine-grained droplet KrC-I1 is also of the *Vfr(RE)* type, and shows no evidence in its current form of being a physical mixture or derivation from a larger batch of material. It could have formed as a complete melt of a refractory-ferromagnesian mixture.

For *Vfr(AD)* inclusions such as MET-I3 (Fig. 5d), an evaporative melt origin involving comparatively modest heating followed by more-or-less back reaction with a chondritic reservoir is preferred. This would explain depletions in the most volatile alkali elements and a nearly unfractionated composition for other lithophile elements. Less intense heating could have resulted in less efficient removal of metal and sulfide as immiscible melts, explaining somewhat higher abundances of siderophile elements in these inclusions compared to other *Vfr* types (Fig. 1).

Vfr(mono) inclusions such as Rfd-I1 (Fig. 5b) and Par-I1 (Fig. 5a, right) could have formed as evaporative melts that partly back-reacted with their chondritic surroundings. At least the former and possibly the latter inclusion are megadroplets that show mineralogical-textural evidence for back reaction, in the form of pyroxene-rich rims. Reaction between melts and silica-bearing vapor to form low-Ca pyroxene at the melt-gas interface has been experimentally demonstrated (Tissandier et al., 2002). Given the similar condensation temperatures for Mg and Si (Lodders, 2003), silica vapor would

be generated during heating of chondritic material to make refractory residues with elevated Al/Mg, as in *Vfr* inclusions (Fig. 14). Pyroxene rims are also present on the *Vfr(AD)* inclusions 7869-I1 and McK-I2 (Table 1), and these inclusions also could have experienced back-reaction with silica-rich gas, despite their apparent lesser heating. Thus, back-reaction between refractory melt and Si-rich gas can explain both the overall compositions as well as pyroxene rimming textures of various *Vfr(mono)* and *Vfr(AD)* inclusions.

Megadroplet Rfd-I1 has additional complex mineralogical zoning suggestive of reaction with its surroundings. It has an olivine-pyroxene-glass core surrounded by an olivine-glass mantle and finally a low-Ca pyroxene-glass rim (Fig. 5b). Olivine and pyroxene in the core and most of the mantle have intermediate Fe contents, olivine in the outermost mantle is comparatively Fe-rich, and pyroxene in the rim is Fe-poor. These large fluctuations in mineralogy and phase compositions suggest disequilibrium within the inclusion and its surroundings.

The only *Vfr* inclusion that cannot be explained as an evaporative melt or mixture is drop-formed inclusion Par-I2 (Fig. 5a, left), which has subchondritic Al/Mg (Fig. 9). It is most enriched in elements with intermediate volatility (Si, Cr, Mn) (Fig. 1e) and is rich in normative orthopyroxene (Fig. 2). This composition and the droplet form could be created by fractional condensation, with removal of a refractory condensate followed by incomplete condensation of more volatile elements in a melt droplet.

Vfr inclusions have distinctive oxygen isotopic compositions (Secs. 3.3, 4.4.2). In principle, these can be explained either by exchange with a gas of distinctive composition or melting of material unlike ordinary chondrite. As explained below, we suggest that *melting of materials somewhat similar to but not quite identical to ordinary chondrite, together with mass fractionation, best explains both the chemical compositions and distinctive oxygen isotope compositions of Vfr inclusions.*

Although chemical compositions of *Vfr* inclusions can be explained as involving an ordinary-chondrite-like system that was variably heated, this system may not have been actual ordinary chondrites but rather a related chondrite type with similar chemical but different isotopic composition. It could have been similar to the low-$\Delta^{17}O$ protolith inferred for *Unfr+K* inclusion MET-I2 (Sec. 4.5.1). The oxygen isotope composition of *Vfr* inclusion MET-I3 is similar to MET-I2 (Fig. 7a), so melting of the same precursor can explain both inclusions.

Compared to MET-I2 and MET-I3, other *Vfr* inclusions have higher $\delta^{18}O$ values (by ~1-3‰) (Fig. 7d). Significant mass fractionation to heavier isotopes therefore would be required to make these other inclusions from starting material similar to that which could have melted to produce MET-I2 and MET-I3.

The high $\delta^{18}O$ values in most Vfr inclusions could have arisen by kinetic isotope mass fractionation. During rapid evaporation at low pressures, residues obtain isotopically heavier oxygen as a result of kinetic isotope fractionation (Davis et al., 1990; Young et al., 1998). Experiments and modeling show that increases of up to ~3‰ in $\delta^{18}O$, the approximate magnitude needed for some *Vfr* inclusions, can be produced by ~15% mass loss under certain conditions (Davis et al., 1990; Young et al., 1998). Larger amounts of mass loss and increases in $\delta^{18}O$ would be possible, if some back reaction between the residues and surroundings occurred. Taken to completion, such back-reaction for oxygen isotopes even could have driven the composition of MET-I3 back to its starting value.

It is also possible but less likely that the high $\delta^{18}O$ values of most *Vfr* inclusions reflect gas-condensate equilibrium. Gas with nebular H_2O/CO in equilibrium with olivine will have $\delta^{18}O$ about ~2‰ higher than the olivine (Clayton et al., 1991). This implies that to make inclusions as equilibrium condensates, the gas would have to be higher in $\delta^{18}O$ than the measured inclusion compositions, i.e., even further from an ordinary chondrite composition. Although this cannot be excluded, there is no independent evidence for the requisite gas composition, which would have to be high in $\delta^{18}O$ but

quasi-ordinary-chondrite-like in $\Delta^{17}O$, and which does not conform to the usual observation for variations in ^{16}O component observed for meteoritic materials. The alternate explanation that inclusions formed as evaporative residues involving kinetic isotopic fractionation is favored as it fits with the chemical data for inclusions and is more compatible with a quasi-ordinary-chondrite reservoir.

Regardless, $\Delta^{17}O$ is the key parameter for evaluating the reservoirs of these inclusions. Fig. 8 implies that MET-I2, MET-I3, and the average composition of MET-I1 could all have originated from similar low-$\Delta^{17}O$ (~0.30-0.36‰) reservoirs. However, this does not explain the isotopic heterogeneity of MET-I1, which seems to require at least two different reservoirs (Sec. 4.3). Lut-I1, Rfd-I1, and the QUE trio could have formed from materials transitional to H chondrites ($\Delta^{17}O$ ~ 0.44-0.55‰, Fig. 8). Finally, Obl-I2, although not now a *Vfr* inclusion, probably formed as one, by the melting of materials similar to that for Lut-I1, Rfd-I1 and the QUE trio (Fig. 8), with some increase in $\Delta^{17}O$ caused by later metamorphic exchange (Sec. 4.4.2).

4.4.5 Assessment and comparison to previous work

The data suggest two major origins of inclusions.

(1) *Planetary impact melts formed as impact melts of chondritic planetesimals*, and include the *Unfr+K* and *FldR* chemical types as well as some *Unfr* inclusions and the unique Jgo-I1. Textures are commonly microporphyritic but also include poikilitic, cryptocrystalline, skeletal, spinifex, and porphyritic-barred olivine hybrids.

(2) *Nebular melts are comprised of vapor-fractionated melts or melt-solid mixtures*, and include all of the *Vfr* chemical subtypes. Many or all of these originated as droplets, or suspended melts, that could have experienced considerable evaporative mass loss and variable back-reaction in a nebula of chondritic composition. Textures include microporphyritic, cryptocrystalline, skeletal, poikilitic, granular, and microporphyritic-barred olivine variants. Textures (and mineralogies) are

grossly similar to planetary impact melts, highlighting a difficulty in using petrographic data alone to discriminate origins. They could have formed as impact melt droplets that were chemically and isotopically processed while free-floating, or by any heating mechanism that could have operated on chondritic matter and that ultimately became free-floating in the nebula.

These two major groups correspond roughly to the Na-rich and Na-poor inclusions (clasts and megachondrules) of Ruzicka et al. (1998, 2000), respectively. Impact melts and macrochondrules also were recognized as two major types of inclusions by Bridges and Hutchison (1997). We suggest that some inclusions studied by others could be planetary differentiates (Bridges and Hutchison, 1997; Ruzicka et al., 2012a), but that these are less prevalent than impact melts and nebular melts as none were found in this study.

Our results place constraints on the model of forming inclusions by the disruption of planetesimal magmaspheres (Crowther et al., 2018). This suggested origin is problematic for the following reasons. (1) The composition of average inclusion implies roughly 100% melting with 80% loss of metal and sulfide, but in a liquid magmasphere all dense metal and sulfide should sink to form a core. To prevent this, one could invoke vigorous convection to suspend some of the dense liquid. Alternatively, some liquid core material could be added back to liquid silicate mantle if the molten planetesimals were collisionally disrupted and mixed. More plausible is the incomplete separation of liquid metal from the smaller cooling melt units represented by inclusions. (2) A substantially molten, possibly vigorously convecting magmasphere might be expected to be chemically uniform, but individual inclusion compositions vary considerably around an average bulk ordinary chondrite composition (Fig. 1, 2, 9). These compositional variations are largely unexplained by the magmasphere hypothesis. There could have been multiple magmaspheres, each with a different composition, but igneous processes alone cannot create these compositions. (3) A partially molten magmasphere might be expected to lead to equilibrium partial melts or crystallization products of such

melts. However, these processes do not appear to have operated for most inclusions. (4) Feldspathic (*FldR*) inclusions are best explained by partial melting of chondrite with preferential melting of a feldspar component during disequilibrium shock melting. This implies solid precursors inconsistent with the magmasphere hypothesis. (5) The close correspondence in oxygen isotope compositions between some *Unfr+K* and *Unfr* inclusions and their hosts would have to be pure coincidence if the inclusions formed from magmaspheres. They are more plausibly explained by shock melting of the hosts.

4.5 Implications for chondrule origins

Large inclusions have similarities and differences to chondrules in ordinary chondrites (Table 7).

Similar normative compositions suggest that both types of objects are broadly ordinary-chondrite-like in overall compositions. Textures are generally similar too, with a prevalence of microporphyries (Lauretta et al., 2006), although drop-formed inclusions have a higher proportion of skeletal textures than chondrules (Weyrauch and Bischoff, 2012). This implies broadly similar crystallization and thermal histories. Mineralogies are generally similar, including the presence of clinoenstatite in weakly-heated meteorites, which again suggests similar compositions and cooling histories during crystallization (Jones, 1996a). Both types of objects can have pyroxene rims, implying that both can experience melt-gas interaction (Friend et al., 2016; however, pyroxene rims do not necessarily require melt-gas reaction; Rubin, 2018). Oxygen isotopic compositions of "large chondrules" (Clayton et al., 1991; Bridges et al. 1998) overlap those of inclusions, although the latter have more prominent examples of low-$\Delta^{17}O$ and high-$\delta^{18}O$ objects. This could indicate possibly similar reservoirs for chondrules and inclusions, but many of the "large chondrules" are probably inclusions as defined here, given that the chondrules of Bridges et al. (1998) are ~0.5-7 mm across, and those of Clayton et al. (1991) are ~0.8-8.6 mm across (based on reported masses and assumed

spherical objects with a density of 3 g/cm^3). Finally, similar groupings can be made for both sets of objects based on bulk Na/Al (Ruzicka et al., 1998, 2000). This could indicate two broadly different origins for chondrules (planetary and nebular melts).

The most obvious difference between the objects is the large sizes of inclusions compared to chondrules. The masses of the former are ~10^2 – 10^6 times greater for 3.5-40 mm-diameter inclusions than the 0.4-0.7 mm-diameter chondrules typical of ordinary chondrites (assuming spherical objects with densities of 3 g/cm^3). Clearly the amount of melt production was *much* greater for inclusions. Another significant difference is a dearth of magnesian olivine (Fa < 10) compositions in inclusions, unlike Type I chondrules. Also, there is little metal in inclusions compared to some Type I chondrules. This appears to indicate an absence of Type I-like inclusions. It could indicate that inclusions formed at higher fO_2 than Type I chondrules. Another significant difference is the absence of relict dusty-metal-bearing olivine and relict forsterite grains in inclusions, although some *Unfr+K* and *Unfr* inclusions appear to have different types of relict grains. The relict grains in chondrules provide evidence for the recycling of chondrules (Jones, 1996b), specifically of Type II into Type I chondrules and of Type I into Type II chondrules (Ruzicka et al., 2007; Ruzicka, 2012), but there is no evidence for such a cyclical process affecting inclusions. Some *Unfr+K* inclusions contain chondritic clasts, which are absent in chondrules, suggesting incomplete melting of precursor solids. This could indicate that chondrules were more thoroughly melted (at odds with the presence of relict grains), or were less likely to trap unmelted material owing to smaller chondrule melt volumes. Finally, some inclusions contain multimillimeter olivine grains that are absent in chondrules, or millimeter-to-submillimeter-sized domains of olivine "donuts" and barred textures that are not common as subunits of chondrules. These coarse grains and domains may represent nucleation sites in melts with few other nuclei, based on analogy with experimental studies of barred olivine chondrule textures (Lofgren, 1989; Connolly and Hewins, 1995; Tsuchiyama et al., 2004), possibly the remnants of largely melted chondrules that

served as nucleation sites. Alternatively, coarse grains could be remnants of coarse-grained (plutonic?) precursors.

Given the similarities and differences, one can reasonably infer that *chondrules could have formed in ways similar to inclusions, but that there were also important differences*. Fig. 9 demonstrates this similar-but-not-the-same aspect based on the chemistries of inclusions and representative chondrule types. Type IA and IB chondrules are alkali-depleted like *Vfr* inclusions, but are more magnesian and not as aluminous (Fig. 9). Type IIB chondrules have elevated alkali and aluminum contents like *FldR* inclusions, but are more silica-rich, and overall do not resemble the normative compositions of these inclusions or melt pockets, despite similar CI-normalized (Al/Mg) and (Na/Mg + K/Mg) ratios (Fig. 9). Type IIA chondrules have quasi-chondritic compositions (Fig. 9). They chemically resemble *Unfr* inclusions, except for being somewhat richer in Na_2O (1.65 ± 0.35 wt%, Jones, 1990) than *Unfr* inclusions (1.02 ± 0.32 wt%, Table 2).

5. CONCLUSIONS

(1) The bulk chemical compositions of the inclusions studied here vary broadly around chondritic composition, comprise four main bulk chemical types and some other variants, and show no evidence of having formed as igneous differentiates. In general, they formed by variations of melting processes affecting ordinary chondrite-like material.

(2) The oxygen isotope compositions of inclusions overlap ordinary chondrite compositions and are related to inclusion chemical type.

(3) Inclusions of the generally unfractionated but K-enriched (*Unfr+K)* type formed as impact melts of chondritic planetesimals, including ordinary chondrite parent bodies and a low-$\Delta^{17}O$ body.

(4) Inclusions of the unfractionated (*Unfr)* chemical type formed as impact melts of chondritic planetesimals or by open-system metamorphism in such planetesimals. Some *Unfr* inclusions formed

on one type of chondritic body, but were transported to another body in which they were metamorphosed.

(5) Inclusions of the feldspar-rich (*FldR*) type formed by the preferential melting and concentration of feldspar during disequilibrium shock melting of chondritic protoliths, in a process analogous to that which produced melt pockets but on a much larger scale.

(6) Inclusions of the vapor-fractionated (*Vfr)* chemical type are best explained as nebular melts that formed largely by evaporative melting and as melt-solid mixtures. Potential heating mechanisms could be impact melting and dispersal in the nebula, or any mechanism that melted chondritic material and allowed chemical and isotopic modification of free-floating melt droplets. These inclusions have low $\Delta^{17}O$ and high $\delta^{18}O$ values and formed in reservoirs with $\Delta^{17}O$ lower than their hosts.

(7) Different inclusions formed both before and after metamorphism of their hosts. L and LL chondrites contain a relatively large number of early-formed melts.

(8) Overall, the results of this study point to important and varied roles for both "planetary" impact melting and "nebular" evaporative melting processes to form different large igneous inclusions in ordinary chondrites. Chondrules may have formed by processes similar to those inferred for large inclusions, but with some important differences. Chief among these are that only chondrules have Type I-like characteristics, and only chondrules show evidence for Type I-II recycling processes. The genetic relationship of inclusions and chondrules deserves further study.

Acknowledgments

We thank Denton Ebel, Kevin Righter, Cecilia Satterwhite and the Meteorite Working Group (MWG) for making samples available for study, three anonymous reviewers and Dr. Melinda Hutson for reviews of this manuscript, and Dr. James Day for editorial handling. NASA funding (NASA grant NNH12ZDA001N to Principal Investigator AR) is gratefully acknowledged. Research on inclusions

by the lead author was stimulated by post-doctoral work performed with Prof. Larry A. Taylor, and this paper is dedicated to his memory.

REFERENCES

Almeida N.V., Downes H., Smith C.L., Greenwood R.C., Hellmann J.L., Kleine T., Franchi I.A. and Russell S.S. (2017) Igneous Inclusions in the Barwell L6 Chondrite. In *80th Annual Meeting of the Meteoritical Society*, abstract #6116.

Anders E. and Grevesse N. (1989) Abundances of the elements: Meteoritic and solar. *Geochim. Cosmochim. Acta*, **53**(1), 197-214.

Armstrong K. (2014) *Chemical and Petrographic Survey of Large, Igneous-Textured Inclusions in Ordinary Chondrites*, M.S. thesis, Portland State University. 161 p.

Bild R.W. and Wasson J.T. (1977) Netschaevo: A new class of chondritic meteorite. *Science* **197**(4298), 58-62.

Binns R.A. (1967) An exceptionally large chondrule in the Parnallee meteorite. *Mineral. Mag.* **36**(279), 319-324.

Bischoff A., Geiger T., Palme H., Spettel B., Schultz L., Scherer P., Schlüter J. and Lkhamsuren J. (1993) Mineralogy, chemistry, and noble gas contents of Adzhi-Bogdo–an LL3–6 chondritic breccia with L-chondritic and granitoidal clasts. *Meteoritics* **28**(4), 570-578.

Bischoff A., Schleiting M., Wieler R. and Patzek M. (2018) Brecciation among 2280 ordinary chondrites–Constraints on the evolution of their parent bodies. *Geochim. Cosmochim. Acta* 238, 516-541.

Bland P.A., Lee M.R., Sexton A.S., Franchi I.A., Fallick A.E.T., Miller M.F., Cadogan J.M., Berry F.J. and Pillinger C.T. (2000) Aqueous alteration without a pronounced oxygen-isotopic shift: Implications for the asteroidal processing of chondritic materials. *Meteorit. Planet. Sci.* **35**(6), 1387-1395.

Bogard D.D., Garrison D.H., Norman M., Scott E.R.D. and Keil K. (1995) ^{39}Ar-^{40}Ar age and petrology of Chico: Large-scale impact melting on the L chondrite parent body. *Geochim. Cosmochim. Acta* **59**(7), 1383-1399.Brearley A.J. and Jones R.H. (1998) Chondritic meteorites. In *Planetary Materials* (ed. J.J. Papike), Reviews in Mineralogy 36, pp. 3/1-3/398. Mineralogical Society of America: Washington.

Bridges J.C. and Hutchison R. (1997) A survey of clasts and large chondrules in ordinary chondrites. *Meteorit. Planet. Sci.* **32**(3), 389-394.

Bridges J.C., Franchi I.A., Hutchison R., Morse A.D., Long J.V.P. and Pillinger C.T. (1995a) Cristobalite- and tridymite-bearing clasts in Parnallee (LL3) and Farmington (L5). *Meteoritics* **30**(6), 715-727.

Bridges J.C., Hutchison R., Franchi I.A., Alexander C.M. and Pillinger C.T. (1995b) A feldspar-nepheline achondrite clast in Parnallee. *Antarctic Meteorite Research* **8**, 195-203.

Bridges J.C., Franchi I. A., Hutchison R., Sexton A.S. and Pillinger C.T. (1998) Correlated mineralogy, chemical compositions, oxygen isotopic compositions and the sizes of chondrules. *Earth Planet. Sci. Lett.* **155**,183–196.

Bridges J., Franchi I., Sexton A. and Pillinger C. (1999) Mineralogical controls on the oxygen isotopic compositions of UOCs. *Geochim. Cosmochim. Acta* **63**(6), 945-951.

Casanova I., Miller M.L., Keil K., Wieler R., King E.A. and Sanmiguel A. (1987) Brecciation and impact-melt rock formation of ordinary chondrites - Evidence from a study of Spanish meteorites. *Meteoritics* **22**, 351.

Chen M. and El Goresy A. (2000) The nature of maskelynite in shocked meteorites: not diaplectic glass but a glass quenched from shock-induced dense melt at high pressures. *Earth Planet. Sci. Lett.* **179**(3-4), 489-502.

Clayton R.N. (1993) Oxygen isotopes in meteorites. *Ann. Rev. Earth Planet. Sci.* **21**,115–149.

Clayton R.N., Mayeda T.K., Goswami J.N. and Olsen E.J. (1991) Oxygen isotope studies of ordinary chondrites. *Geochim. Cosmochim. Acta* **55**, 2317–2337.

Connolly H.C., Jr. and Hewins R.H. (1995) Chondrules as products of dust collisions with totally molten droplets within a dust-rich nebular environment: An experimental investigation. *Geochim. Cosmochim. Acta* **59**(15), 3231-3246.

Connolly H.C., Jr., Smith C., Benedix G., Folco L., Righter K., Zipfel J., Yamaguchi A., Chennaoui Aoudjehane H. (2007) The Meteoritical Bulletin, No. 92, 2007 September. *Meteorit. Planet. Sci.* **42**(9), 1647-1694.

Crowther S.A., Filtness M.J., Jones R.H. and Gilmour J.D. (2018) Old formation ages of igneous clasts on the L chondrite parent body reflect an early generation of planetesimals or chondrule formation. *Earth Planet. Sci. Lett.* **481**, 372-386.

Davis A.M., Hashimoto A., Clayton R.N. and Mayeda T.K. (1990) Isotope mass fractionation during evaporation of Mg_2SiO_4. *Nature* **347**(6294), 655-657.

Dodd R.T. and Jarosewich E. (1982) The compositions of incipient shock melts in L6 chondrites. *Earth Planet. Sci. Lett.* **59**(2), 355-363.

Dodd R.T., Jarosewich E., and Hill B. (1982) Petrogenesis of complex veins in the Chantonnay (L6f) chondrite. *Earth Planet. Sci. Lett.* **59**, 364–374.

Feldstein S.N., Jones R.H. and Papike J.J. (2001) Disequilibrium partial melting experiments on the Leedey L6 chondrite: Textural controls on melting processes. *Meteorit. Planet. Sci.* **36**(11), 1421-1441.

Fodor R.V. and Keil K. (1975) Implications of poikilitic textures in LL-group chondrites. *Meteoritics* **10**(4), 325-339.

Fodor R.V., Keil K., Prinz M., Ma M.S., Murali A.V. and Schmitt R.A. (1980) Clast-laden melt-rock fragment in the Adams County, Colorado, H5 chondrite. *Meteoritics* **15**(1), 41-62.

Friend P., Hezel D.C. and Mucerschi D. (2016) The conditions of chondrule formation, Part II: Open system. *Geochim. Cosmochim. Acta* **173**, 198-209.

Garvie L.A.J. (2012) The Meteoritical Bulletin, No. 99, April 2012. https://www.lpi.usra.edu/meteor/docs/mb99.pdf

Greenwood R., Franchi I., Gibson J. and Benedix G. (2012) Oxygen isotope variation in primitive achondrites: The influence of primordial, asteroidal and terrestrial processes. *Geochim. Cosmochim. Acta* **94**, 146-163.

Greenwood R.C., Barrat J.A., Scott E.R., Haack H., Buchanan P.C., Franchi I.A., Yamaguchi A., Johnson D., Bevan A.W. and Burbine T.H. (2015) Geochemistry and oxygen isotope composition of main-group pallasites and olivine-rich clasts in mesosiderites: Implications for the "Great Dunite Shortage" and HED-mesosiderite connection. *Geochim. Cosmochim. Acta* **169**, 115-136.

Grieve R.A. (1978) The melt rocks at Brent crater, Ontario, Canada. In *Lunar and Planetary Science Conference Proceedings* (Vol. 9, pp. 2579-2608).

Grossman J.N. (1999) The Meteoritical Bulletin, No. 83, 1999 July. *Meteorit. Planet. Sci.* **34**, A169-A186.

Grossman J.N., Rubin A.E., Nagahara H. and King E.A. (1988) Properties of chondrules. In *Meteorites and the Early Solar System* (eds. J.F. Kerridge and M.S. Matthews), pp.619-659. University of Arizona Press: Tucson.

Herd C., Friedrich J., Greenwood R., Franchi I. and Sylvester P. (2013). An igneous-textured clast in the Peace River meteorite: Insights into accretion and metamorphism of asteroids in the early solar system. *Canadian Journal of Earth Sciences Revue* **50**(1), 14-25.

Huss G.R., Rubin A.E. and Grossman J.N. (2006) Thermal metamorphism in chondrites. *Meteorites and the Early Solar System II* (eds. D.S. Lauretta and H.Y. McSween, Jr.), pp.567-586. University of Arizona Press: Tucson.

Hutchison R. (2004) *Meteorites: A petrologic, chemical and isotopic synthesis*. Cambridge University Press. 506 p.

Hutchison R., Williams C.T., Din V.K., Clayton R.N., Kirschbaum C., Paul R.L. and Lipschutz M.E. (1988) A planetary, H-group pebble in the Barwell, L6, unshocked chondritic meteorite. *Earth Planet. Sci. Lett.* **90**(2), 105-118.

Hutson M.L. and Ruzicka A.M. (2010) Jungo 001, Jungo 002, Jungo 003, and Big Horn Mountains: Four new chondrites from Nevada and Arizona which contain a variety of unusual petrographic features. *Lunar Planet Sci. XXXXI*, abstract #1878.

Hutson M., Ruzicka A., Jull A.J.T., Smaller J.E. and Brown R. (2013) Stones from Mohave County, Arizona: Multiple falls in the "Franconia strewn field". *Meteorit. Planet. Sci.* **48**(3), 365-389.

Hutson M.L., Ruzicka A.M. and Nazari M. (2014) Diverse and unusual O-chondrites from the Lut desert, Iran. In *77th Annual Meeting of the Meteoritical Society*, abstract #5180.

Jamsja N. and Ruzicka A. (2010) Shock and thermal history of NWA 4859, an annealed impact-melt breccia of LL-chondrite parentage containing unusual igneous features and pentlandite. *Meteorit. Planet. Sci.* **45**, 828-849.

Jarosewich E. (1990) Chemical analyses of meteorites: A compilation of stony and iron meteorite analyses. *Meteoritics* **25**, 323-337.

Jones R.H. (1990) Petrology and mineralogy of type II, FeO-rich chondrules in Semarkona (LL3. 0): Origin by closed-system fractional crystallization, with evidence for supercooling. *Geochim. Cosmochim. Acta* **54**(6), 1785-1802.

Jones R.H. (1994) Petrology of FeO-poor, porphyritic pyroxene chondrules in the Semarkona chondrite. *Geochim. Cosmochim. Acta* **58**(23), 5325-5340.

Jones R.H. (1996a) FeO-rich, porphyritic pyroxene chondrules in unequilibrated ordinary chondrites. *Geochim. Cosmochim. Acta* **60**(16), 3115-3138.

Jones R.H. (1996b) Relict Grains in Chondrules: Evidence for Chondrule Recycling. In *Chondrules and the Protoplanetary Disk* (eds. R. Jones and E. Scott), pp.163-172. Cambridge: Cambridge University Press.

Jones R.H. and Scott E.R.D. (1989) Petrology and thermal history of type IA chondrules in the Semarkona (LL3. 0) chondrite. In *Lunar and Planetary Science Conference Proceedings* (Vol. 19, pp. 523-536).

Keil K., Fodor R.V., Starzyk P.M., Schmitt R.A., Bogard D.D. and Husain L. (1980) A 3.6-by-old impact-melt rock fragment in the Plainview chondrite: Implications for the age of the H-group chondrite parent body regolith formation. *Earth Planet. Sci. Lett.* **51**(2), 235-247.

Kennedy A.K., Hutchison R., Hutcheon I.D. and Agrell S.O. (1992) A unique high Mn/Fe microgabbro in the Parnallee (LL3) ordinary chondrite: nebular mixture or planetary differentiate from a previously unrecognized planetary body? *Earth Planet. Sci. Lett.* **113**(1-2), 191-205.

Klein C. and Dutrow B. (2007) *Manual of Mineral Science*. Wiley. 23 p.

Krot A.N., Hutcheon I. D., Scott E.R.D., Libourel G., Chaussidon M., Aléon J., and Petaev M. I. (2005) Evolution of oxygen isotopic composition in the inner solar nebula. *Astrophys. J.* **622**, 1333–1342.

Krot A.N., Yurimoto H., McKeegan K.D., Leshin L., Chuassidon M., Libourel G., Yoshitake M., Huss G. R., Guan Y., and Zanda B. (2006) Oxygen isotopic compositions of chondrules: Implications for understanding oxygen isotopic evolution of the solar nebula. *Chemie der Erde* **66**, 249–276.

Lauretta D.S., Nagahara H. and Alexander C.M.D. (2006) Petrology and origin of ferromagnesian silicate chondrules. In *Meteorites and the Early Solar System II* (eds. D.S. Lauretta and H.Y. McSween, Jr.), pp.431-459. University of Arizona Press: Tucson.

Lodders K. (2003) Solar system abundances and condensation temperatures of the elements. *Astrophys. J.* **591**(2), 1220-1247.

Lofgren G. (1989) Dynamic crystallization of chondrule melts of porphyritic olivine composition: Textures experimental and natural. *Geochim. Cosmochim. Acta* **53**(2), 461-470.

Longhi J. (1991) Comparative liquidus equilibria of hypersthene-normative basalts at low pressure. *Am. Mineral.* **76**, 785–800.

Lunning N.G., Gardner-Vandy K.G., Sosa E.S., McCoy T.J., Bullock E.S. and Corrigan C.M. (2017) Partial melting of oxidized planetesimals: An experimental study to test the formation of oligoclase-rich achondrites Graves Nunataks 06128 and 06129. *Geochim. Cosmochim. Acta* **214**, 73-85.

Martins Z., Hofmann B.A., Gnos E., Greenwood R.C., Verchovsky A., Franchi I.A., Jull A.T., Botta O., Glavin D.P., Dworkin J.P. and Ehrenfreund P. (2007) Amino acid composition, petrology, geochemistry, 14C terrestrial age and oxygen isotopes of the Shişr 033 CR chondrite. *Meteorit. Planet. Sci.* **42**(9), 1581-1595.

Mayeda T.K., Clayton R.N. and Yanai K. (1987) Oxygen isotopic compositions of several Antarctic meteorites. *Mem. Natl. Inst. Polar Res.*, Spec. Issue **46**, 144-150.

McDermott K.H., Greenwood R.C., Scott E.R., Franchi I.A. and Anand M. (2016) Oxygen isotope and petrological study of silicate inclusions in IIE iron meteorites and their relationship with H chondrites. *Geochim. Cosmochim. Acta* **173**, 97-113.

Metzler K., Bischoff A., Greenwood R.C., Palme H., Gellissen M., Hopp J., Franchi I.A. and Trieloff M. (2011) The L3–6 chondritic regolith breccia Northwest Africa (NWA) 869:(I) Petrology, chemistry, oxygen isotopes, and Ar-Ar age determinations. *Meteorit. Planet. Sci.* **46**(5), 652-680.

Miller M.F., Franchi I.A., Sexton A.S. and Pillinger C.T. (1999) High precision $\delta^{17}O$ isotope measurements of oxygen from silicates and other oxides: method and applications. *Rapid Comm. Mass Spectrom.* **13**(13), 1211-1217.

Nakamura N., Morikawa N., Hutchison R., Clayton R.N., Mayeda T.K., Nagao K., Misawa K., Okano O., Yamamoto K., Yanai K. and Matsumoto Y. (1994) Trade element and isotopic characteristics of inclusions in the Yamato ordinary chondrites Y-75097, Y-793241 and Y-794046. *Antarctic Meteorite Research* **7**, 125-143.

Norman M.D. and Mittlefehldt D.W. (2002) Impact processing of chondritic planetesimals: Siderophile and volatile element fractionation in the Chico L chondrite. *Meteorit. Planet. Sci.* **37**(3), 329-344.

Orville P.M. (1962) Alkali metasomatism and feldspars. *Norsk Geologisk Tidsskrift* **42**, 283-316.

Petaev M.I. and Wood J.A. (1998) The condensation with partial isolation (CWPI) model of condensation in the solar nebula. *Meteorit. Planet. Sci.* **33**(5), 1123-1137.

Petaev M.I. and Wood J.A. (2005) Meteoritic constraints on temperatures, pressures, cooling rates, chemical compositions and modes of condensation in the solar nebula. In *Chondrites and the Protoplanetary Disk* (eds. A.N. Krot, E.R.D. Scott and B. Reipurth), pp. 373-406. ASP Conference Series, Vol. 341.

Pourkhorsandi H. and Mirnejad H. (2013) Lut Desert (Iran): A high-potential area for finding meteorites. In *44th Lunar Planet. Sci. Conf.*, abstract #1096.

Pourkhorsandi H., Rochette P., Gattaccecca J., D'Orazio M. and Mirnejad M. (2016) Lut Desert (IRAN) Meteorites: Distribution, Classification and Weathering. In *79th Annual Meeting of the Meteoritical Society*, abstract #1921.

Pouchou J.L. and Pichoir F. (1991) Quantitative analysis of homogeneous or stratified microvolumes applying the model "PAP". In *Electron Probe Quantitation* (eds. K.F.J. Heinrich and D.E. Newbury), pp. 31-75. New York: Plenum Press.

Prinz M., Nehru C.E., Weisberg M.K., Delaney J.S., Yanai K. and Kojima H. (1984) H chondritic clasts in a Yamato L6 chondrite: Implications for metamorphism. *Meteoritics* **19**, 292-293.

Prinz M., Weisberg M.K. and Nehru C.E. (1988) Gunlock, a new Type 3 ordinary chondrite with a golfball-sized chondrule. *Meteoritics* **23**, 297.

Rubin A.E. (1985) Impact melt products of chondritic material. *Rev. Geophysics* **23**(3), 277-300.

Rubin A.E. (1990) Kamacite and olivine in ordinary chondrites: Intergroup and intragroup relationships. *Geochim. Cosmochim. Acta* **54**(5), 1217-1232.

Rubin A.E. (2003) Chromite-plagioclase assemblages as a new shock indicator; implications for the shock and thermal histories of ordinary chondrites. *Geochim. Cosmochim. Acta* **67**(14), 2695-2709.

Rubin A.E. (2018) Evaluation of petrologic evidence for high partial pressures of SiO (g) in the solar nebula. *Meteorit. Planet. Sci.* **53**(12), 2596-2607.

Rubin A.E., Keil K., Taylor G.J., Ma M.S., Schmitt R.A. and Bogard D.D. (1981) Derivation of a heterogeneous lithic fragment in the Bovedy L-group chondrite from impact-melted porphyritic chondrules. *Geochimica Cosmochim. Acta* **45**(11), 2213-2228.

Rubin A.E., Rehfeldt A., Peterson E., Keil K. and Jarosewich E. (1983a) Fragmental breccias and the collisional evolution of ordinary chondrite parent bodies. *Meteoritics* ***18***(3), 179-196.

Rubin A.E., Scott E.R., Taylor G.J., Keil K., Allen J.S., Mayeda T.K., Clayton R.N. and Bogard D.D. (1983b) Nature of the H chondrite parent body regolith: Evidence from the Dimmitt breccia. *J. Geophys. Res. Solid Earth* **88** (S02), A741-A754.

Rubin A.E., Benoit P., Reed B., Eugster O. and Polnau W. (1996) The Richfield LL3 chondrite. *Meteorit. Planet. Sci.* **31**(6), 925-927.

Ruzicka A. (2012) Chondrule formation by repeated evaporative melting and condensation in collisional debris clouds around planetesimals. *Meteorit. Planet. Sci.* **47**(12), 2218-2236.

Ruzicka A., Kring D.A., Hill D.H., Boynton W.V., Clayton R.N. and Mayeda T.K. (1995) Silica-rich orthopyroxenite in the Bovedy chondrite. *Meteoritics* **30**(1), 57-70.

Ruzicka A., Snyder G.A. and Taylor L.A. (1998) Mega-chondrules and large, igneous-textured clasts in Julesberg (L3) and other ordinary chondrites: Vapor-fractionation, shock-melting, and chondrule formation. *Geochim. Cosmochim. Acta* **62**, 1419-1442.

Ruzicka A., Fowler G.W., Snyder G.A., Prinz M., Papike J.J. and Taylor L.A. (1999) Petrogenesis of silicate inclusions in the Weekeroo Station IIE iron meteorite: Differentiation, remelting, and dynamic mixing. *Geochim. Cosmochim. Acta* **63**, 2123-2143.

Ruzicka A., Snyder G.A. and Taylor L.A. (2000) Geochemical and isotopic evidence bearing on the origin of large, igneous-textured inclusions in ordinary chondrites. *Antarct. Meteorite Res.* **13**, 19-38.

Ruzicka A., Hiyagon H., Hutson M. and Floss C. (2007) Relict olivine, chondrule recycling, and the evolution of nebular oxygen reservoirs. *Earth Planet. Sci. Lett.* **257**, 274–289

Ruzicka A., Hutson M., Floss C. and Hildebrand A. (2012a) Large silica-rich igneous-textured inclusions in the Buzzard Coulee chondrite: Condensates, differentiates, or impact melts? *Meteorit. Planet. Sci.* **47**, 1809-1829.

Ruzicka A., Floss C. and Hutson M. (2012b) Agglomeratic olivine (AO) objects in ordinary chondrites: Accretion and melting of dust to form ferroan chondrules. *Geochim. Cosmochim. Acta* **76**, 103-124.

Ruzicka A., Grossman J., Bouvier A., Herd C.D.K. and Agee C.B. (2015) The Meteoritical Bulletin, No. 102, Aug. 19 2015. https://www.lpi.usra.edu/meteor/docs/mb102.pdf

Ruzicka A.M., Schepker K.L., Greenwood R.C. and Franchi I.A. (2016) Combined chemical-oxygen isotope study of large igneous inclusions in ordinary chondrites. *47th Lunar Planet. Sci. Conf.*, Abstract #2230.

Ruzicka A., Grossman J., Bouvier A. and Agee C.B. (2017) The Meteoritical Bulletin, No. 103. https://www.lpi.usra.edu/meteor/docs/mb103.pdf

Sack R.O., Ghiorso M.S., Wang M.S. and Lipschutz M.E. (1994) Igneous inclusions from ordinary chondrites: High temperature cumulates and a shock melt. *J. Geophys. Res. Planets* **99**(E12), 26029-26044.

Stelzner T.H., Heide K., Bischoff A., Weber D., Scherer P., Schultz L., Happel M., Schrön W., Neupert U., Michel R. and Clayton R.N. (1999) An interdisciplinary study of weathering effects in ordinary chondrites from the Acfer region, Algeria. *Meteorit. Planet. Sci.* **34**(5), 787-794.

Stöffler D., Keil K. and Scott E.R.D. (1991) Shock metamorphism of ordinary chondrites. *Geochim. Cosmochim. Acta* **55**(12), 3845-3867.

Terada K. and Bischoff A. (2009) Asteroidal granite-like magmatism 4.53 Gyr ago. *Astrophys. J. Lett.* **699**(2), L68-L71.

Tissandier L., Libourel G. and Robert F. (2002) Gas-melt interactions and their bearing on chondrule formation. *Meteorit. Planet. Sci.* **37**(10), 1377-1389.

Tsuchiyama A., Osada Y., Nakano T. and Uesugi K. (2004) Experimental reproduction of classic barred olivine chondrules: open-system behavior of chondrule formation 1. *Geochim. Cosmochim. Acta* **68**(3), 653-672.

Wasson J.T., Rubin A.E. and Yurimoto H. (2004) Evidence in CO3.0 chondrules for a drift in the O isotopic composition in the inner solar nebula. *Meteorit. Planet. Sci.* **39**, 1591–1598.

Weyrauch M. and Bischoff A. (2012) Macrochondrules in chondrites—Formation by melting of mega-sized dust aggregates and/or by rapid collisions at high temperatures? *Meteorit. Planet. Sci.* **47**(12), 2237-2250.

Wlotzka F., Palme H., Spettel B., Wänke H., Fredriksson K. and Noonan A.F. (1983) Alkali differentiation in LL-chondrites. *Geochim. Cosmochim. Acta* **47**(4), 743-757.

Yakovlev O.I. and Parfenova O.V. (1980) The role of vaporization and condensation in the formation of the chemical composition of impactites. In *Lunar and Planetary Science Conference* **11**, 1285-1287.

Yanai K., Matsumoto Y. and Kojima H. (1983) A Brachina-like inclusion in the Yamato-75097 L6 chondrite: A preliminary examination. *Mem. Nat. Inst. Polar Res.*, Special Issue **30**, 29-35.

Young E.D., Nagahara H., Mysen B.O. and Audet D.M. (1998) Non-Rayleigh oxygen isotope fractionation by mineral evaporation: Theory and experiments in the system SiO_2. *Geochim. Cosmochim. Acta* **62**(18), 3109-3116.

FIGURE CAPTIONS

Fig. 1. Mean bulk CI-normalized abundances (bars = ±1σ errors, n = number of objects averaged) for inclusion chemical types and some individual inclusions (data from Table 2). Elements are grouped according to T_{c50} values (Ruzicka et al., 2012b, after Lodders, 2003), lithophiles on left and partly to wholly siderophile/chalcophile on right. Average ordinary (O) chondrite (Hutchison, 2004) shown for comparison. (a) *Unfr* (unfractionated) inclusions. (b) *Unfr+K* (generally unfractionated, except strongly K-enriched) inclusions, and mean chondritic impact melt (Table 3). (c) *Vfr* (vapor-fractionated) inclusions, all varieties. (d) *FldR* (feldspar-rich) inclusions. (e) *Vfr(mono)* (vapor-fractionated, monotonic abundance variation) inclusions and individual inclusion Par-I2, a *Vfr(int)* inclusion. (f) *Vfr(RE)* (vapor-fractionated, refractory- element-enriched) inclusions. (g) *Vfr(AD)* (vapor-fractionated, alkali-depleted) inclusions. (h) Data for individual inclusions Tdk-I1 (*FldP* = feldspar-poor) and Jgo-I1 (unique). Average CI chondrite composition taken from Anders and Grevesse (1989). Large errors for elements such as Ti, K, and P for some inclusion types reflect in part the difficulty in accurate determinations of minor element abundances with the reconstruction technique used.

Fig. 2. Normative bulk compositions of inclusions in an olivine (Ol) – quartz (Qz) – plagioclase (Pl) ternary liquidus diagram (Ruzicka et al., 1999, after Longhi 1991); magnified portion near Ol vertex shown below. OC designates the field for bulk ordinary chondrites (Jarosewich, 1990); the dashed line shows the field for melt pockets in ordinary chondrites (Dodd and Jarosewich, 1982; Dodd et al. 1982). Bz-1, Bz-2, and Bz-3 are inclusions in Buzzard Coulee (Ruzicka et al., 2012a). Abbreviations: R = peritiectic; E = eutectic; Opx = orthopyroxene; lpx = low-Ca pyroxene; aug = augite; SiO_2 = silica mineral; px = pyroxene; Wo = wollastonite; Or = orthoclase; NAB = normative albite; NOR = normative orthoclase; Mg# = Mg/(Mg+Fe). Inclusion types as in Fig. 1.

Fig. 3. Distribution of inclusion chemical types according to petrographic type of the host chondrite, by **(a)** number of inclusions and **(b)** percentage of inclusions. For genomict breccias, the lowest type is used. Inclusion chemical types as in Fig. 1. Droplets are shown by stippled patterns in (a). Type 3 and 4 chondrites contain similar proportions of four different chemical types (*Vfr*, *Unfr+K*, *Unfr*, *FldR*) and are dominated by the *Vfr* chemical type, whereas in type 5 and 6 chondrites, the *Unfr* chemical type is more dominant.

Fig. 4. Images of *Unfr* (a-c) and *Unfr+K* (d-f) inclusions. **(a)** False color BSE+EDS image of Arm-I1, showing olivine phenocrysts (green) set in a diopside-rich (red) groundmass. Other phases include plagioclase (purple), phosphate (orange), and low-Ca pyroxene (tan). Arrows point to barred olivine domains, including one "donut" (D) with a half-complete olivine shell and interior bars. **(b)** False color BSE+EDS image of Glk-I1, showing complex brecciation and veining effects. Olivine grains (green) occur as magnesian phenocrysts (P) with narrow ferroan rims, and reversely zoned (R), often broken grains with ferroan cores (light green) and magnesian overgrowths. These grains are set in a feldspathic mesostasis (F, purple) which in turn are present as clasts within a more mafic matrix (M, tan). Troilite (pale yellow-green) is present as veins and inclusions; arrows point to olivine grains that contain troilite veins that do not extend past the edge of the crystals into adjacent groundmass. **(c)** BSE montage of 7873-I1 and an adjacent nodule composed of two troilite lumps surrounded by metal. Olivine grains in the inclusion are increasingly concentrated towards the right, changing into a spinifex texture. **(d)** BSE image of 869-I1, which contains both normally zoned olivine phenocrysts (dark grey interiors, lighter rims) and reversely zoned (R), sometimes broken olivine grains (arrow) set in a glassy, K-rich mesostasis. The inclusion has a sharp contact with the host at top left, but grades into it

at right where it incorporates two clasts (A—pyroxene rich clast, largely intact, and B—partly melted clast with ferroan (light grey) olivine bars, pyroxene overgrowths, and mesostasis that merges into mesostasis of inclusion). **(e)** False color BSE+EDS map of Dim-I1 showing olivine set in a glassy, feldspathic, K-rich mesostasis (purple). The clast has a broken margin (top). Olivine occurs as phenocrysts (P), some with unusually magnesian cores (arrows), as well as reversely zoned grains (R), some broken (e.g., grains left center). Veinlets are filled with weathering products. **(f)** Cross-polarized transmitted light image of 8231-I1, showing orthopyroxene (opx) oikocrysts, which poikilitically enclose olivine (ol) chadocrysts, surrounded by finer-grained interstitial areas rich in olivine, plagioclase, augite, troilite, and phosphate. Oikocryst clusters appear somewhat clastic.

Fig. 5. Images of *Vfr* (a-d), FldR (e), and chemically unique (f) inclusions. Abbreviations and phase colors same as in Fig. 4 and as given below. **(a)** False color BSE+EDS image of Par-I1 (right) and Par-I2 (left), two *Vfr(mono)* inclusions. Par-I1 contains ol phenocrysts set in a groundmass of zoned pigeonite (pig, tan-pink) and plagioclase (plag, purple); low-Ca pyroxene (lpx, tan-brown) occurs only on the inclusion edge. Par-I2 contains lpx, mainly reversely zoned (R), and ol, set in a glass-rich (gl) mesostasis; pig (pink) forms overgrowths on lpx. **(b)** False color BSE+EDS image of Rfd-I1, an intact *Vfr(mono)* droplet with a zoned interior containing chiefly lpx (enriched in core) and ol (enriched in mantle), and a rim rich in magnesian lpx. **(c)** False color BSE+EDS image of QUE-I4, a *Vfr(RE)* inclusion showing complex brecciation effects, including two major breccia contacts (dashed lines) that correspond to abrupt changes in texture. Microfaults separate coarse (multi-millimeter) ol dominating at left; finer-grained ol together with lpx and glassy mesostasis (meso) at center; and finer-grained lpx and meso nearly devoid of ol at right. The arrow shows one location where a microfault cuts an lpx phenocryst but not apparently the surrounding mesostasis. **(d)** False color BSE+EDS image of MET-I3, a holocrystalline *Vfr(AD)* inclusion that varies in texture from poikilitic enclosure of ol by lpx, to areas where mesostasis patches rich in pig and plag surround ol phenocrysts. Cr-spinel (sp, pink) and troi are accessory phases. **(e)** False color BSE+EDS image of Etr-I1, which contains ol and lpx phenocrysts and coarse phosphate (orange) including merrillite (merr) and Cl-apatite set in a plag-rich mesostasis (purple) with Cr-sp, ol, metal (blue) and phosphate veinlets. Diopside (diop, red) occurs as overgrowths on lpx only further from the coarse merr. The inclusion-host contact is blurred, and along one edge curved (below left). **(f)** False color BSE+EDS image of Jgo-I1, which contains ol grains set in a groundmass rich in plag and Cr-sp. Textures vary from barred olivine (BO), to microporphyritic olivine (mpO) to coarse olivine (CO, single grain outlined by dashes). Phosphate (phos), metal (blue), and troilite (yellow green) also occur in the mesostasis. The edge of the inclusion is marked by a plag-rich band that grades into the host and inclusion.

Fig. 6. Average mineral compositions in inclusions (data from Table A1, chemical types from Table 1) and shock melts (crosses), shown in a portion of the pyroxene quadrilateral, feldspar ternary, and an olivine Fa plot. Compositions found in type 4-6 H, L, and LL chondrites (equilibrated ordinary chondrites, EOC; Brearley and Jones, 1998) shown by ellipses for pyroxene and feldspar and by bars for olivine. **(a)** Mafic minerals. Lines between data points in the olivine plot connect multiple compositions in the same object. **(b)** Feldspathic phases. Plagioclase (p) and feldspar (f) by black font, glasses (g) by blue italics (inclusions) or green italics (impact melts). Labeled inclusions: 4686 = 4686-I1, glass only; 7872 = 7872-I1, both plagioclase and glass; 7873 = 7873-I1, glass only; E = Etr-I1, plagioclase and glass; G = Glk-I1, contains both feldspathic glass (fg) and mafic glass (mg); Q3 = QUE-I3, both plagioclase and glass; Q4 = QUE-I4, mixture of plagioclase and glass (p+g), M1 = McK-I1, both plagioclase and glass; ME2 = MET-I2, glass only; R = Rgl-I1, glass only; T1 = Tdk-I1, two plagioclases. Labeled shock melt glasses: 5964 = NWA 5964; 6454 = NWA 6454; 6579 = NWA 6579; 6580 = NWA 6580.

Fig. 7. Oxygen isotopic compositions of igneous inclusions and their host chondrites (data from Table 4, chemical types from Table 1). Inclusions with equilibrated Fe-Mg in olivine and low-Ca pyroxene are shown with asterisks in labels. Outlines show compositional ranges of type 4-6 H, L and LL chondrites after Clayton et al. (1991). **(a)** Chemical types of inclusions, compared to large chondrules in ordinary chondrites (Clayton et al., 1991; Bridges et al., 1998) and inclusion Bo-1 in Bovedy (Ruzicka et al., 1995). Lines connect values for different aliquots of the same inclusions. **(b)** *Unfr* (4686-I1, 4859-I18) and *Unfr+K* (869-I1, 8231-I1, Dim-I1) inclusions and hosts with small shifts in $\Delta^{17}O$ between inclusions and hosts. **(c)** *Unfr* (7871-I1, 8645-I1, Obl-I2) and *Unfr+K* (MET-I2) inclusions and hosts with large shifts in $\Delta^{17}O$ between inclusions and hosts. The dashed line shows a potential mixing line between Oberlin host and Obl-I2 samples. NWA 7871 is reclassified as LL6. **(d)** V*fr* inclusions (Lut-I1, MET-I1, MET-I3, QUE-I1, QUE-I2, QUE-I3, Rfd-I1) and hosts, all of which feature lower $\Delta^{17}O$ values in inclusions compared to hosts.

Fig. 8. Oxygen isotope reservoirs. The ordinate shows mean $\Delta^{17}O$ values for inclusions (chemical types as in Fig. 1) and hosts, and the abscissa differences in these values for hosts relative to inclusions (averaged data from Table 4). Lines connect hosts and inclusions. Inclusions with equilibrated olivine and low-Ca pyroxene are identified with asterisks. QUE-I1, I3 and I4 are assumed to represent one lithology, so one data point is shown for these, equal to the average composition of five analyses, excluding one slightly aberrant result (QUE-I3 split 4A, 1.583 mg sample). Group labels H, L, and LL are added to host data points; H, L and LL bars at right indicate the range of $\Delta^{17}O$ values in type 4-6 H, L and LL chondrites (after Clayton et al., 1991). Diagonal arrows indicate potential shifts to undo weathering-related effects for the hosts of 4686-I1 (NWA 4686), QUE-I1, -I2 and -I3 (QUE 97008), Lut-I1 (Lut 005), and Rfd-I1 (Richfield)—see Text. Small differences in $\Delta^{17}O$ occur between the inclusions 869-I1, 8231-I1 and Dim-I1 and their hosts, consistent with the formation of these inclusions from the same oxygen reservoir represented by the hosts. For most other cases, $\Delta^{17}O$ is significantly lower in inclusions compared to hosts, yielding host data points to the right (positive $\Delta^{17}O$ shifts). Three inclusions (notably 8645-I1) show the opposite trend, yielding host data points to the left (negative $\Delta^{17}O$ shifts). Significant positive or negative shifts can be explained in different ways (see Text).

Fig. 9. CI-chondrite-normalized element weight ratios [$(Al/Mg)_{CI}$ vs. $(Na/Mg)_{CI} + (K/Mg)_{CI}$] for large igneous inclusions and chondrite impact melts in this study (average CI chondrite composition of Anders and Grevesse (1989) used for normalization), compared to average composition of melt pockets (Dodd and Jarosewich, 1982; Dodd et al., 1982), average composition of L chondrite falls (Jarosewich, 1990), representative compositions of IA, IB, IIA and IIB chondrules (Lauretta et al., 2006; after Jones and Scott, 1989, and Jones 1990, 1994, 1996a), and equilibrium condensates / residues in a system with L chondrite bulk composition at 10^{-6} bar pressure and different temperature (T) (based on the CWPI program of Petaev and Wood (1998, 2005)). Three sets of representative mixing lines represent various proportions of whole rock L chondrite and condensates / residues of different composition. One inclusion, QUE-I1, plots outside the graph area [with $(Al/Mg)_{CI} = 5.1$, $(Na/Mg)_{CI} + (K/Mg)_{CI} = 3.8$] and may have been oversampled for mesostasis.

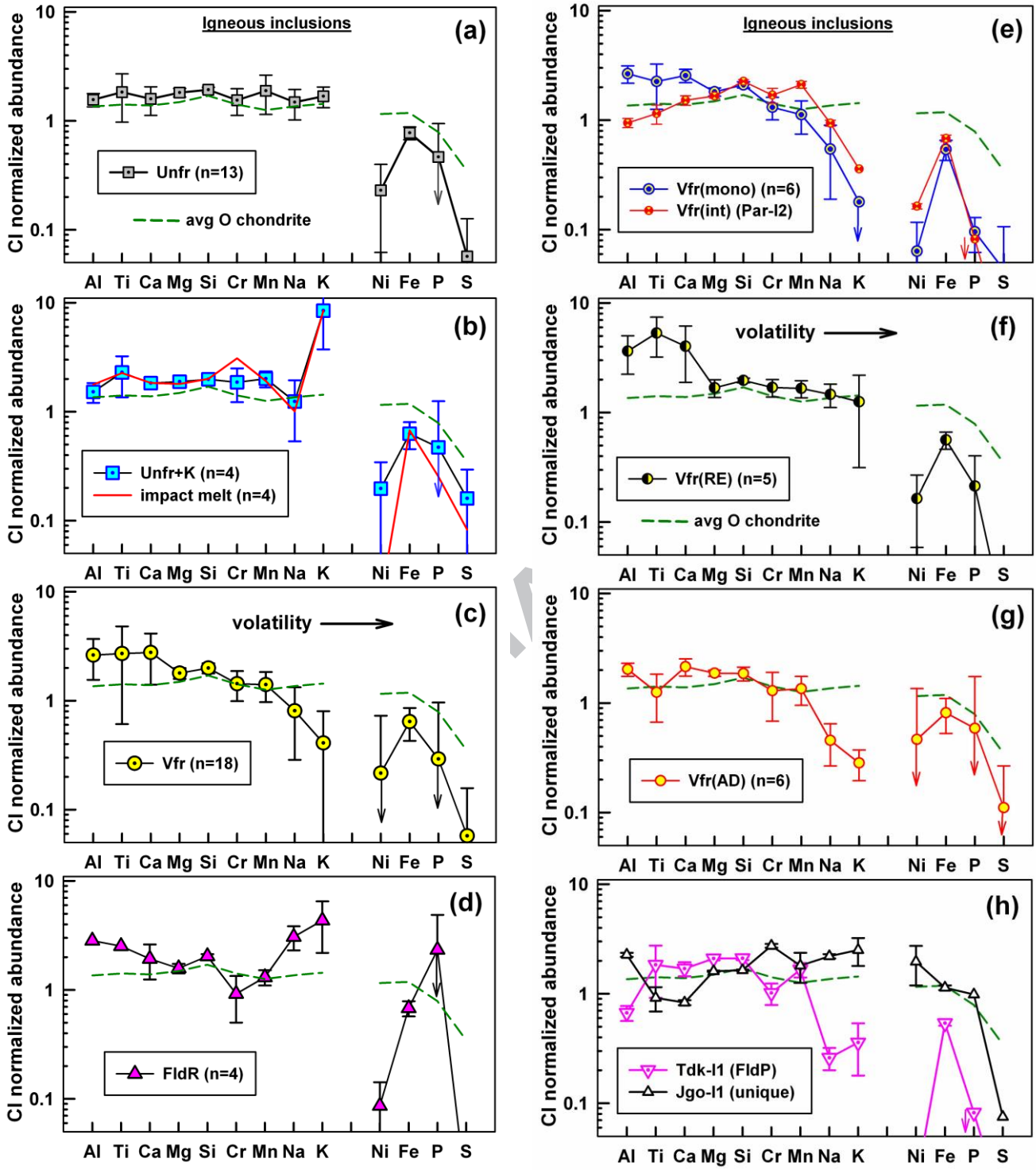

Fig. 1.

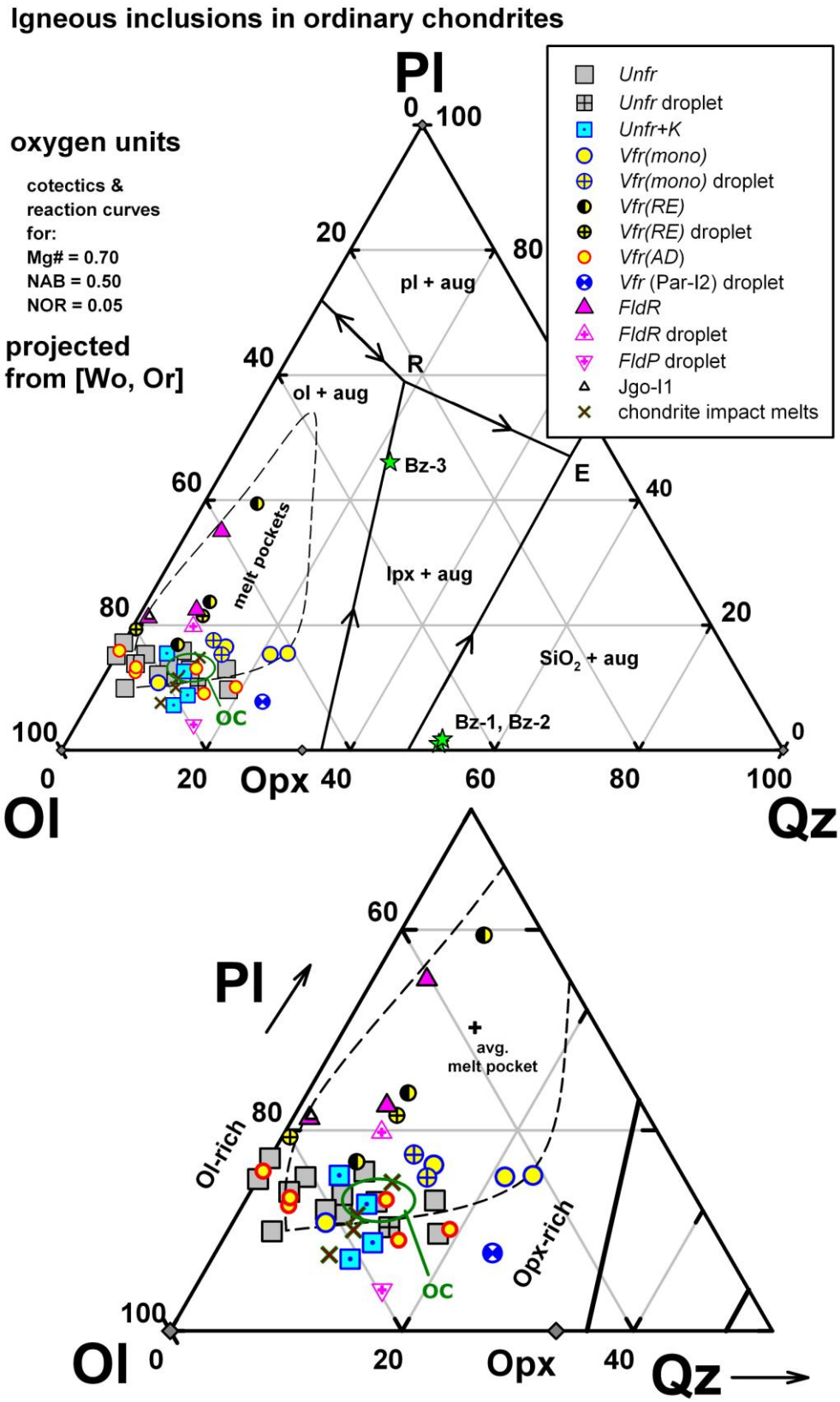
Igneous inclusions in ordinary chondrites
oxygen units
cotectics & reaction curves for:
Mg# = 0.70
NAB = 0.50
NOR = 0.05
projected from [Wo, Or]
Pl
Ol
Opx
Qz
pl + aug
ol + aug
lpx + aug
SiO2 + aug
R
E
Bz-3
Bz-1, Bz-2
melt pockets
OC
Unfr
Unfr droplet
Unfr+K
Vfr(mono)
Vfr(mono) droplet
Vfr(RE)
Vfr(RE) droplet
Vfr(AD)
Vfr (Par-I2) droplet
FldR
FldR droplet
FldP droplet
Jgo-I1
chondrite impact melts
avg. melt pocket
Ol-rich
Opx-rich

Fig. 2.

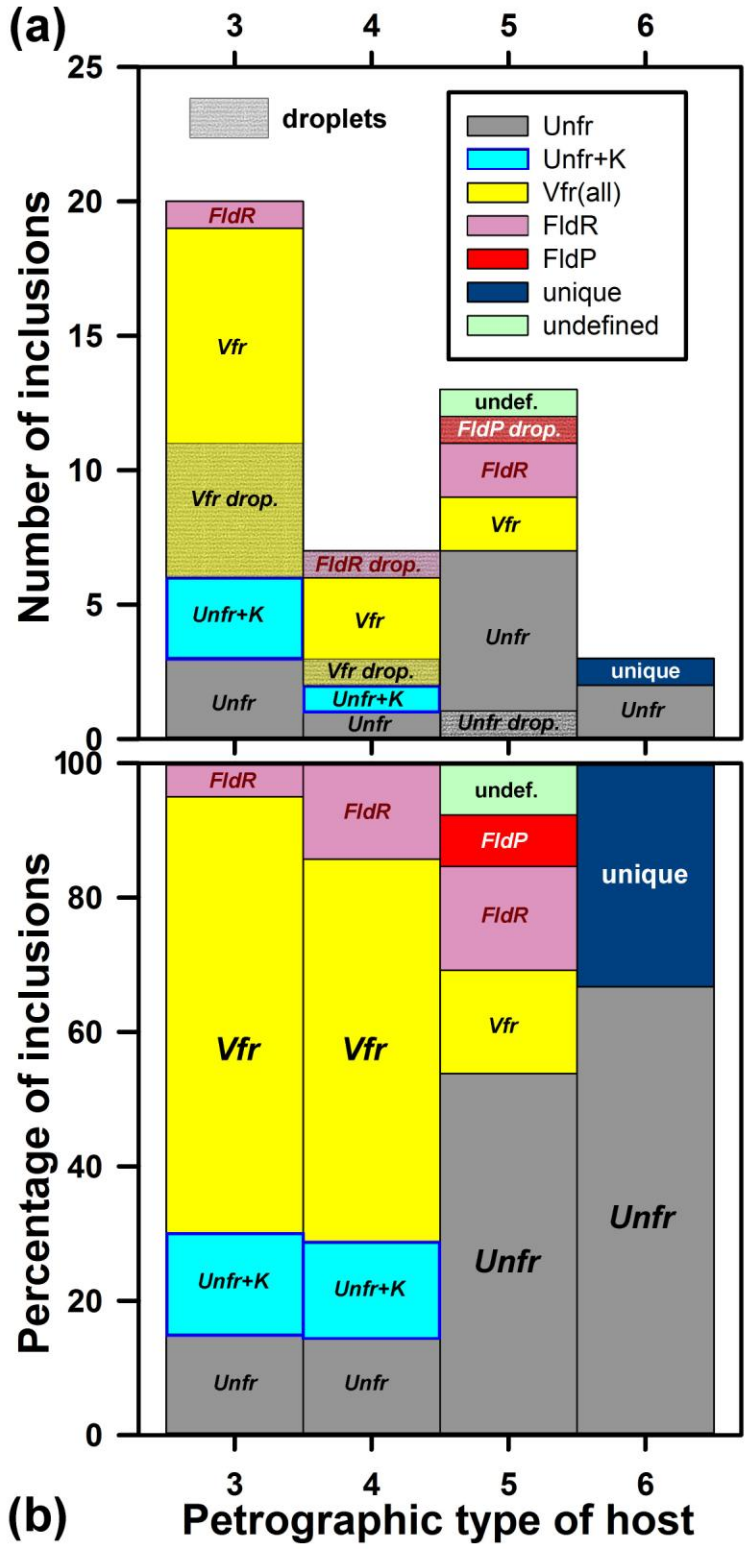
(a)
Number of inclusions
droplets
Unfr
Unfr+K
Vfr(all)
FldR
FldP
unique
undefined
FldR
Vfr
Vfr drop.
Unfr+K
Unfr
FldR drop.
Vfr
Vfr drop.
Unfr+K
Unfr
undef.
FldP drop.
FldR
Vfr
Unfr
Unfr drop.
unique
Unfr
(b)
Percentage of inclusions
Petrographic type of host
FldR
Vfr
Unfr+K
Unfr
FldR
Vfr
Unfr+K
Unfr
undef.
FldP
FldR
Vfr
Unfr
unique
Unfr

Fig. 3.

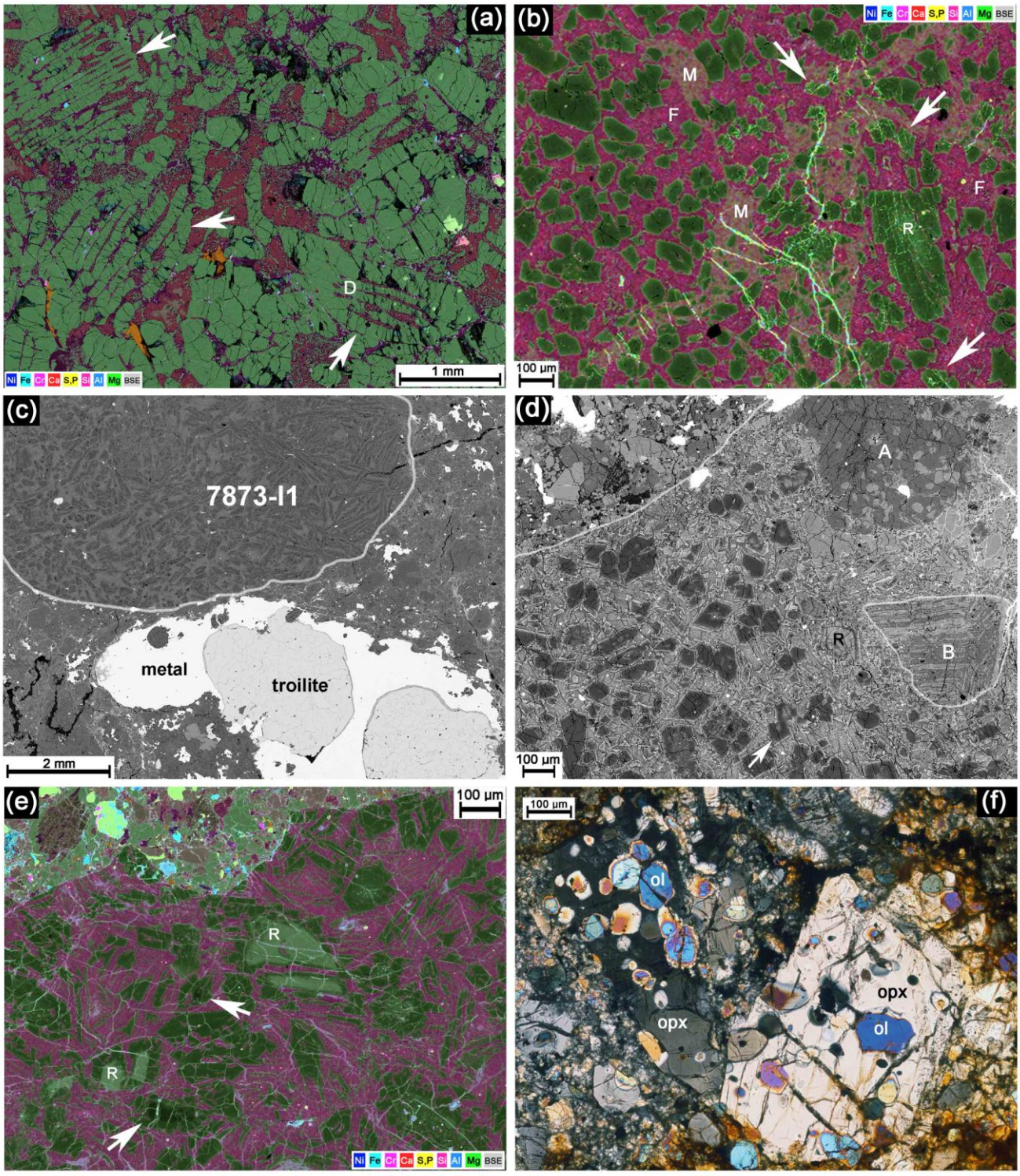
(a)
D
1 mm
Ni Fe Cr Ca S,P Si Al Mg BSE
(b)
M
F
M
F
R
100 µm
Ni Fe Cr Ca S,P Si Al Mg BSE
(c)
7873-I1
metal
troilite
2 mm
(d)
A
R
B
100 µm
(e)
100 µm
R
R
Ni Fe Cr Ca S,P Si Al Mg BSE
100 µm
(f)
ol
opx
opx
ol

Fig. 4.

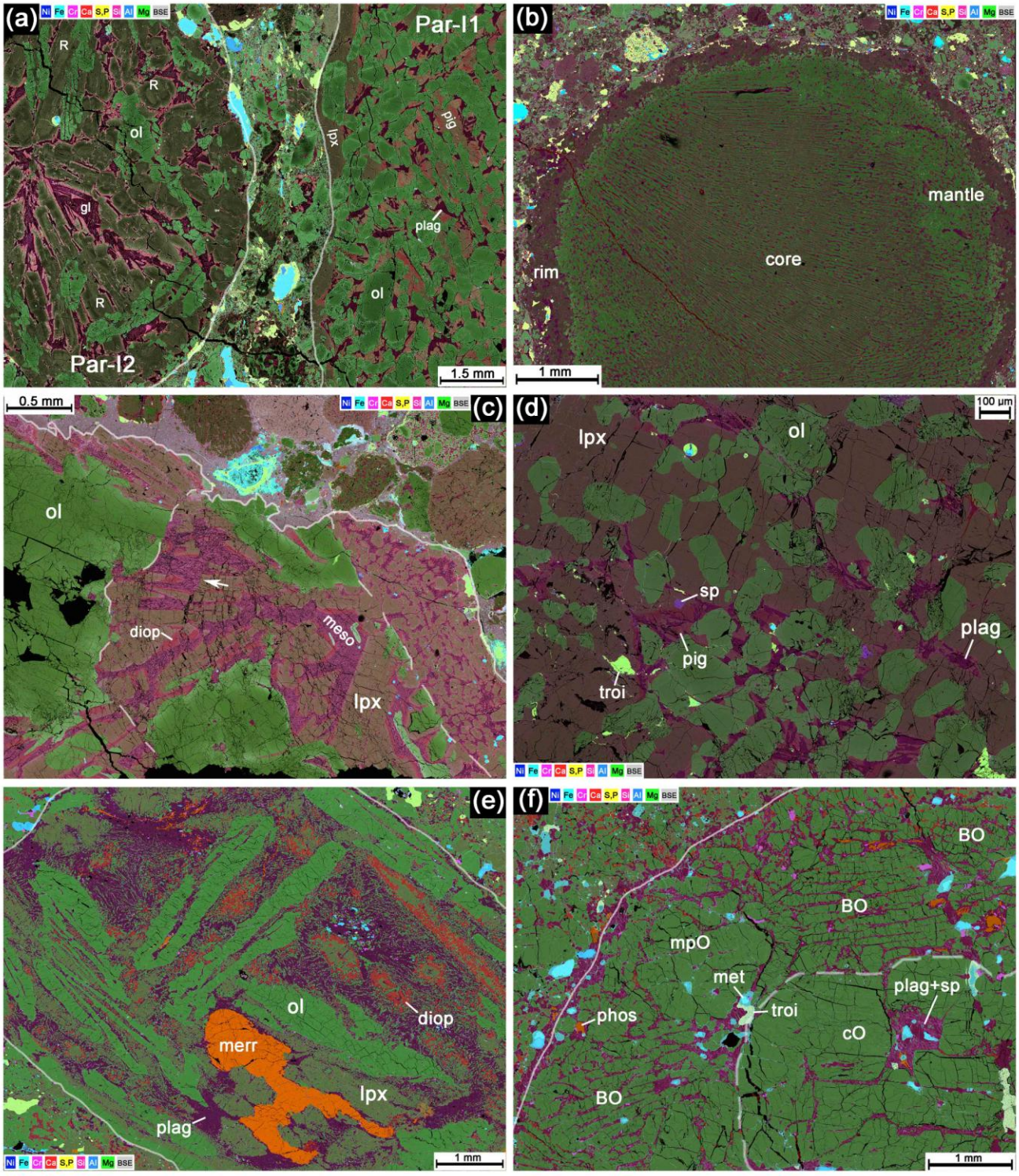
(a)
Par-I1
R
R
ol
gl
R
lpx
pig
plag
ol
Par-I2
1.5 mm
(b)
mantle
core
rim
1 mm
0.5 mm
(c)
ol
diop
meso
lpx
(d)
100 µm
lpx
ol
sp
plag
pig
troi
(e)
ol
diop
merr
lpx
plag
1 mm
(f)
BO
BO
mpO
met
plag+sp
phos
troi
cO
BO
1 mm

Fig. 5.

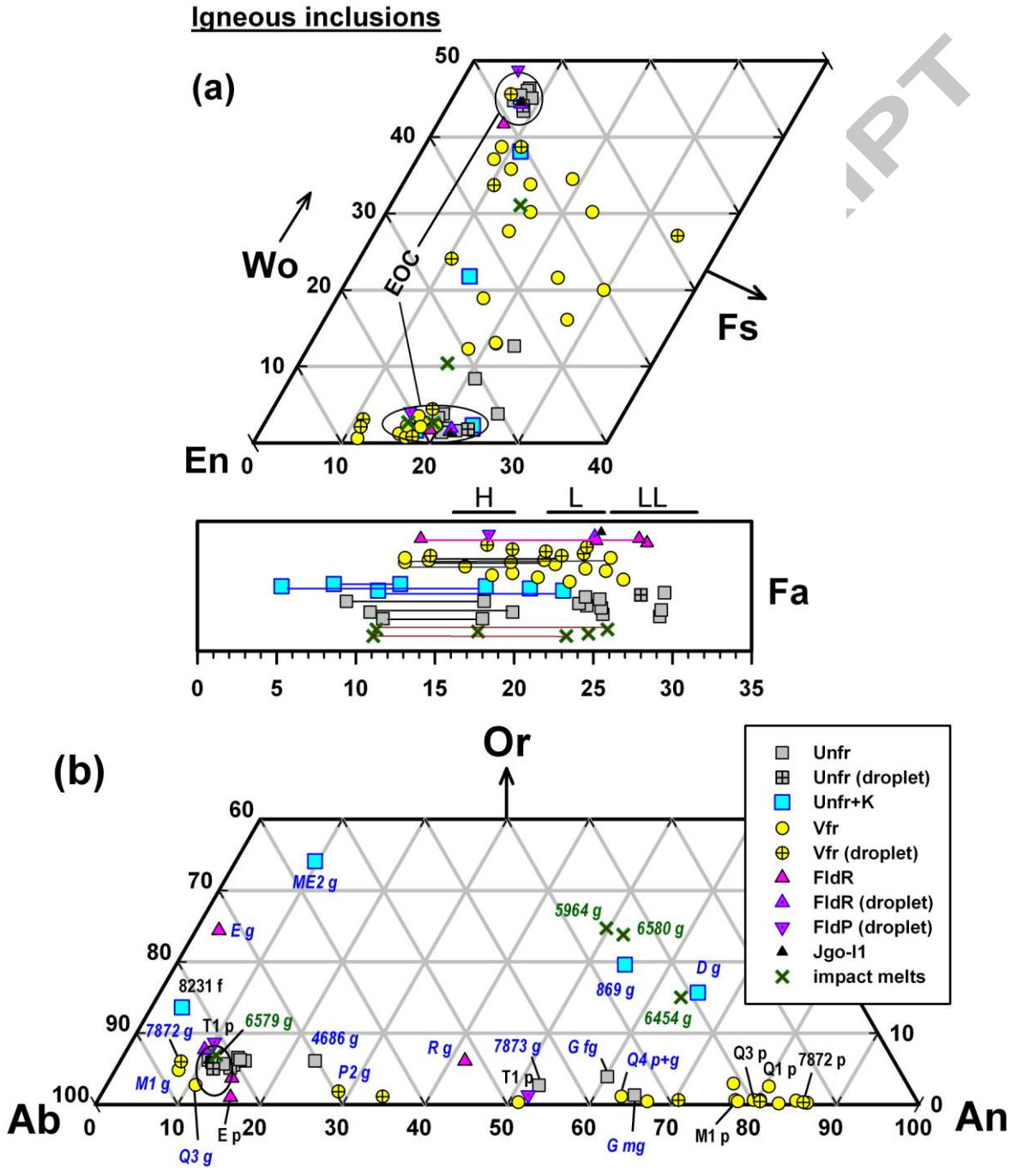

Fig. 6.

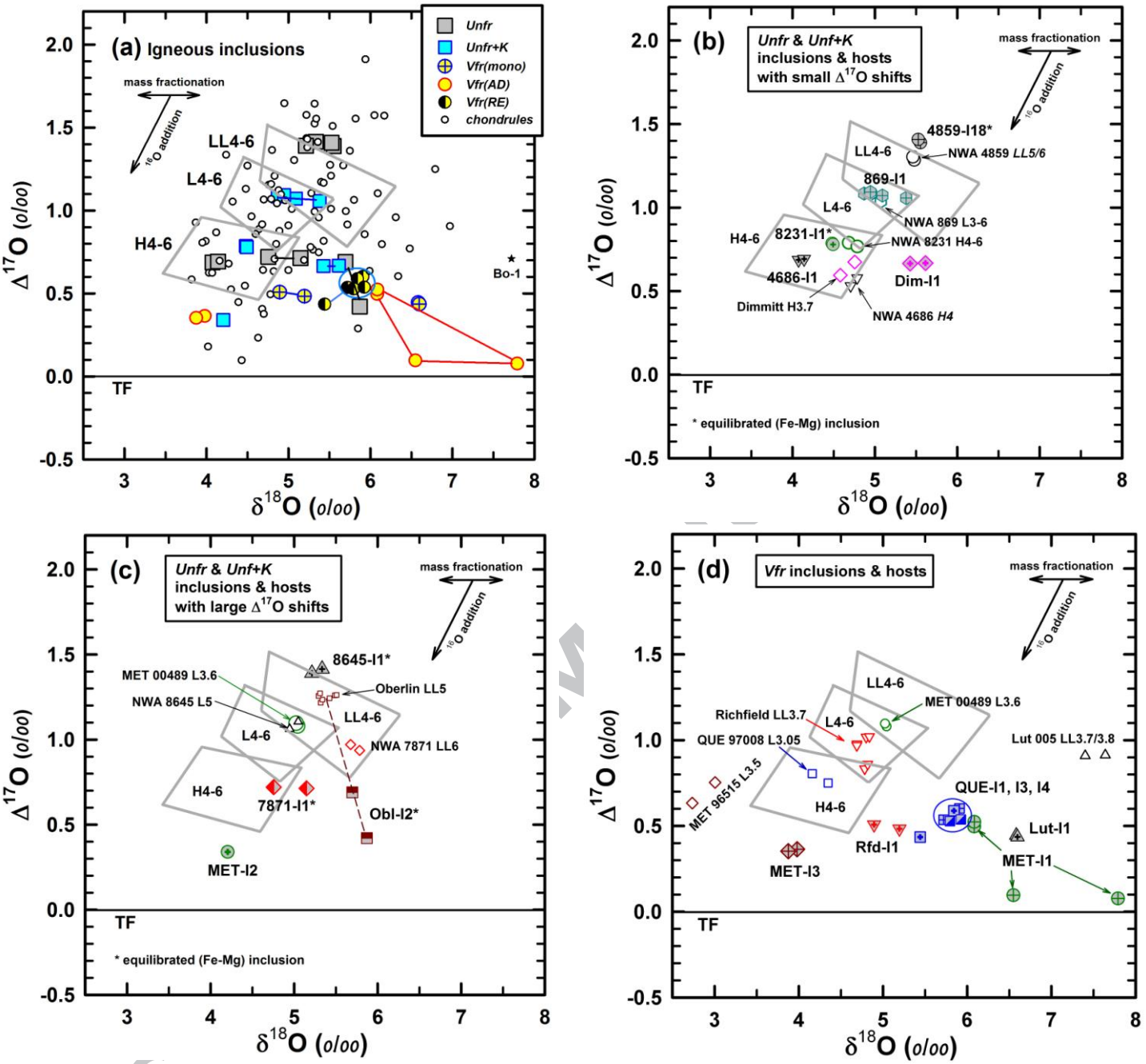

Fig. 7.

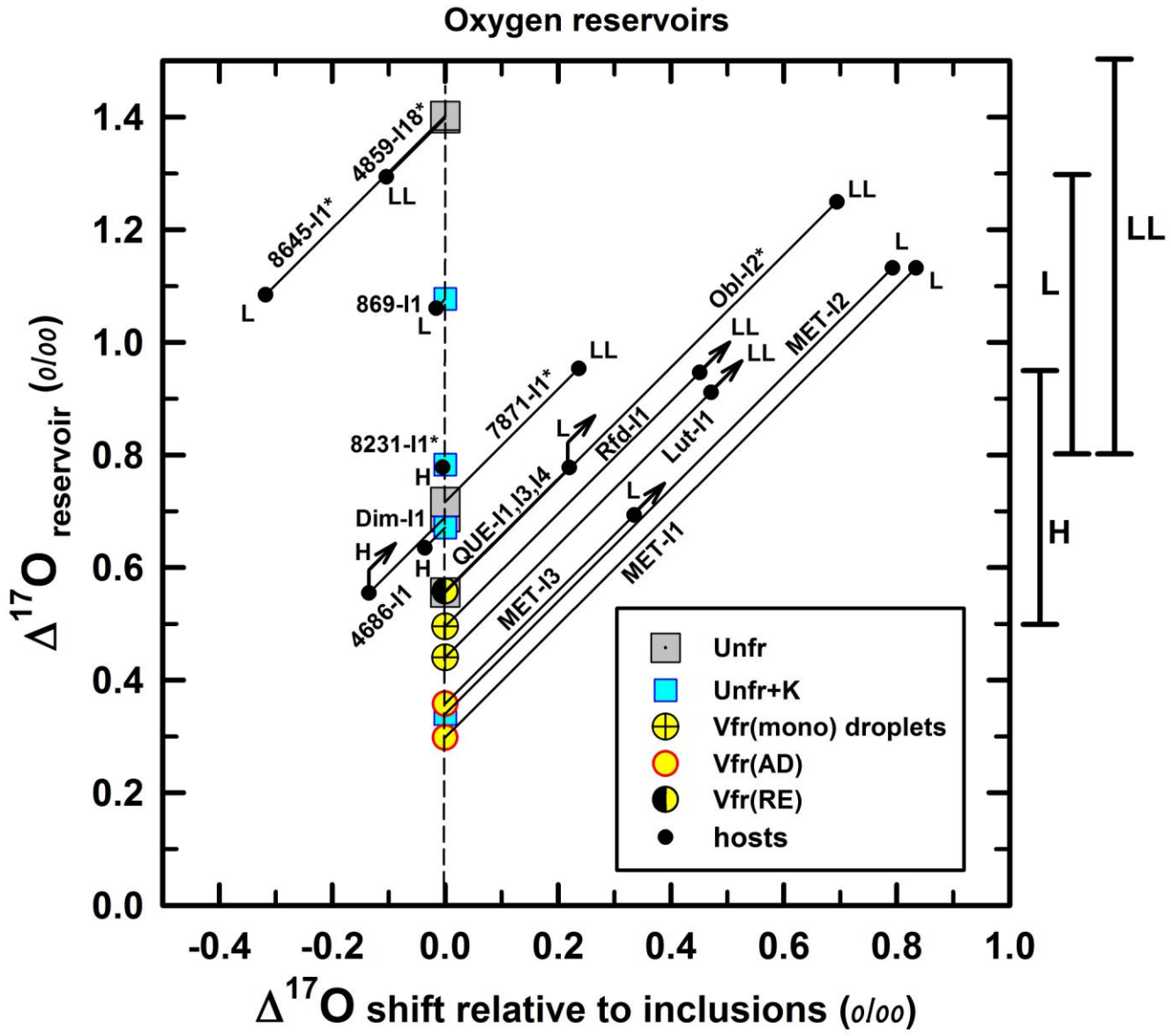

Fig. 8.

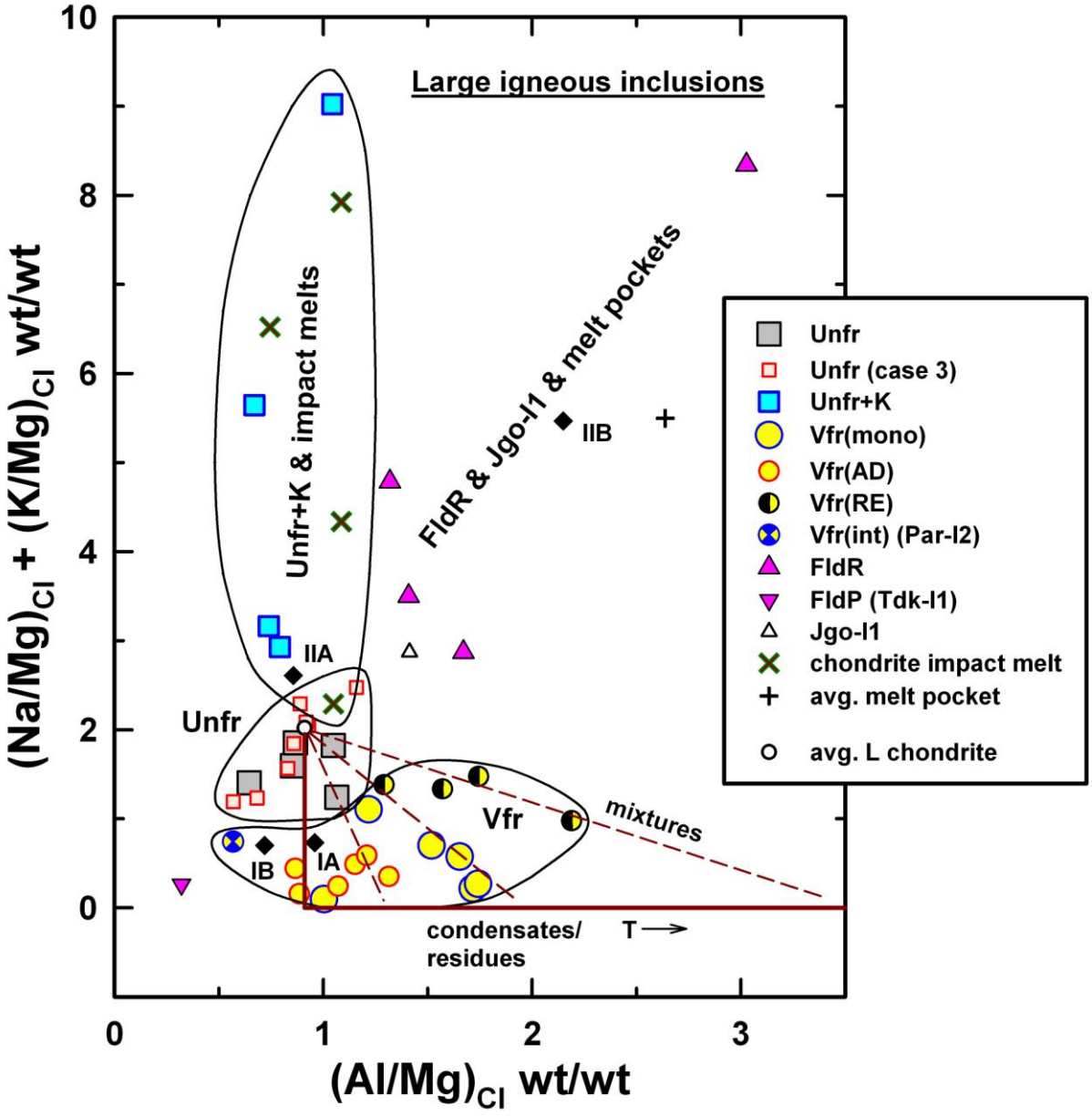

Fig. 9

Table 1. Forty-two large igneous inclusions in this study.

Inclusion[1]	Host (type)	Inclusion characteristics					
		Size (mm)	Texture-mineralogy	Droplet?[4]	Edge[5]	Fe-Mg uniform?	Bulk chemical

		[2]	type [3]			[6]	type [7]
869-I1* (CML 0074-13C)	NWA 869 (L3-6)	14 x 10	fine mpO	N	broken, intrusive	N	*Unfr+K*
4686-I1 (CML 0727-3A)	NWA 4686 (H4)	10	mpO	N	broken, sharp	N	*Unfr*
4859-I4*[§] (CML 0272-14)	NWA 4859 (LL5)	16	mpOP	N	px rim, shock vein	Y	*FldR*
4859-I18* (CML 0272-18-1)	NWA 4859 (LL5)	18	fine mpO	N	ol rim, ol+plag band	Y	*Unfr*
7869-I1* (CML 0143-1)	NWA 7869 (L3.7)	5.5	fine GO	Y	px rim	N	*Vfr(AD)*
7869-I2* (CML 0143-1)	NWA 7869 (L3.7)	3.5	mpOP	N	broken	N	*Vfr(mono)*
7870-I1* (CML 0173-3)	NWA 7870 (L4)	5	SO	Y	granular rim	Y	*FldR*
7871-I1* (CML 0178-2)	NWA 7871 (LL6)[9]	10 x 9	fine SOP-GO	N	granular rim	Y	*Unfr*
7872-I1* (CML 0359-3)	NWA 7872 (L3.7)	5	BO-GO	Y	granular rim	Y	*Vfr(RE)*
7873-I1* (CML 0615-2A)	NWA 7873 (H5-6)	8 x 6	mpO (spinifex)	N	broken, shock melt	N	*Unfr*
8141-I1* (CML 0014-1)	NWA 8141 (L3-6)	4 x 3	mpO	N	px + troi rim, broken	Y	*Unfr*
8231-I1* (CML 0368-1)	NWA 8231 (H4-6)	20 x 10	poik PO	N	broken	Y	*Unfr+K*
8232-I1* (CML 0372-4)	NWA 8232 (LL5)	7 x 4	fine mpO	N	plag & px+ol rim, blurred	Y	*Unfr*
8645-I1 (CML 0800-3)	NWA 8645 (L5)	8	mpO	N	plag at rim, blurred	Y (ol), N (lpx)	*Unfr*
Arm-I1* (AMNH 4461)	Armel (L5)	15	mpO	N	px at rim	N (ol) [8], N (lpx)	*Unfr*
Arm-I2* (AMNH 4461)	Armel (L5)	7	mpO	N	px at rim	N (ol) [8], Y (lpx)	*Unfr*
Cyn-I1* (AMNH 369-1)	Cynthianna (L4)	4.5	fine mpP	N	broken	Y (ol), N (lpx)	*Vfr(mono)*
Dim-I1 (AMNH 4488)	Dimmitt (H3.7)	20 x 10	mpO	N	broken	N	*Unfr+K*
Etr-I1*† (AMNH 4462-1)	Etter (L5)	13 x 6.3	pO	N?	ol rim, blurred	Y	*FldR*
Glk-I1*‡	Gunlock	18 x	fine mpO	N	shock	N	*Unfr*

(AMNH 4620-3)	(L3.6)	10			vein		
Jgo-I1[&] (CML 0414-1B)	Jungo 001 (L6)	8	BO/cO/mpO	N	plag band, blurred	Y (ol), N (lpx)	unique
Khr-I1* (AMNH 4245-1)	Khohar (L3.6)	3.5	mpO	N	shock vein	N	*Vfr(AD)*
KrC-I1* (AMNH 4428-1)	Kramer Creek (L4)	3.5	CC	Y	curved, abraded	Y	*Vfr(RE)*
Lut-I1* (CML 0740-3)	Lut 005 (LL3.7)	8	fine SOP-GO	Y	curved, granular rim	N	*Vfr(mono)*
McK-I1* (AMNH 391-1)	McKinney (L4)	3.5	fine mpO	N	shock melt	Y	*Vfr(AD)*
McK-I2* (AMNH 391-1)	McKinney (L4)	3	fine mpO	N	px at rim, shock melt	Y	*Vfr(AD)*
MET-I1 (MET 00489-22)	MET 00489 (L3.6)	10	poik PO	N	broken	N	*Vfr(AD)*
MET-I2 (MET 00489-26)	MET 00489 (L3.6)	4	mpO	N	broken	N	*Unfr+K*
MET-I3 (MET 96515-32)	MET 96515 (L3.5)	6 x 5	poik PO	N	broken	N	*Vfr(AD)*
Obl-I1* (AMNH 3832-1)	Oberlin (LL5)	6	mpO	N	broken	Y	Not defined
Obl-I2 (AMNH 3832)	Oberlin (LL5)	7	BOP	Y	curved, ol shell	Y	*Unfr*
Par-I1* (AMNH 1096-2)	Parnallee (LL3.6)	12	mpO	N	px at rim	N	*Vfr(mono)*
Par-I2* (AMNH 1096-2)	Parnallee (LL3.6)	3.2	mpP	Y	curved	N	*Vfr*
Par-I3* (CML 0524-2)	Parnallee (LL3.6)	7 x 6	CC	N	broken	Y	*Unfr*
PVM-I1*[#] (CML 0185-9B)	Palo Verde Mine (L6)	7 x 6	mpO	N	px, plag+sp at rim	Y (ol), N (lpx)	*Unfr*
QUE-I1 (QUE 97008,87)	QUE 97008 (L3.05)	6	mpPO	N	broken	N	*Vfr(RE)*
QUE-I3 (QUE 97008,86)	QUE 97008 (L3.05)	6	mpOP	N	broken	N	*Vfr(RE)*
QUE-I4 (QUE 97008,88)	QUE 97008 (L3.05)	7	pOP	N	broken	N	*Vfr(RE)*
Rfd-I1* (AMNH 4487)	Richfield (LL3.7)	5.5	fine SOP	Y	curved, granular px	N	*Vfr(mono)*
Rgl-I1* (AMNH 4825-3)	Ragland (LL3.4)	11	fine mpO	N	broken	N	*FldR*
Tdk-I1* (CML 0646-1-1)	Tamdahkt (H5)	4 x 3.3	fine RP	Y	curved, px at rim	Y (ol), N (lpx)	*FldP*

Tdk-I2* (CML 0646-2-1)	Tamdahkt (H5)	6	mpP-BO	N	broken, blurred	Y (ol), N (lpx)	*Vfr(mono)*

[1] Inclusion designation; sample number in parenthesis (CML = Cascadia Meteorite Laboratory, AMNH = American Museum of Natural History, MET and QUE designations are for Antarctic Meteorite samples). * Inclusions studied by Armstrong (2014). [§] Corresponds to LITE 4 of Jamsja and Ruzicka (2010). † Corresponds to Et-1 of Ruzicka et al. (1998). ‡ Corresponds to "golfball-sized chondrule" of Prinz et al. (1988); a separate thin section (4620-2) of the same object was studied as Gu-1 by Ruzicka et al. (1998). [#] Inclusion illustrated by Hutson et al. (2013). [&] Inclusion illustrated by Hutson and Ruzicka (2010).

[2] Approximate maximum diameter in exposed sections.

[3] Abbreviations: mpO = microporphyritic olivine (phenocrysts ~0.1-1 mm across, "fine" variety has phenocrysts ≤0.1 mm across), or coarser variant pO = porphyritic olivine (phenocrysts up to >1 mm across); mpOP = microporphyritic olivine-pyroxene or mpPO = microporphyritic pyroxene-olivine olivine (phenocrysts ~0.1-1 mm across, "fine" variety has phenocrysts ≤0.1 mm across), or coarser variant pOP = porphyritic olivine-pyroxene (phenocrysts up to >1 mm across); cO = coarse olivine grain; mpP = microporphyritic pyroxene (phenocrysts ~0.1-1 mm across); poik PO = poikilitic pyroxene-olivine; RP = radial pyroxene; BOP = barred olivine-pyroxene; CC = cryptocrystalline; GO = granular olivine; GP = granular pyroxene; SO = skeletal olivine; SOP = skeletal olivine-pyroxene.

[4] Y = yes, N = no.

[5] Inclusion edge character. Abbreviations: ol = olivine, px = pyroxene, plag = plagioclase, sp = spinel, mainly chromite, troi = troilite.

[6] Substantial Fe-Mg homogeneity in olivine (ol, standard deviation Fa<1) and low-Ca pyroxene (lpx, standard deviation Fs <1), Y = yes or N = no.

[7] Includes: *Unfr* = generally unfractionated abundances of lithophiles; *Unfr+K* = generally unfractionated abundances of lithophiles except for enrichment in K; *Vfr* = vapor-fractionated inclusions, abundances of lithophiles vary according to T_{c50} values; *Vfr(mono)* = vapor-fractionated inclusion subtype, abundances of lithophiles vary monotonically with T_{c50} values (depleted in volatiles); *Vfr(RE)* = vapor-fractionated inclusion subtype, abundances of refractory elements (Al, Ti, Ca) are enriched compared to other lithophile elements; *Vfr(AD)* = vapor-fractionated inclusion subtype, abundances of alkali elements (Na, K) are depleted compared to other lithophile elements; FldR = feldspar-rich, enriched in plagiophile elements (Al, Ca, Na, K); FldP = feldspar-poor, depleted in plagiophile elements (Al, Na, K).

[8] Nearly homogeneous olivine (standard deviation Fa = 1.0 and 1.2 for Arm-I1 and Arm-I2, respectively).

[9] Reclassified to LL6 from L6.

Table 2. Mean bulk compositions of inclusions as determined in this study, compared to average L chondrite*.

Inclusion chemical type	Wt%															
	SiO_2	TiO_2	Al_2O_3	Cr_2O_3	FeO	MnO	MgO	CaO	Na_2O	K_2O	P_2O_5	Cl	S	Fe(s)	Fe(m)	Ni
Unfr	44.5	0.14	2.60	0.61	15.9	0.49	30.3	2.09	1.02	0.11	0.13	0.05	0.36	0.55	0.89	0.26
[n = 13]	(2.2)	(0.06)	(0.35)	(0.17)	(2.9)	(0.20)	(3.1)	(0.60)	(0.32)	(0.02)	(0.14)	(0.08)	(0.43)	(0.80)	(0.60)	(0.19)
Unfr+K	45.7	0.17	2.54	0.74	10.6	0.53	31.4	2.41	0.85	0.58	0.12	0.03	1.01	1.76	1.37	0.22
[n = 4]	(1.5)	(0.07)	(0.54)	(0.26)	(5.4)	(0.09)	(3.9)	(0.15)	(0.48)	(0.32)	(0.22)	(0.03)	(0.84)	(1.58)	(0.80)	(0.16)
Vfr, all	45.7	0.20	4.33	0.56	12.6	0.36	29.6	3.62	0.55	0.03	0.08	0.03	0.36	0.63	1.16	0.26
[n= 18]	(4.8)	(0.16)	(1.80)	(0.18)	(3.0)	(0.11)	(3.4)	(1.84)	(0.36)	(0.03)	(0.19)	(0.05)	(0.63)	(1.05)	(2.84)	(0.55)
Vfr(mono)	47.9	0.17	4.35	0.51	11.6	0.29	29.8	3.32	0.37	0.01	0.02	0.04	0.27	0.48	0.77	0.07
[n = 6]	(3.1)	(0.07)	(0.79)	(0.12)	(2.3)	(0.10)	(2.6)	(0.47)	(0.23)	(0.00)	(0.01)	(0.08)	(0.40)	(0.70)	(0.85)	(0.06)
Vfr(RE)	45.4	0.39	6.06	0.67	11.8	0.43	28.0	5.34	1.00	0.07	0.06	0.03	0.09	0.10	0.30	0.18
[n = 5]	(2.4)	(0.16)	(2.37)	(0.13)	(3.3)	(0.08)	(5.1)	(2.88)	(0.24)	(0.04)	(0.06)	(0.05)	(0.07)	(0.13)	(0.24)	(0.12)
Vfr(AD)	42.7	0.09	3.34	0.50	13.9	0.35	31.1	2.78	0.31	0.02	0.16	0.01	0.69	1.23	2.39	0.51
[n = 6]	(6.3)	(0.04)	(0.43)	(0.25)	(3.5)	(0.11)	(2.4)	(0.49)	(0.13)	(0.01)	(0.33)	(0.00)	(0.98)	(1.58)	(4.87)	(0.98)
FldR	46.5	0.19	4.65	0.36	15.6	0.34	25.9	2.51	2.07	0.29	0.65	0.05	0.09	0.15	0.71	0.10
[n = 4]	(2.0)	(0.08)	(1.39)	(0.17)	(1.8)	(0.05)	(2.6)	(0.90)	(0.52)	(0.15)	(0.71)	(0.04)	(0.06)	(0.11)	(0.93)	(0.06)
FldP	47.9	0.14	1.10	0.40	13.0	0.43	34.4	2.19	0.17	0.02	<0.01	<0.01	0.07	0.13	0.03	0.02
(Tdk-I1)	(1.8)	(0.06)	(0.17)	(0.09)	(0.6)	(0.06)	(1.3)	(0.32)	(0.03)	(0.01)			(0.01)	(0.02)	(0.00)	(0.00)
Unique	38.7	0.07	3.87	1.12	13.5	0.48	27.4	1.12	1.53	0.17	0.29	0.04	0.49	0.87	8.09	2.25
(Jgo-I1)	(0.5)	(0.01)	(0.16)	(0.05)	(0.5)	(0.15)	(0.4)	(0.06)	(0.07)	(0.04)	(0.01)	(0.00)	(0.01)	(0.02)	(0.59)	(0.89)
All 42 inclusions[1]	45.1	0.17	3.49	0.57	14.0	0.42	29.8	2.75	0.88	0.13	0.16	0.04	0.38	0.65	1.16	0.28
	(3.1)	(0.10)	(1.07)	(0.18)	(2.9)	(0.13)	(3.1)	(1.09)	(0.35)	(0.07)	(0.21)	(0.05)	(0.49)	(0.86)	(1.58)	(0.34)
Avg. L chondrite[2]	39.7	0.12	2.25	0.53	14.5	0.34	24.7	1.85	0.95	0.11	0.22	nd	2.10	3.66	7.03	1.24
	(0.6)	(0.01)	(0.15)	(0.04)	(1.1)	(0.02)	(0.4)	(0.10)	(0.05)	(0.01)	(0.04)		(0.29)	(0.51)	(0.95)	(0.10)
Avg. inclusion/L[3]	0.99	1.24	1.36	0.94	0.84	1.08	1.06	1.30	0.81	1.03	0.64	nd	--	--	--	--
	(0.07)	(0.73)	(0.42)	(0.30)	(0.17)	(0.33)	(0.11)	(0.52)	(0.32)	(0.55)	(0.84)					

* Totals for inclusions originally 100% before rounding. ±1σ values given in parentheses. Averaged data exclude elevated values of Na and K in Lut-I1 that reflect alkali metasomatism and exclude individual Ni, K, S values that are likely overestimates (Table A3). n = number of inclusions averaged. Fe(s) = Fe in sulfide (troilite), Fe(m) = Fe in FeNi-metal. Inclusion types as in Table 1. [1] Includes defined inclusion types, as well as unique Jgo-I1 and undefined Obl-I1. [2] Jarosewich (1990), L chondrite falls; nd = not determined. [3] Concentration ratio, average (42 inclusions)/(L chondrite) on S-, Fe(s)-, Fe(m)-, Ni-free (metal-and-sulfide-free) basis, ±1σ value assumes errors for inclusions only.

Table 3. Bulk compositions of typical, silicate-rich portions of chondritic impact melt lithologies, as determined using the same methodology as for inclusions, compared to average inclusion of all chemical types and average inclusion of *Unfr+K* type.*

Sample	Wt%															
	SiO_2	TiO_2	Al_2O_3	Cr_2O_3	FeO	MnO	MgO	CaO	Na_2O	K_2O	P_2O_5	Cl	S	Fe(s)	Fe(m)	Ni
NWA 6454 melt[1] (CML 0273-1)	45.8 (1.4)	0.23 (0.08)	3.39 (0.41)	0.81 (0.23)	12.9 (1.2)	0.59 (0.17)	31.2 (1.0)	3.06 (0.41)	0.48 (0.11)	0.51 (0.11)	<0.01	<0.01	0.36 (0.18)	0.67 (0.33)	0.03 (0.001)	<0.01
NWA 6579 melt[2] (CML 0358-1)	47.1 (0.9)	0.14 (0.03)	2.97 (0.22)	0.79 (0.13)	15.5 (0.7)	0.62 (0.17)	28.3 (0.7)	2.23 (0.18)	1.19 (0.09)	0.15 (0.03)	0.07 (0.02)	<0.01	0.24 (0.05)	0.42 (0.09)	0.19 (0.003)	0.02 (0.003)
NWA 5964 melt[3] (CML 0175-4-1)	44.5 (1.2)	0.15 (0.02)	3.02 (0.12)	1.19 (0.43)	15.8 (0.5)	0.38 (0.02)	27.8 (0.9)	2.26 (0.10)	0.53 (0.02)	0.85 (0.04)	<0.01	<0.01	0.94 (0.33)	1.60 (0.60)	0.82 (0.03)	0.05 (0.009)
NWA 6580 melt[4] (CML 0371-1)	44.6 (1.6)	0.14 (0.04)	2.25 (0.14)	2.00 (0.33)	15.5 (0.6)	0.37 (0.02)	30.2 (1.2)	1.98 (0.11)	0.52 (0.03)	0.76 (0.05)	<0.01	<0.01	0.52 (0.38)	0.81 (0.68)	0.25 (0.02)	0.01 (0.003)
Average of 4 impact melts	45.5 (1.2)	0.16 (0.04)	2.91 (0.48)	1.20 (0.57)	14.9 (1.4)	0.49 (0.13)	29.4 (1.6)	2.38 (0.47)	0.68 (0.34)	0.57 (0.31)	0.03 (0.03)	<0.01	0.52 (0.31)	0.88 (0.51)	0.32 (0.35)	0.02 (0.02)
Avg. (incl.)/ (impact melt)[5]	0.99 (0.07)	1.1 (0.7)	1.2 (0.4)	0.48 (0.27)	0.94 (0.21)	0.86 (0.35)	1.0 (0.1)	1.2 (0.5)	1.3 (0.8)	0.22 (0.18)	5.3 (8.8)	--	0.73 (1.04)	0.74 (1.07)	3.6 (6.3)	14 (22)
Avg. (Unfr+K)/ (impact melt)[6]	1.0 (0.0)	1.1 (0.5)	0.87 (0.23)	0.62 (0.36)	0.71 (0.37)	1.1 (0.3)	1.1 (0.1)	1.0 (0.2)	1.3 (0.9)	1.0 (0.8)	4.0 (8.4)	--	1.9 (2.0)	2.0 (2.1)	4.3 (5.3)	11 (14)

* Totals originally 100% before rounding. ±1σ values given in parentheses.

[1, 2] L melt rock. [3] L3-6 breccia with abundant impact melt. [4] L melt breccia composed primarily of impact melt. [5] Concentration ratio, average (inclusion) / (impact melt); data for inclusions from Table 2. [6] Concentration ratio, average (*Unfr+K* inclusion) / (impact melt); data for *Unfr+K* inclusions from Table 2.

Table 4. Oxygen isotope data for igneous inclusions and host meteorites. Averaged data underlined, ±1σ values in parentheses.

			Inclusions			
Sample	Host	Mass (mg) [1]	$\delta^{17}O$ (‰)	$\delta^{18}O$ (‰)	$\Delta^{17}O$ (‰) [2]	$\Delta^{17}O$ (‰) linearized [3]
869-I1 (frag G)	NWA	3.0	3.616	4.869	1.084	1.061
	869	3.0 r	3.665	4.945	1.094	1.070
869-I1 (frag F)		2.6	3.855	5.379	1.058	1.033
		2.6 r	3.720	5.091	1.073	1.049
869-I1			3.714 (0.103)	5.071 (0.225)	1.077 (0.015)	1.053 (0.016)
4686-I1 (frag 9)	NWA	8.7	2.805	4.073	0.687	0.668
	4686	8.7 r	2.846	4.141	0.693	0.674
4686-I1			2.826 (0.029)	4.107 (0.048)	0.690 (0.004)	0.671 (0.004)
4859-I18 (frag I)	NWA	10.2	4.276	5.553	1.388	1.361
	4859	10.2 r	4.282	5.527	1.408	1.381
4859-I18			4.279 (0.004)	5.540 (0.018)	1.398 (0.014)	1.371 (0.014)
7871-I1 (piece G)	NWA	5.4	3.193	4.755	0.720	0.910
	7871	5.4 r	3.390	5.147	0.714	0.946
7871-I1			3.292 (0.139)	4.951 (0.277)	0.717 (0.005)	0.695 (0.006)
8231-I1 (frag 3)	NWA	6.6	3.117	4.482	0.786	0.766
	8231	6.6 r	3.115	4.492	0.779	0.758
8231-I1			3.116 (0.001)	4.487 (0.007)	0.783 (0.005)	0.762 (0.005)
8645-I1 (frag 4)	NWA	5.3	4.189	5.335	1.415	1.388
	8645	5.3 r	4.101	5.213	1.390	1.364
8645-I1			4.145 (0.062)	5.274 (0.086)	1.403 (0.017)	1.376 (0.017)
Dim-I1 (6-2-1)	Dimmitt	1.308	3.588	5.615	0.668	0.644
Dim-I1 (6-2-1)		1.328	3.488	5.428	0.665	0.642
Dim-I1 (6-2-2)		1.879	3.609	5.634	0.679	0.655
Dim-I1			3.562 (0.065)	5.559 (0.114)	0.671 (0.007)	0.647 (0.007)
Lut-I1 (powder)	Lut 005	4.8	3.868	6.583	0.445	0.418
		4.8 r	3.866	6.597	0.436	0.408
Lut-I1			3.867 (0.001)	6.590 (0.010)	0.440 (0.007)	0.413 (0.007)
MET-I1 (split B)	MET	5.7	3.501	6.548	0.096	0.070
	00489	5.7 r	4.128	7.790	0.077	0.048
MET-I1 (split A)		2.321	3.659	6.082	0.496	0.471
MET-I1 (split A)		2.259	3.687	6.084	0.523	0.498
MET-I1			3.744 (0.269)	6.626 (0.806)	0.298 (0.245)	0.272 (0.246)
MET-I2	MET	1.6	2.526	4.204	0.340	0.322

	00489					
MET-I3 (frag D)	MET	5.2	2.433	3.979	0.364	0.346
	96515	5.2 r	2.367	3.874	0.353	0.335
MET-I3			2.400 (0.047)	3.927 (0.074)	0.358 (0.008)	0.341 (0.008)
Obl-I2 (chip B)	Oberlin	2.122	3.473	5.870	0.421	0.396
Obl-I2 (chip B)		1.9	3.652	5.696	0.690	0.665
Obl-I2			3.563 (0.127)	5.783 (0.123)	0.555 (0.191)	0.531 (0.190)
QUE-I1 (frag B)	QUE	2.073	3.510	5.720	0.536	0.511
QUE-I1 (frag B)	97008	2.118	3.674	5.908	0.602	0.576
QUE-I1			3.592 (0.116)	5.814 (0.133)	0.569 (0.047)	0.544 (0.046)
QUE-I3 (split 4A)	QUE	1.583	3.265	5.442	0.435	0.412
QUE-I3 (split 4A)	97008	1.667	3.626	5.842	0.588	0.563
QUE-I3			3.446 (0.255)	5.642 (0.283)	0.512 (0.108)	0.488 (0.107)
QUE-I4 (frag 1)	QUE	3.8	3.541	5.795	0.528	0.503
	97008	3.8 r	3.618	5.925	0.537	0.512
QUE-I4			3.580 (0.054)	5.860 (0.092)	0.532 (0.007)	0.507 (0.006)
Rfd-I1 (frag A2)	Richfield	3.5	3.184	5.194	0.483	0.461
		3.5 r	3.052	4.893	0.508	0.486
Rfd-I1			3.118 (0.093)	5.044 (0.213)	0.495 (0.017)	0.473 (0.018)

			Host meteorites			
Sample	Group & type	Mass (mg) [1]	$\delta^{17}O$ (‰)	$\delta^{18}O$ (‰)	$\Delta^{17}O$ (‰) [2]	$\Delta^{17}O$ (‰) linearized [3]
NWA 869	L3.6	2.263	3.659	4.952	1.084	1.060
NWA 869		2.345	3.675	5.071	1.038	1.014
NWA 869			3.667 (0.011)	5.012 (0.084)	1.061 (0.032)	1.037(0.033)
NWA 4686	H4	2.280	2.978	4.705	0.531	0.511
NWA 4686		2.403	3.066	4.784	0.578	0.557
NWA 4686			3.022 (0.062)	4.745 (0.056)	0.555 (0.033)	0.534 (0.033)
NWA 4859	LL5	2.203	4.133	5.478	1.284	1.258
NWA 4859		2.244	4.144	5.462	1.304	1.277
NWA 4859			4.139 (0.008)	5.470 (0.011)	1.294 (0.014)	1.268 (0.014)
NWA 7871	LL6[5]	2.234	3.944	5.784	0.936	0.910
NWA 7871[4]		2.297	3.923	5.676	0.971	0.946
NWA 7871			3.934 (0.015)	5.730 (0.076)	0.954 (0.025)	0.928 (0.025)
NWA 8231	H4-6	2.347	3.224	4.682	0.789	0.768
NWA 8231		2.319	3.256	4.786	0.767	0.745

NWA 8231			3.240 (0.023)	4.734 (0.074)	0.778 (0.016)	0.757 (0.016)
NWA 8645	L5	2.354	3.635	4.946	1.063	1.040
NWA 8645		2.317	3.731	5.048	1.106	1.082
NWA 8645			3.683 (0.068)	4.997 (0.072)	1.085 (0.031)	1.061 (0.030)
Dimmitt (host 2)	H3.7	2.357	3.147	4.754	0.675	0.654
Dimmitt (host 2)		2.368	2.977	4.581	0.595	0.574
Dimmitt			3.062 (0.120)	4.668 (0.122)	0.635 (0.057)	0.614 (0.056)
Lut 005	LL3.7	2.339	4.886	7.640	0.913	0.881
Lut 005		2.344	4.758	7.401	0.909	0.878
Lut 005			4.822 (0.091)	7.521 (0.169)	0.911 (0.003)	0.879 (0.002)
MET 00489,21	L3.6	2.285	3.702	5.042	1.080	1.056
MET 00489,21		2.310	3.708	5.023	1.096	1.072
MET 00489,21		2.340	3.912	5.175	1.221	1.196
MET 00489			3.774 (0.120)	5.080 (0.083)	1.132 (0.077)	1.108 (0.077)
MET 96515,31[4]	L3.5	2.368	2.317	3.006	0.754	0.739
MET 96515,31[4]		2.055	2.055	2.735	0.633	0.620
MET 96515			2.186 (0.185)	2.871 (0.192)	0.693 (0.086)	0.680 (0.085)
Oberlin (frag 4)	LL5	1.557	4.034	5.311	1.272	1.247
Oberlin (frag 3)		2.297	4.064	5.424	1.244	1.217
Oberlin (frag 3)		2.333	4.009	5.292	1.257	1.232
Oberlin (frag B2-2)		2.398	4.114	5.488	1.260	1.234
Oberlin (frag B2-2)		2.240	4.127	5.509	1.262	1.236
Oberlin (frag B2-1)		2.300	3.983	5.319	1.217	1.192
Oberlin (frag B2-1)		2.257	4.010	5.337	1.235	1.209
Oberlin			4.049 (0.055)	5.383 (0.090)	1.250 (0.019)	1.224 (0.019)
QUE 97008,82	L3.05	2.218	3.011	4.347	0.751	0.731
QUE 97008,82		2.180	2.968	4.159	0.805	0.786
QUE 97008			2.990 (0.030)	4.253 (0.133)	0.778 (0.039)	0.758 (0.039)
Richfield (split C)	LL3.7	2.267	3.537	4.838	1.021	0.998
Richfield (split C)		2.346	3.513	4.799	1.018	0.995
Richfield (split A)		2.273	3.417	4.690	0.978	0.956
Richfield (split A)		2.309	3.407	4.688	0.969	0.947
Richfield (split B)		2.320	3.320	4.782	0.833	0.811
Richfield (split B)		2.374	3.365	4.817	0.860	0.838
Richfield			3.427 (0.084)	4.769 (0.065)	0.947 (0.081)	0.924 (0.080)

[1] r = replicate analyses on same subsample. [2] $\Delta^{17}O = \delta^{17}O - 0.52\ \delta^{18}O$. [3] $\Delta^{17}O$ linearized = $1000\ \{\ln[1 + \delta^{17}O_{SMOW}/1000)] - 0.5247\ \ln[1 + \delta^{18}O_{SMOW}/1000)]\}$. [4] Trace NF_2 detected during analysis, a signature of N in the sample that can lead to an isobaric interference on $^{17}O^{16}O$ (Miller et al., 1999). [5] Reclassified to LL6 from L6.

Table 5. Relative timing of melting and metamorphic events for inclusions, inferred from petrographic-chemical data.

Inclusion (host group & type)	Inference[1]	Rationale
4686-I1 (H4), 7873-I1 (H5-6)	Melted after host metamorphism (Case 1a).	Glass-rich mesostases & zoned olivine phenocrysts, sharp contact with host, host equilibrated.
869-I1 (L3-6)	Melted after host metamorphism & mixing of metamorphic grades (Case 1b).	Glass-rich mesostasis & zoned olivine phenocrysts, partly sharp, partly intrusive contact with host.
8231-I1 (H4-6)	Melted & homogenized, not metamorphosed *in situ* (Case 2a)	Homogenous Fe-Mg in olivine, different than that of homogenous host, sharp contact with host.
8141-I1 (L3-6)	Melted & homogenized, not metamorphosed *in situ* (Case 2b).	Homogenous Fe-Mg in olivine, partly blurred & partly broken contact with host, unequilibrated type 3 lithology in host.
*8645-I1 (L5)**, Arm-I1 (L5), Arm-I2 (L5), Cyn-I1 (L4), *Jgo-I1 (L6)**, PVM-I1 (L6), Tdk-I1 (H5), *Tdk-I2 (H5)**	Melted before/during host metamorphism, with incomplete Fe-Mg homogenization (Case 3a).	Slight Fe-Mg inhomogeneity in olivine & pyroxene, some blurred contacts with host.
4859-I4 (LL5), 4859-I18 (LL5), 7871-I1 (LL6)[2], *8232-I1 (LL5)**, *Etr-I1 (L5)**, McK-I1 (L4), McK-I2 (L4), Obl-I1 (LL5), Obl-I2 (LL5)	Melted before/during host metamorphism, with complete Fe-Mg homogenization (Case 3b).	Homogenous Fe-Mg in olivine & pyroxene, some blurred contacts with host.
7870-I1 (L4), 7872-I1 (L3.7), KrC-I1 (L4), Par-I3 (LL3.6)	Homogeneity by rapid crystallization, not *in situ* metamorphism (Case 4).	Olivine uniform Fe-Mg, host less so, sharp contact with host, textures compatible with rapid crystallization.
7869-I1 (L3.7), 7869-I2 (L3.7), Dim-I1 (H3.7), Glk-I1 (L3.6), Khr-I1 (L3.6), Lut-I1 (LL3.7), MET-I1 (L3.6), MET-I2 (L3.6), MET-I3 (L3.5), Par-I1 (LL3.6), Par-I2 (LL3.6), QUE-I1 (L3.05), QUE-I3 (L3.05), QUE-I4 (L3.05), Rfd-I1 (LL3.7), Rgl-I1 (LL3.4)	Not significantly metamorphosed (Case 5).	Zoned olivine phenocrysts, sharp contacts with host, host low subtype.

* Texturally blurred inclusion-host boundary, evidence for *in situ* metamorphism. [1] For explanation of different cases, see Text. [2] Reclassified to LL6 from L6.

Table 6. Inferences pertaining to oxygen isotope reservoirs and inclusion petrogenesis.

Inclusion	Inference
869-I1	Melting of L-like source, incorporated in L body. No shift in $\Delta^{17}O$ compared to host, consistent with melting of host.
4686-I1	Melting of H-like source, incorporated in H body. Small shift in $\Delta^{17}O$ compared to host, possible differential weathering effect (inclusion less affected).
4859-I18	Melting of LL-like source, incorporated in LL body. Small shift in $\Delta^{17}O$ compared to host, O not re-equilibrated.
8231-I1	Melting of H-like source, incorporated in H body. No shift in $\Delta^{17}O$ compared to host, consistent with melting of host.
Dim-I1	Melting of H-like source, incorporated in H body. No shift in $\Delta^{17}O$ compared to host, consistent with melting of host, but would require mass fractionation to produce isotopically heavier inclusion.
7871-I1	Melting of H-like source, incorporated in LL body, O not re-equilibrated.
8645-I1	Melting of LL-like source, incorporated in L body, O not re-equilibrated.
Lut-I1	Melting in distinctive reservoir, incorporation in LL body.
MET-I1	Melting in distinctive reservoir, incorporation in L body.
MET-I2	Melting in distinctive reservoir, incorporation in L body.
MET-I3	Melting in distinctive reservoir, incorporation in L body.
Obl-I2	Melting in distinctive reservoir, incorporated in LL body, O partially re-equilibrated.
QUE-I1, I3, I4	All 3 inclusions derived by melting of the same, distinctive reservoir (extension of H), incorporated in L body.
Rfd-I1	Melting in distinctive reservoir (extension of H), incorporated in LL body.

Table 7. Six similarities and differences between chondrules and most large igneous inclusions in ordinary chondrites.

Similarities	Differences
1. Normative compositions	1. Much larger sizes for inclusions
2. Overall textures, prevalence of microporphyries	2. Little magnesian olivine or magnesian low-Ca pyxroxene in inclusions
3. Mineralogies, including clinoenstatite	3. No relict dusty olivine grains in inclusions
4. Can have pyroxene rims	4. No relict forsterite grains in inclusions
5. Oxygen isotope compositions (larger chondrules)	5. Some inclusions contain chondritic clasts
6. Have high Na/Al and low Na/Al groups*	6. Some inclusions have olivine “donut” textures or multi-mm grains

* Ruzicka et al. (1998)

ELECTRONIC ANNEX

for “Petrology and oxygen isotopic composition of large igneous inclusions in ordinary chondrites: Early solar system igneous processes and oxygen

reservoirs", authors Alex M. Ruzicka, Richard C. Greenwood, Katherine Armstrong, Kristy L. Schepker, Ian A. Franchi

Contents

Experimental techniques. Various experimental techniques were used to study inclusions. This included optical microscopy (OM), scanning electron microscopy (SEM), electron microprobe analysis (EMPA), and laser fluorination and mass spectrometry of bulk samples for analysis of oxygen isotopes.

All inclusions were studied in polished thin section or polished slice using OM and SEM methods at Portland State University (PSU). Petrographic OM data were obtained using a Leica DM 2500 microscope. A Zeiss Sigma Variable Pressure-Field Emission-Scanning Electron Microscope (VP-FE-SEM) with an attached high-efficiency XMax50 silicon-drift energy dispersive spectrometer (EDS) was used to obtain major-element chemical and additional petrographic data. The SEM was operated at 15 keV accelerating voltage and beam currents of ~5-10 nA. AZtec 3.1 and 3.2 Oxford Instruments Nanoanalysis software was used with the SEM to map inclusions at various magnifications with backscattered electron (BSE) images (2048 x 1646 pixels) and EDS maps (1024 x 768 pixels) for each field. These data were used to create standardized false color phase images, by associating characteristic X-ray intensities for different

elements to different colors and BSE intensity to overall brightness. Each map contains 4-60 fields covering all or most of the inclusions, and each field has ~80-90 million total X-ray counts obtained with an EDS counting duration of ~16 min (150 µs dwell per pixel per frame, 4 frames). The false color maps were used to determine modes for inclusions, for phases with ≥0.1 area %, by using ImageJ and Color Inspector 3D plug-in to group pixels into 10-35 color bins, assigning these colors to various phases, and summing the pixels for these phases to determine areal fractions. Precision in modes for different phases was estimated by varying the number of color bins, and equating error to the standard deviation of areal fractions. Quantitative phase chemical data were obtained from point analyses (with analytical counting times of 20 seconds), or in some cases from user-defined extracts from EDS maps, by converting count rate data to concentrations using energy and beam calibration on a pure Cu standard and factory quantitative standardizations for elements of interest. Although included in the spectra, oxygen was calculated by stoichiometry for all phases except metals and sulfide. Analyses were accepted if mineral stoichiometry was acceptable, including 2.0 ± 0.05 (Mg+Fe)/Si cations for olivine, 1.0 ± 0.05 (Mg+Fe+Ca)/Si cations for pyroxene, and 0.25 ± 0.03 (Na+K+Ca)/(Si+Al) cations for feldspar. Most accepted analyses for olivine, pyroxene, and feldspar were within ± 0.02 cations of ideal stoichiometry on this basis.

Quantitative major element chemical data were obtained with an SX-100 Cameca electron microprobe at Oregon State University that was remotely accessed from PSU. The electron microprobe was operated at 15 keV accelerating voltage, beam currents of 10-50 nA, and beam size focused to ~1 µm. Wavelength dispersive spectrometry (WDS) methods, well-characterized mineral and glass standards, and the PAP correction procedure (Pouchou and Pichoir, 1991) were used. Various phases in thirteen inclusions (4859-I18, 7871-I1, 8645-I1, Etr-

I1, Glk-I1, Khr-I1, MET-I1, MET-I2, MET-I3, Par-I1, Par-I2, QUE-I3, Tdk-I2) were studied with EMPA. Analyses were accepted if totals were between 97-102 wt% and mineral stoichiometry was acceptable using the same criteria as for SEM analysis. Phase composition datasets for these inclusions were obtained by merging EMPA and SEM data.

Bulk chemical compositions for inclusions were calculated by modal reconstruction, combining modes with mean phase compositions. Areal modes were assumed to be the same as volumetric abundances and were converted to weight fractions using mineral densities from Klein and Dutrow (2007). Errors in bulk compositions reflect uncertainties in both phase compositions (equated to standard deviations of mean compositions) and modes.

Oxygen isotope analysis was performed for aliquots of bulk samples of sixteen inclusions and their host meteorites that were mechanically separated from one another by various means. Separation methods included a combination of cutting (using diamond-impregnated blade saws with either de-ionized water or isopropyl alcohol as cutting fluid), abrasion (SiC grinding paper with de-ionized water), crushing (agate mortar and pestle), or breaking (stainless steel pick). Any fusion crust was removed. Analyzed aliquots were typically 2-5 mg, with most host aliquots being subsamples of larger samples. All analyzed inclusion and host aliquots were judged to be 100% pure by examination with a binocular microscope. Three-isotope analysis was performed by infrared (10 μm wavelength) laser-assisted fluorination coupled with high-mass-resolution mass spectrometry at the Open University, following the procedures of Miller et al. (1999). System precision (2σ) for $\delta^{17}O$, $\delta^{18}O$, and $\Delta^{17}O$ (= $\delta^{17}O - 0.52\ \delta^{18}O$) is estimated as ±0.05‰, ±0.09‰, and ±0.02‰, respectively.

For oxygen isotope analysis, no attempt was made to treat samples for terrestrial weathering, such as by use of an EATG treatment that has been used to remove weathering

products in meteorites (Martins et al., 2007; Greenwood et al., 2007, 2015). Reasons for this include the following: (1) terrestrial weathering products are more likely to affect oxygen isotope compositions for metal-rich samples (Greenwood et al., 2007), and inclusions are metal poor; (2) the studied inclusions typically show little evidence for weathering, beyond mild staining in some cases; and (3) larger samples (20 mg or more) are usually required for the EATG technique and available sample mass was insufficient.

Assessment of terrestrial weathering effects in analyses of oxygen isotopes. There is evidence that some chondrite hosts have oxygen isotope compositions that were affected by climate-dependent weathering on Earth (Sec. 3.3). Terrestrial weathering of ordinary chondrites in non-Antarctic environments typically causes shifts to higher $\delta^{18}O$ and lower $\Delta^{17}O$ (Clayton et al., 1991; Stelzner et al., 1999; Bland et al., 2000), whereas weathering in Antarctic environments causes shifts to lower $\delta^{18}O$ and lower $\Delta^{17}O$ (Bland et al., 2000; Greenwood et al., 2012). Below, we review evidence for terrestrial weathering in some inclusion-host pairs, focusing on those cases in which hosts have discrepant oxygen isotope compositions.

We suggest that NWA 4686 (H4), found in the Sahara, experienced a modest weathering-related fractionation but that inclusion 4686-I1 was little affected. Compared to the inclusion it contains, the host has slightly lower $\Delta^{17}O$ (by ~0.15‰) and somewhat higher $\delta^{18}O$ (by ~0.6‰) (Fig. 7b). This can be explained by hot-desert weathering preferentially affecting the host, but not so significantly that the host was shifted completely out of the H field (Fig. 7b). In contrast, the inclusion lies squarely in the H field (Fig. 7b) with no evidence for a weathering-related shift.

As previously noted (Sec. 3.3), LL-like oxygen values for NWA 7871 could indicate that this meteorite is actually LL6, not L6 as originally classified, an explanation compatible with the originally-recognized L/LL-like transitional character of metal and sulfide contents and olivine

compositions of this meteorite. However, it is also possible that $\delta^{18}O$ of the host was increased and $\Delta^{17}O$ was little changed by weathering in a hot desert environment. The opposite would be required to explain inclusion 7871-I1, which compared to L chondrites would require little change in $\delta^{18}O$ but possibly a small decrease in $\Delta^{17}O$ (Fig. 7c). Although two different weathering styles could be invoked for inclusion and host, an alternative interpretation that neither host nor clast was much affected by terrestrial weathering is also consistent with the data.

Oxygen isotope compositions of Richfield aliquots (classified LL3.7, or more properly LL3.7-5; Rubin et al., 1996) fall within the L4-6 field (Fig. 7d), which might suggest misclassification. However, an LL designation seems secure for Richfield, based on CRE exposure ages that match the peak of LL chondrites, a mode in Fa contents that falls within the LL range, and low bulk metal contents (Rubin et al., 1996). The meteorite is a moderately weathered find from a grain field in Kansas, USA (Rubin et al., 1996), raising the possibility that terrestrial weathering shifted the oxygen isotope composition of Richfield to slightly outside the LL field. The various aliquots of the meteorite analyzed for oxygen isotopes spread mainly in $\Delta^{17}O$ (Fig. 7d), which could indicate that $\Delta^{17}O$ values were variably lowered by weathering. If so, this would indicate that even moderate weathering in an agricultural (and irrigated) area from a steppe-like climate can affect oxygen isotope compositions. We cannot rule out a weathering effect for inclusion Rfd-I1 in Richfield, but see no reason to believe that the much lower $\Delta^{17}O$ value for it compared to the host (Fig. 7d) is the result of much more extensive weathering. This low $\Delta^{17}O$ value for Rfd-I1 is similar to other inclusions of the same chemical type (*Vfr*) from different hosts (Fig. 7d), which is best explained by this composition representing an extraterrestrial value.

For other meteorites with discrepant oxygen values, including Lut 005, MET 96515, and QUE 97008, terrestrial weathering in differing climates could have been important (Sec. 3.3). Hot desert meteorite Lut 005 (classified LL3.7/3.8) is strongly enriched (by ≥1.5‰) in $\delta^{18}O$ (Fig. 7b), as one might expect for hot desert weathering. In contrast, compared to other L chondrites, Antarctica-recovered MET 96515 (classified L3.5) and QUE 97008 (classified L3.05) are possibly low in $\Delta^{17}O$ (up to 0.5‰), and either much lower in $\delta^{18}O$ (by ~1-2‰, MET 96515) or possibly lower in $\delta^{18}O$ (up to 1‰, QUE 97008) (Fig. 7d). The data are consistent with terrestrial weathering having affected the oxygen isotope compositions of Lut 005, MET 96515, and QUE 97008.

For the inclusions in these meteorites, the evidence suggests a limited role for weathering. The oxygen isotopic compositions of the QUE-I1, QUE-I3, and QUE-I4 inclusions in host QUE 97008 are unlikely to have been strongly affected by terrestrial weathering, given both the tight clustering of inclusion compositions in different meteorite fragments, and the high $\delta^{18}O$ values of these inclusions, which would be in an opposite sense to that expected for cold-weathering effects as invoked to explain the host composition (Fig. 7d). Similarly, the oxygen isotope compositions of MET-I3 in MET 96515 and Lut-I1 in Lut 005 (Fig. 7d) do not follow the same pattern as their hosts, if all were similar to L or LL chondrites originally: weathering-related fractionations invoked for the hosts involve small shifts in $\Delta^{17}O$ values and larger changes in $\delta^{18}O$, opposite to what would be required for the inclusions. Terrestrial weathering might be invoked to explain the heterogeneous oxygen isotope compositions of different MET-I1 aliquots, with two analyses plotting close to the TF line (Fig. 7d). However, this would require weathering effects involving large shifts in $\Delta^{17}O$ and increases in $\delta^{18}O$, opposite to the cold-weathering effects invoked for other Antarctic meteorites, and unlike that observed for the host,

which has a normal L-like oxygen isotope composition and no evidence for any weathering-related fractionation, and unlike MET-I2 recovered from a different piece of the same meteorite, which has much lower $\delta^{18}O$ than MET-I1 (Fig. 7c, 7d).

We conclude that there is little evidence for the oxygen isotope compositions of inclusions having been significantly affected by weathering, even in cases where this might not be true for the host chondrites.

Table A1. Texture and phase compositions of inclusions.

Inclusion	Texture and phase compositions*
869-I1	Contains normally & reversely zoned ol (overall $Fa_{16.4 \pm 6.1}$, ~100 µm across) & zoned low-Ca px ($Wo_{2.3 \pm 1.2}$ $Fs_{23.7 \pm 3.3}$) set in feldspathic glass ($Ab_{25.9 \pm 2.7}$ $Or_{19.6 \pm 2.5}$, 2.7±0.5 at% Mg, 4.3±0.4 at% Fe). Crystals broken (zoning interrupted), inclusion has broken edge in places & partially engulfs (intrudes) host in other places. Adjacent to shock-blackened area.
4686-I1	Ol phenocrysts (~100-150 µm across), normally zoned (cores $Fa_{11.7 \pm 1.9}$, rims $Fa_{18.0 \pm 1.7}$), set in feldspathic glass ($Ab_{70.3 \pm 5.9}$ $Or_{6.1 \pm 1.7}$, 0.37±-0.14 at% Mg, 1.7±0.3 at% Fe). Meso contains tabular or skeletal px grains zoned from low-Ca px ($Wo_{3.8 \pm 1.1}$ $Fs_{19.6 \pm 1.3}$) to pig ($Wo_{8.4 \pm 3.8}$ $Fs_{20.9 \pm 1.1}$), with px often forming overgrowths on ol phenocrysts. Inclusion has sharp edge, partly marked by a fracture, with host.
4859-I4	Rounded inclusion, marked by shock veins, with ol phenocrysts (~500 µm across) including some ol donuts, with intervening low-Ca px, diop, plag, ol. Highly uniform ol ($Fa_{28.4 \pm 0.1}$), low-Ca px ($Wo_{1.7 \pm 0.3}$ $Fs_{19.2 \pm 0.3}$), diop ($Wo_{41.7 \pm 0.3}$ $Fs_{7.5 \pm 0.2}$), somewhat more variable plag ($Ab_{81.6 \pm 1.5}$ $Or_{3.7 \pm 0.7}$). Edge marked by low-Ca px rim inside of ol + plag band & shock vein.
4859-I18	Ol ($Fa_{29.2 \pm 0.3}$) phenocrysts (~100 µm across) set in groundmass of low-Ca px ($Wo_{1.7 \pm 0.3}$ $Fs_{24.1 \pm 0.5}$), diop ($Wo_{46.4 \pm 2.0}$ $Fs_{8.1 \pm 0.6}$) & plag ($Ab_{80.5 \pm 8.5}$ $Or_{5.5 \pm 1.2}$). Rim of ol occurs inside ol + plag band at inclusion edge. Contains rounded metal-troilite nodule.
7869-I1	Drop-formed, met-rich inclusion, interior dominated by zoned granular ol grains (<100 µm across) (cores $Fa_{14.7 \pm 1.5}$, rims $Fa_{23.0 \pm 2.8}$) set in meso containing plag ($Ab_{28.9 \pm 3.5}$ $Or_{0.6 \pm 0.2}$) & diop ($Wo_{50.6 \pm 0.7}$ $Fs_{1.0 \pm 0.3}$). Inclusion has concentric interior Al-sp band, rim with low-Ca px + phos.
7869-I2	Contains phenocrysts (~300 µm across) of normally zoned ol ($Fa_{23.5 \pm 3.3}$) & low-Ca px ($Wo_{1.2 \pm 0.6}$ $Fs_{15.9 \pm 2.0}$) with interstitial plag ($Ab_{48.5 \pm 1.8}$ $Or_{0.3 \pm 0.1}$) & aug ($Wo_{30.2 \pm 2.1}$ $Fs_{16.3 \pm 1.0}$). Irregular, brecciated inclusion edge.
7870-I1	Drop-formed object with concentric skeletal ol bars ($Fa_{25.1 \pm 0.4}$) (grains ~500 x 20 µm across) & interstitial low-Ca px ($Wo_{1.9 \pm 0.6}$ $Fs_{21.5 \pm 0.6}$), plag ($Ab_{82.9 \pm 0.7}$ $Or_{7.7 \pm 1.0}$), diop ($Wo_{44.3 \pm 2.0}$ $Fs_{8.1 \pm 0.6}$), Cl-apat.
7871-I1	Subrounded, somewhat square, inclusion with interior composed of locally aligned ol ($Fa_{25.6 \pm 0.3}$) grains (~30 µm wide), with interstitial diop ($Wo_{46.1 \pm 1.3}$ $Fs_{8.0 \pm 0.5}$), plag ($Ab_{78.8 \pm 3.9}$ $Or_{6.1 \pm 0.9}$), merr, Cl-apat, fine-grained ol; grades into granular ol rim. Cross-cut by calcite veins.
7872-I1	Inclusion has core with BO texture that grades into granular ol rim. Core composed of parallel ol ($Fa_{24.4 \pm 0.3}$) grains (~30 x 180 µm across) of same crystal orientation, with interstitial aug ($Wo_{38.7 \pm 6.6}$ $Fs_{11.0 \pm 2.1}$) & two feldspar types ($Ab_{13.9 \pm 4.2}$ $Or_{0.3 \pm 0.2}$, lesser $Ab_{86.6 \pm 1.8}$ $Or_{6.0 \pm 1.5}$). Grades into granular ol rim. Adjacent to shock-blackened area.
7873-I1	Inclusion has equant to elongate grains of ol (~150 µm wide, up to ~1 mm long) with normally zoned ol ($Fa_{12.4 \pm 3.8}$) set in glassy meso ($Ab_{44.8 \pm 2.2}$ $Or_{2.7 \pm 1.2}$, 4.5±0.6 at% Mg, 4.2±0.3 at% Fe) with crystallites. Ol grains brecciated (zoning interrupted), concentrated on one side of inclusion. Some shock veins inside inclusion. Adjacent to met-troi nodule in melt breccia host.
8141-I1	Sub-rounded, partly brecciated inclusion with ~750 µm-wide attached piece, partial troi + low-Ca px rim integrated with inclusion. Contains ol ($Fa_{24.5 \pm 0.4}$) grains (~250 µm across), set in groundmass of low-Ca px ($Wo_{1.4 \pm 0.2}$ $Fs_{20.6 \pm 0.8}$), diop ($Wo_{45.5 \pm 0.6}$ $Fs_{7.5 \pm 0.3}$) & plag ($Ab_{81.6 \pm 5.1}$ $Or_{5.7 \pm 1.2}$).
8231-I1	Inclusion in multiple pieces within melt breccia host. Poik texture with ol set in coarse (~400 µm across) low-Ca px ($Wo_{1.6 \pm 0.2}$ $Fs_{17.6 \pm 0.4}$),

	interstitial areas between coarse low-Ca px contains ol ($Fa_{21.0 \pm 0.2}$), aug ($Wo_{38.1 \pm 1.7}$ $Fs_{11.2 \pm 1.3}$), plag ($Ab_{82.7 \pm 1.6}$ $Or_{13.6 \pm 1.9}$), troi & phos. Met-troi nodule near edge. Internally brecciated, with chondritic portion deep inside inclusion.
8232-I1	Rounded, oval-shaped inclusion has ol ($Fa_{29.3 \pm 0.2}$) grains (~100 µm across) set in plag-rich (maskelynite) ($Ab_{81.1 \pm 1.5}$ $Or_{5.1 \pm 0.7}$) meso, with low-Ca px + ol rim. Diop ($Wo_{45.1 \pm 0.4}$ $Fs_{9.0 \pm 0.4}$) only in meso patches within core; low-Ca px ($Wo_{2.7 \pm 0.6}$ $Fs_{17.6 \pm 0.4}$) only near rim. At one edge, have outer plag band & inner px-rich band, with plag in band extending into host. Inclusion texturally integrated with host.
8645-I1	Contains ol ($Fa_{25.5 \pm 0.7}$) grains (~300 µm across) set in meso with plag ($Ab_{83.2 \pm 2.7}$ $Or_{6.2 \pm 2.8}$), diop ($Wo_{44.9 \pm 2.6}$ $Fs_{7.8 \pm 3.4}$), & some low-Ca px ($Wo_{1.6 \pm 1.0}$ $Fs_{21.4 \pm 1.8}$). Met & troi occur in patches. Plag at rim, grades into host.
Arm-I1	Oval-shaped inclusion with ol ($Fa_{24.6 \pm 1.0}$), both as isolated grains (~500 µm across), as ol donuts, and as patches of BO-like domains (~125 µm across), set in meso rich in diop ($Wo_{44.8 \pm 2.2}$ $Fs_{7.1 \pm 1.8}$), with less plag ($Ab_{79.4 \pm 3.9}$ $Or_{6.6 \pm 2.6}$) & low-Ca px ($Wo_{3.3 \pm 1.8}$ $Fs_{19.3 \pm 2.1}$); more low-Ca px at margin. Has smaller (2 x 1 mm) attached piece.
Arm-I2	Oval-shaped inclusion with grains (~250 µm across) of ol ($Fa_{24.1 \pm 1.1}$) set in meso with diop ($Wo_{43.4 \pm 1.8}$ $Fs_{8.9 \pm 2.8}$), low-Ca px ($Wo_{1.6 \pm 0.3}$ $Fs_{22.1 \pm 0.9}$), plag ($Ab_{79.3 \pm 3.8}$ $Or_{6.3 \pm 1.6}$) and Cr-sp; more low-Ca px at inclusion edge. Has smaller (2 x 1 mm) attached piece.
Cyn-I1	Phenocrysts (~100 µm across) of zoned clinoenstatite ($Wo_{0.7 \pm 0.2}$ $Fs_{16.9 \pm 7.7}$) & equilibrated ol ($Fa_{26.9 \pm 0.3}$) set in groundmass of plag ($Ab_{32.8 \pm 1.9}$ $Or_{0.4 \pm 0.1}$) and aug ($Wo_{38.7 \pm 2.4}$ $Fs_{8.8 \pm 0.8}$). Inclusion is a fragment.
Dim-I1	Contains tabular, elongate, equant, or glomerocrystic ol grains (~200 µm across) set in a glassy meso ($Ab_{19.0 \pm 5.9}$ $Or_{15.7 \pm 6.5}$, 4.5±0.8 at% Mg, 2.6±0.7 at% Fe) with crystallites. Have both normally zoned ol with magnesian cores (Fa<7, $Fa_{5.3 \pm 1.4}$) & narrow ferroan rims; and reversely zoned ol with ferroan cores (Fa>7, $Fa_{18.2 \pm 4.4}$) & narrow magnesian rims. Dusty metal inclusions often occur in grain cores (ferroan and magnesian). Grain zonation sometimes interrupted (grains brecciated). Inclusion contains sub-mm domains with different textures (mPO, GO, BO) as well as a larger (~2.7 x 1.9 mm) type 3 chondritic clast deep in the interior. The inclusion is a fragment although olivine grains decorate one margin.
Etr-I1	Elongate inclusion with curved ol rim on one edge though elsewhere inclusion is brecciated (inclusion may be droplet fragment). Texturally integrated with host. Contains coarse (~2 mm long) elongate-skeletal ol ($Fa_{25.2 \pm 0.6}$) grains, with finer low-Ca px ($Wo_{1.5 \pm 0.2}$ $Fs_{21.5 \pm 0.2}$) phenocrysts in places rimmed by diop ($Wo_{44.3 \pm 0.5}$ $Fs_{8.4 \pm 0.8}$), set in an abundant meso with feldspar ($Ab_{83.1 \pm 2.7}$ $Or_{1.0 \pm 0.1}$) and feldspathic glass ($Ab_{72.8 \pm 8.5}$ $Or_{24.4 \pm 9.0}$, 0.03 at% Mg, 0.09 at% Fe), Cr-sp, low-Ca px, diop, ol. Contains mm-sized Cl-apat & merr, also phos veinlets in meso. Diop notably underabundant close to phos. Has melt pockets that grade into feldspar.
Glk-I1	Inclusion has rounded overall form but is bounded by shock veins that partly extend into the inclusion. Contains both normally & reversely zoned ol (magnesian: $Fa_{9.4 \pm 0.8}$, ferroan $Fa_{18.1 \pm 2.2}$, overall $Fa_{11.5 \pm 3.8}$) (~100 µm grains) set in glassy meso. Two types of meso present, dominantly feldspathic ($Ab_{35.9 \pm 8.4}$ $Or_{3.9 \pm 1.2}$, 5.4±1.0 at% Mg, 5.0±0.4 at% Fe) and lesser mafic, pyroxene-normative ($Ab_{33.9 \pm 3.9}$ $Or_{1.3 \pm 1.3}$, 14.5 at% Mg, 5.0±0.3 at% Fe); in places ol ± feldspathic meso form clasts in mafic meso. Has coarse round met-troi nodules, troi veinlets that cross-cut all phases but which are often concentrated in ol.
Jgo-I1	Contains ol ($Fa_{25.5 \pm 0.7}$) grains of different habits, set in distinctive meso composed largely of plag ($Ab_{83.1 \pm 1.9}$ $Or_{6.2 \pm 1.6}$) & Cr-sp. Shows composite textures: portions have BO-like texture dominated by locally parallel, elongate ol grains (~420 x 130 µm across), elsewhere contains equant ol grains including coarse (up to 4 mm across) grain. Meso contains lesser low-Ca px ($Wo_{1.4 \pm 0.8}$ $Fs_{21.6 \pm 1.8}$), diop ($Wo_{44.5 \pm 2.0}$ $Fs_{8.1 \pm 1.5}$), Cl-apat, met. Inclusion edge is plag-rich and texturally integrated with host.

Khr-I1	Oblong & subrounded inclusion bounded by shock vein. Contains ol ($Fa_{19.9 \pm 2.5}$) phenocrysts (~150 µm across) including ol donuts intergrown with interstitial pig ($Wo_{13.0 \pm 3.8}$ $Fs_{21.0 \pm 1.5}$) & plag ($Ab_{19.3 \pm 2.5}$ $Or_{0.8 \pm 0.6}$). Accessory Cr-sp.
KrC-I1	Drop-formed cryptocrystalline inclusion (grains ~20 µm across), has curved but abraded rim, locally aligned elongate-skeletal ol ($Fa_{22.0 \pm 0.5}$) intergrown with low-Ca px ($Wo_{4.4 \pm 1.7}$ $Fs_{18.1 \pm 0.5}$), diop ($Wo_{45.6 \pm 2.5}$ $Fs_{6.4 \pm 0.9}$) & finer interstitial plag ($Ab_{64.6 \pm 8.3}$ $Or_{1.1 \pm 0.7}$). Similar finer-grained material is nearby which coats a fragmented chondrule.
Lut-I1	Drop-formed object broken on some margins. Core is dominated by skeletal grains (~100 x 20 µm across) of locally aligned olivine & low-Ca px, which grades into a granular rim (up to ~0.5 mm thick) dominated by equant ol. Between ol ($Fa_{19.9 \pm 6.3}$) & low-Ca px ($Wo_{3.1 \pm 1.9}$ $Fs_{10.9 \pm 3.2}$) grains, have intervening patches of plag ($Ab_{19.1 \pm 6.2}$ $Or_{0.4 \pm 1.1}$) & high-Ca px ($Wo_{24.1 \pm 11.0}$ $Fs_{10.4 \pm 3.0}$, includes both pig and aug). Some low-Ca px in interior is clinoenstatite, and some plag is replaced by feldspathoid. Core is more magnesian than edge, except for 3 bands of ferroan ol intergrown with phos that cross-cut the inclusion.
McK-I1	Homogenous ol ($Fa_{25.8 \pm 0.2}$) grains (~100 µm across) with interstitial pig of two types ($Wo_{13.1 \pm 3.3}$ $Fs_{20.9 \pm 2.3}$, $Wo_{27.7 \pm 4.3}$ $Fs_{15.1 \pm 1.9}$), plag ($Ab_{21.8 \pm 2.8}$ $Or_{0.4 \pm 0.2}$) & glass/maskelynite ($Ab_{87.5 \pm 1.8}$ $Or_{4.8 \pm 0.8}$). Possible ol donut fragments. Shows abundant troi veining mainly limited to ol grains (as in host), interstitial phases mostly not veined although lower-Ca pig sometimes veined.
McK-I2	Ol ($Fa_{24.5 \pm 0.6}$) grains (~100 µm across) set in mesostasis containing pig ($Wo_{18.9 \pm 3.0}$ $Fs_{16.6 \pm 1.1}$), plag ($Ab_{14.7 \pm 1.0}$ $Or_{0.5 \pm 0.4}$), and sodic glass (maskelynite). Abundant troi veining limited mainly to ol. Low-Ca px ($Wo_{2.6 \pm 0.6}$ $Fs_{18.1 \pm 2.2}$) in rim.
MET-I1	Low-Ca px grains (~500 µm across) that poikilitically enclose ol are set in a meso with plag ($Ab_{17.0 \pm 5.2}$ $Or_{2.5 \pm 0.9}$) & pig ($Wo_{16.1 \pm 6.3}$ $Fs_{27.5 \pm 5.9}$). Low-Ca px grains include clinoenstatite cores ($Wo_{0.6 \pm 0.6}$ $Fs_{11.5 \pm 1.4}$) & thick ferroan opx overgrowths ($Wo_{3.5 \pm 1.6}$ $Fs_{17.0 \pm 2.0}$) which itself are overgrown by aug ($Wo_{33.8 \pm 2.7}$ $Fs_{14.5 \pm 2.8}$). Ol is normally zoned ($Fa_{16.9 \pm 3.3}$) & appears partly resorbed by low-Ca px. Inclusion has rounded overall form but is a clast, surrounded by a fine grained rim.
MET-I2	Normally zoned ol (cores $Fa_{8.6 \pm 0.9}$, rims $Fa_{12.8 \pm 2.3}$, overall $Fa_{11.6 \pm 2.8}$) phenocrysts (~200 µm across) are set in a meso with pig ($Wo_{21.8 \pm 7.8}$ $Fs_{13.6 \pm 3.1}$) & feldspathic glass ($Ab_{56.3 \pm 9.8}$ $Or_{34.1 \pm 9.4}$, 1.5±1.7at% Mg, 1.3±0.5 at% Fe). Inclusion is a clast.
MET-I3	Normally zoned ol ($Fa_{22.6 \pm 2.3}$) is poikilitically enclosed by low-Ca px ($Wo_{2.1 \pm 1.0}$ $Fs_{17.9 \pm 1.7}$) & set in a relatively sparse meso with plag ($Ab_{19.0 \pm 3.4}$ $Or_{0.6 \pm 1.1}$) & pig ($Wo_{21.6 \pm 7.7}$ $Fs_{23.7 \pm 6.7}$). Pig locally overgrows low-Ca px; low-Ca px is mainly opx but is clinoenstatite (striated) in places. Cr-sp, met, troi are accessory phases. Inclusion is a clast.
Obl-I1	Fragment composed chiefly of coarse ol (up to 1 mm, $Fa_{28.8 \pm 0.6}$) with interstitial plag ($Ab_{82.3 \pm 2.1}$ $Or_{4.0 \pm 1.1}$), low-Ca px ($Wo_{1.2 \pm 0.1}$ $Fs_{23.6 \pm 0.4}$) & diop ($Wo_{45.5 \pm 0.3}$ $Fs_{8.2 \pm 0.2}$). Mode probably not representative owing to coarse size of ol.
Obl-I2	Drop-formed object with classic barred ol-px texture, including ol shell. Elongate and parallel grains (~70 x 500 µm across) of ol ($Fa_{28.0 \pm 0.6}$) & low-Ca px ($Wo_{1.8 \pm 0.3}$ $Fs_{23.4 \pm 0.7}$) are associated with meso patches containing diop ($Wo_{44.1 \pm 1.6}$ $Fs_{8.5 \pm 1.5}$), plag ($Ab_{83.2 \pm 2.1}$ $Or_{5.0 \pm 2.0}$), ol & accessory phos and chr. Nearby troi-rich nodule.
Par-I1	Contains normally zoned ol ($Fa_{21.5 \pm 2.1}$) phenocrysts (~500 µm across), with interstitial pig ($Wo_{12.3 \pm 5.3}$ $Fs_{18.2 \pm 2.3}$) zoned to aug ($Wo_{35.8 \pm 2.5}$ $Fs_{11.3 \pm 0.9}$), & plag ($Ab_{13.5 \pm 2.2}$ $Or_{0.2 \pm 0.1}$). One ol donut. Low-Ca px at rim only.
Par-I2	Phenocrysts (~500 µm across) of low-Ca px ($Wo_{0.8 \pm 0.5}$ $Fs_{17.6 \pm 3.7}$) with pig/aug ($Wo_{27.1 \pm 3.6}$ $Fs_{34.5 \pm 5.1}$) overgrowths, often partly enclosing olivine ($Fa_{24.6 \pm 3.1}$) grains with weak normal zoning, set in a glassy meso ($Ab_{69.6 \pm 6.0}$ $Or_{1.8 \pm 0.4}$, 1.9±0.5 at% Mg, 2.0±0.5 at% Fe). Most low-Ca px has partly reverse zoning; clinoenstatite occurs in the cores of some grains. Inclusion has round outline and appears drop-formed in part

	based on radial and concentric arrangement of low-Ca px.
Par-I3	Cryptocrystalline (grains <10 µm across), composed of platy crystals of chemically uniform low-Ca px ($Wo_{3.8 \pm 0.6}$ $Fs_{25.8 \pm 0.2}$) & pockets of pig ($Wo_{12.7 \pm 0.5}$ $Fs_{23.2 \pm 0.2}$). Low-Ca px intergrades with platy ol ($Fa_{29.5 \pm 0.3}$). Little feldspar.
PVM-I1	Ol ($Fa_{25.5 \pm 0.4}$) phenocrysts (~200 µm across), including ol donuts, set in meso rich in feld/maskelynite ($Ab_{82.9 \pm 1.9}$ $Or_{5.9 \pm 2.1}$) with subequal diop ($Wo_{45.1 \pm 0.9}$ $Fs_{7.6 \pm 0.3}$), chr, phos and low-Ca px. Low-Ca px ($Wo_{1.9 \pm 1.0}$ $Fs_{20.9 \pm 1.3}$) more abundant towards edge. Rim has plag/maskelynite+sp band in places, which texturally integrades with host. Nearby met-sulf nodule.
QUE-I1	Grains of low-Ca px (~130 x 460 µm across) and ol (~330 µm across) are set in a glassy meso rich in plag ($Ab_{21.1 \pm 9.5}$ $Or_{2.9 \pm 1.0}$) & pig ($Wo_{19.3 \pm 5.3}$ $Fs_{44.1 \pm 7.7}$). Low-Ca px phenocrysts ($Wo_{2.0 \pm 0.5}$ $Fs_{19.4 \pm 1.4}$), mostly opx but also striated (with clinoenstatite), have overgrowths of pig/aug ($Wo_{28.1 \pm 2.8}$ $Fs_{25.0 \pm 1.4}$) & enclose irregularly-shaped ol grains that are normally zoned (cores: $Fa_{13.1 \pm 1.0}$, rims: $Fa_{19.8 \pm 3.2}$). Inclusion is clearly a clast.
QUE-I3	Grains of ol (~0.36 x 1 mm) and low-Ca px (~100 x 400 µm across) are set in a meso with feldspathic glass ($Ab_{87.0 \pm 4.5}$ $Or_{2.5 \pm 1.0}$, 0.33±0.09 at% Mg, 1.2±0.30 at% Fe), pig ($Wo_{16.9 \pm 6.1}$ $Fs_{46.2 \pm 4.2}$) & plag ($Ab_{19.8 \pm 7.3}$ $Or_{0.6 \pm 1.4}$). Ol is normally zoned (cores: $Fa_{13.7 \pm 2.2}$, rims: $Fa_{20.3 \pm 2.0}$) & either elongate, glomerocrystic, or irregular in shape. Elongate low-Ca px ($Wo_{2.2 \pm 0.6}$ $Fs_{19.3 \pm 1.4}$) phenocrysts, mainly opx but also striated, locally enclose ol & have overgrowths of aug ($Wo_{30.4 \pm 3.0}$ $Fs_{23.2 \pm 4.6}$). The inclusion is a clast, and pieces appear to be brecciated throughout host.
QUE-I4	Inclusion is brecciated as a whole & internally, with changes in texture across apparent microfaults that do not extend past the inclusion edge. Most of the inclusion contains coarse irregular to tabular ol grains (~0.4-3 mm across) & finer-grained tabular low-Ca px grains (~150 x 370 µm across) with Ca-px rims, set in a meso with pig ($Wo_{20.0 \pm 9.2}$ $Fs_{29.9 \pm 13.2}$) & a mixture of plag & feldspathic glass (overall composition $Ab_{35.6 \pm 19.2}$ $Or_{1.1 \pm 2.2}$). One part of the inclusion almost completely lacks ol and contains finer phenocrysts of low-Ca px (~85 µm across) with rims of Ca-px set in meso. Ol grains are normally zoned (cores: $Fa_{13.1 \pm 3.2}$, rims: $Fa_{26.1 \pm 7.0}$). Low-Ca px ($Wo_{2.2 \pm 1.2}$ $Fs_{19.6 \pm 3.3}$) is striated (partly clinoenstatite) and overgrown by aug ($Wo_{34.5 \pm 4.4}$ $Fs_{18.9 \pm 3.5}$). Al-spinel is accessory phase. Mode may not be representative owing to coarse ol grain size.
Rfd-I1	Drop-formed, with zoned fine-grained interior (core: less ol, more low-Ca px; mantle: more olivine, less low-Ca px) & granular rim rich in low-Ca px. Fine-grained interior has aligned ol ($Fa_{18.3 \pm 3.2}$) crystals (~100 x 20 µm across) intergrown with low-Ca px ($Wo_{2.1 \pm 0.5}$ $Fs_{11.1 \pm 1.1}$), aug ($Wo_{33.7 \pm 5.6}$ $Fs_{10.4 \pm 1.3}$), and interstitial feldspathic material.
Rgl-I1	Zoned ol ($Fa_{22.0 \pm 7.2}$) phenocrysts (~100 µm across) set in glass ($Ab_{52.1 \pm 4.4}$ $Or_{6.1 \pm 5.4}$, 2.9±0.3 at% Mg, 1.7±0.3 at% Fe). Internally brecciated.
Tdk-I1	Oval-shaped droplet, with radiating grains (~100 x 10 µm across) of low-Ca px ($Wo_{4.1 \pm 1.0}$ $Fs_{15.7 \pm 1.1}$) and ol ($Fa_{18.4 \pm 0.4}$), richer in px than ol, set amidst diop ($Wo_{48.8 \pm 0.6}$ $Fs_{5.6 \pm 0.6}$) and lesser plag of two types ($Ab_{81.2 \pm 2.0}$ $Or_{8.7 \pm 3.8}$, $Ab_{46.8 \pm 12.3}$, $Or_{1.3 \pm 0.5}$). Inclusion has px-rich rim in places.
Tdk-I2	Equant zoned low-Ca px ($Wo_{2.2 \pm 1.2}$ $Fs_{16.3 \pm 1.2}$) grains (~450 µm across) with a few parallel ol ($Fa_{18.6 \pm 0.3}$) bars (grains ~110 µm wide) set in a meso with plag ($Ab_{17.0 \pm 2.3}$ $Or_{0.1 \pm 0.1}$), aug ($Wo_{37.1 \pm 5.9}$ $Fs_{8.7 \pm 2.3}$), and low-Ca px. Inclusion is a clast with texturally blurred boundary.

* Mean phase compositions (±1σ values given in parentheses) as determined by combination of SEM and EMPA methods, and representative grain sizes & inclusion edge character as determined by OM and SEM methods. Abbreviations: ol = olivine, px = pyroxene, meso = mesostasis, opx = orthopyroxene, diop = diopside, pig = pigeonite, aug = augite, plag = plagioclase, phos = phosphate, apat = apatite, merr = merrillite, met =

metal, troi = troilite, sp= spinel, mainly chromite. Endmember compositions (mole %): Fa = 100Fe/(Fe+Mg), Fs = 100Fe/(Mg+Fe+Ca), Wo = 100Ca/(Mg+Fe+Ca), Ab=100Na/(Na+K+Ca), Or = 100K/(Na+K+Ca).

Table A2. Modal composition of inclusions determined by SEM mapping technique.

Inclusion	Area (%)*									
	Olivine	Low-Ca pyroxene [1]	High-Ca pyroxene[2]	Plagio-clase	Meso-stasis / glass	Phos-phate [3]	Chromite	Troilite	FeNi metal [4]	Other [5]
869-I1	58.7 (3.5)	10.5 (1.8)	0	0	30.2 (3.5)	0	0.1 (0.06)	0.4 (0.1)	0.1 (0.07)	0
4686-I1	64.9 (0.3)	12.0 (0.1)	3.1 (0.01)	0	18.9 (0.1)	0	0.1 (0.00)	0.8 (0.01)	0.2 (0.00)	0
4859-I4	49.0 (1.2)	23.2 (1.6)	3.1 (0.1)	23.8 (1.5)	0	0.3 (0.04)	0.1 (0.05)	0.3 (0.01)	0.2 (0.01)	trace ilm
4859-I18	49.9 (2.9)	23.2 (0.9)	6.9 (1.9)	16.8 (2.4)	0	0.1 (0.01)	0.4 (0.36)	2.4 (0.6)	0.2 (0.05)	0.3 (0.01) ilm
7869-I1	60.9 (5.0)	8.0 (2.2)	4.6 (0.2)	10.3 (0.2)	0	2.3 (0.06)	0.2 (0.02)	5.4 (0.2)	6.8 (1.8)	1.5 (0.1) sp
7869-I2	36.4 (1.3)	34.6 (0.5)	11.3 (2.3)	15.6 (1.0)	0	0	0.4 (0.01)	0.7 (0.03)	0.9 (0.01)	0
7870-I1	50.1 (3.0)	21.6 (3.2)	5.2 (2.0)	22.3 (1.7)	0	0.7 (0.11)	0.1 (0.02)	0	0.1 (0.02)	trace ilm
7871-I1	74.7 (1.6)	0	4.3 (0.9)	16.8 (2.5)	0	1.1 (0.1)	0.6 (0.01)	0.2 (0.01)	0.1 (0.01)	2.3 (0.7) cc
7872-I1	69.2 (2.8)	0	10.2 (0.7)	18.8 (2.8)	0	0.4 (0.06)	0.6 (0.02)	0.3 (0.2)	0.3 (0.08)	0.2 (0.005) ilm
7873-I1	58.7 (7.6)	0	0	0	40.7 (1.0)	0	0.1 (0.01)	0.4 (0.1)	0.1 (0.1)	0
8141-I1	55.3 (0.3)	13.8 (2.1)	12.2 (1.0)	15.4 (1.4)	0	0	0.4 (0.1)	2.3 (0.2)	0.6 (0.2)	0
8231-I1	42.9 (3.7)	27.8 (3.2)	9.5 (2.5)	12.8 (2.2)	0	1.1 (0.2)	0.7 (0.5)	4.3 (2.7)	0.8 (0.1)	0
8232-I1	59.3 (2.3)	20.7 (2.9)	5.4 (2.4)	12.8 (1.0)	0	0.2 (0.01)	0.5 (0.1)	0.3 (0.04)	0.8 (0.02)	0
8645-I1	77.9	2.5	7.9	9.9	0	0.2	0.6	0.5	0.7	0

	(1.1)	(0.2)	(1.2)	(0.4)		(0.01)	(0.01)	(0.01)	(0.01)	
Arm-I1	70.9 (3.7)	3.0 (0.1)	9.7 (4.0)	15.3 (0.1)	0	0.6 (0.03)	0.2 (0.01)	0	0.2 (0.01)	0
Arm-I2	70.7 (0.7)	6.8 (1.0)	4.5 (0.05)	16.6 (0.2)	0	0.4 (0.00)	0.7 (0.03)	0	0.4 (0.02)	0
Cyn-I1	6.7 (0.5)	69.2 (6.6)	6.9 (0.3)	15.2 (0.4)	0	0	0.1 (0.01)	1.9 (0.01)	0	trace ilm
Dim-I1	64.8 (2.1)	0	0	0	32.8 (2.0)	0	0	1.5 (0.3)	0.8 (0.08)	0
Etr-I1	36.5 (3.1)	20.4 (1.2)	4.0 (0.55)	32.2 (1.7)	0	6.2 (0.2)	0.4 (0.12)	0.1 (0.01)	0.1 (0.01)	0
Glk-I1	39.2 (0.2)	0	0	0	58.1 (2.9)	0	0.1 (0.01)	1.8 (0.01)	0.8 (0.05)	0
Jgo-I1	68.5 (0.6)	0.9 (0.01)	1.9 (0.02)	21.3 (0.5)	0	0.8 (0.01)	1.4 (0.01)	1.0 (0.01)	4.2 (0.04)	0
Khr-I1	71.0 (0.8)	15.9 (0.9)	0	11.6 (0.7)	0	0	0.2 (0.01)	0.9 (0.1)	0.5 (0.06)	0
KrC-I1	49.4 (2.1)	27.5 (0.2)	8.6 (1.4)	13.5 (2.1)	0	0	0.6 (0.1)	0.2 (0.03)	0.1 (0.01)	0.2 (0.03) ilm
Lut-I1	29.6 (2.9)	49.8 (1.8)	9.3 (0.6)	4.8 (2.6)	0	0.1 (0.01)	trace	0	0.7 (0.01)	5.6 (1.7) sod, 0.1 (0.05) ilm
McK-I1	69.4 (0.9)	14.5 (0.4)	2.2 (0.4)	12.6 (0.9)	0	0.1 (0.05)	0.3 (0.1)	0.6 (0.2)	0.2 (0.01)	0
McK-I2	42.5 (0.3)	40.1 (1.6)	3.5 (1.6)	10.5 (0.9)	2.3 (0.1)	0.1 (0.01)	0.4 (0.2)	0.5 (0.3)	0.1 (0.01)	0
MET-I1	30.7 (0.05)	37.4 (0.4)	25.9 (0.5)	6.1 (0.01)	0	0	0	0	0	0
MET-I2	54.0 (3.1)	0	9.4 (0.03)	0	34.4 (0.2)	0	0	1.2 (0.02)	1.0 (0.01)	0
MET-I3	42.6 (0.9)	36.9 (1.5)	12.4 (0.2)	6.3 (0.3)	0	0	0	1.1 (0.02)	0.2 (0.00)	0.4 (0.1) sp
Obl-I1 [6]	90.5 (1.1)	1.5 (0.8)	0.8 (0.1)	6.9 (0.8)	0	0.1 (0.01)	0.1 (0.01)	0	0	0

Obl-I2	50.5 (0.2)	32.5 (0.3)	5.0 (0.45)	10.4 (0.8)	0	0.5 (0.00)	0.4 (0.00)	0.5 (0.00)	0.3 (0.00)	0
Par-I1	60.0 (2.9)	24.5 (1.1)	4.9 (0.2)	9.8 (1.6)	0	0	0.1 (0.01)	0.1 (0.01)	0.4 (0.01)	0.2 (0.01) ilm
Par-I2	17.3 (0.4)	63.8 (5.1)	8.0 (0.2)	0	10.1 (0.2)	0	0.1 (0.01)	0.5 (0.1)	0.2 (0.03)	0
Par-I3	6.9 (1.3)	72.8 (2.1)	19.6 (2.0)	0	0	0	0.1 (0.03)	0	0.6 (0.49)	0
PVM-I1	71.0 (2.3)	7.5 (1.6)	4.3 (1.4)	15.6 (1.1)	0	0.4 (0.02)	0.5 (0.09)	trace	0.7 (0.11)	0
QUE-I1	21.7 (0.2)	38.7 (1.5)	13.0 (0.2)	17.5 (2.1)	8.9 (0.5)	0	0	0	0.2 (0.00)	0
QUE-I3	38.2 (3.8)	8.3 (0.01)	39.5 (1.7)	8.4 (0.4)	5.5 (0.1)	0	0	0	trace	0.1 (0.00) sp
QUE-I4	50.7 (0.3)	23.7 (0.1)	12.1 (0.4)	13.2 (0.1)	0	0	0	0.2 (0.00)	0.1 (0.00)	0.1 (0.00) sp
Rfd-I1	42.2 (0.6)	31.9 (0.2)	9.0 (2.3)	16.3 (1.5)	0	0	0.1 (0.01)	0.3 (0.07)	0.1 (0.04)	0.1 (0.01) ilm
Rgl-I1	63.2 (8.0)	0	0	0	35.1 (3.0)	0	0.4 (0.07)	0.2 (0.15)	0.9 (0.5)	0.2 (0.07) ilm
Tdk-I1	43.0 (2.1)	49.7 (2.8)	4.1 (0.4)	3.0 (0.4)	0	0	0.1 (0.01)	0.1 (0.02)	trace	0
Tdk-I2	17.7 (0.1)	69.2 (0.7)	4.0 (0.1)	8.9 (0.8)	0	0	0.1 (0.01)	trace	0.1 (0.01)	trace ilm

*Totals originally 100% before rounding. Values in parentheses give ±1σ values.

[1] Includes orthopyroxene or clinoenstatite with Wo ≤ 5. [2] Includes pigeonite, augite, or diopside with Wo > 5. [3] Includes merrillite and apatite. [4] Includes kamacite and taenite. [5] Other phases: ilm = ilmenite, sp = aluminous spinel, cc = calcite, sod = sodalite. [6] Mode unrepresentative owing to coarse olivine grain size.

Table A3. Bulk chemical composition of inclusions determined by modal reconstruction.*

	Wt%														
Inclusion	SiO_2	TiO_2	Al_2O_3	Cr_2O_3	FeO	MnO	MgO	CaO	Na_2O	K_2O	P_2O_5	S	Fe(s)	Fe(m)	Ni
869-I1	46.3 (2.4)	0.12 (0.07)	1.98 (0.25)	0.39 (0.11)	16.8 (1.4)	0.52 (0.21)	29.6 (1.5)	2.32 (0.33)	0.55 (0.09)	0.63 (0.12)	<0.01	0.20 (0.05)	0.37 (0.09)	0.19 (0.15)	0.03 (0.02)
4686-I1[1]	46.1	0.13	2.36	0.78	9.01	0.54	36.6	1.02	1.01	0.11	0.08	0.41	0.8	0.46	0.6

	(0.5)	(0.04)	(0.26)	(0.12)	(0.78)	(0.1)	(0.7)	(0.39)	(0.1)	(0.03)	(0.05)	(0.02)	(0.04)	(0.02)	(0.15)
4859-I4[2]	46.7 (1.3)	0.1 (0.04)	4.48 (0.29)	0.17 (0.06)	16.9 (0.4)	0.35 (0.06)	26.8 (0.7)	1.53 (0.12)	1.86 (0.12)	0.13 (0.03)	0.11 (0.02)	0.15 (0.01)	0.25 (0.01)	0.32 (0.02)	0.17 (0.02)
4859-I18	44.0 (2.0)	0.12 (0.01)	3.00 (0.44)	0.36 (0.11)	18.5 (0.9)	0.39 (0.02)	25.9 (1.1)	2.10 (0.44)	1.23 (0.17)	0.14 (0.03)	0.06 (0.05)	1.31 (0.30)	2.39 (0.55)	0.28 (0.06)	0.19 (0.04)
7869-I1	31.8 (1.7)	0.10 (0.02)	3.56 (0.16)	0.23 (0.02)	11.4 (1.0)	0.21 (0.04)	27.1 (1.6)	2.96 (0.32)	0.29 (0.03)	0.01 (0.00)	0.83 (0.29)	2.66 (0.55)	4.35 (0.90)	12.3 (2.5)	2.26 (0.56)
7869-I2	46.7 (1.3)	0.05 (0.01)	4.22 (0.30)	0.75 (0.09)	13.1 (0.7)	0.37 (0.04)	27.8 (0.8)	3.12 (0.37)	0.70 (0.06)	0.01 (0.00)	<0.01	0.37 (0.01)	0.65 (0.02)	2.09 (0.02)	0.06 (0.01)
7870-I1[3]	47.2 (2.6)	0.17 (0.05)	3.9 (0.3)	0.27 (0.04)	15.8 (0.9)	0.40 (0.04)	27.7 (1.6)	2.08 (0.46)	1.68 (0.13)	0.23 (0.03)	0.29 (0.04)	<0.01	<0.01	0.17 (0.03)	0.05 (0.01)
7871-I1[4]	41.6 (1.6)	0.05 (0.01)	2.90 (0.44)	0.49 (0.02)	19.1 (0.5)	0.39 (0.05)	31.2 (0.7)	1.97 (0.27)	1.22 (0.20)	0.14 (0.03)	0.44 (0.08)	0.08 (0.01)	0.14 (0.01)	0.19 (0.02)	0.02 (0.00)
7872-I1[5]	41.2 (1.8)	0.35 (0.07)	4.76 (0.44)	0.56 (0.05)	16.7 (0.7)	0.39 (0.05)	30.3 (1.2)	3.48 (0.31)	0.86 (0.20)	0.08 (0.03)	0.14 (0.02)	0.17 (0.11)	0.30 (0.18)	0.64 (0.17)	0.09 (0.03)
7873-I1	46.6 (2.4)	0.14 (0.07)	2.52 (0.11)	0.82 (0.18)	15.4 (1.2)	0.49 (0.10)	29.6 (2.6)	2.29 (0.18)	1.04 (0.09)	0.09 (0.04)	<0.01	0.32 (0.06)	0.39 (0.10)	0.23 (0.23)	0.02 (0.02)
8141-I1	43.7 (1.5)	0.08 (0.03)	2.46 (0.26)	0.45 (0.10)	15.7 (0.4)	0.33 (0.12)	28.4 (0.7)	2.93 (0.25)	1.06 (0.14)	0.11 (0.02)	<0.01	1.19 (0.10)	2.13 (0.19)	1.14 (0.15)	0.30 (0.05)
8231-I1[6]	43.4 (2.9)	0.10 (0.04)	2.20 (0.35)	0.93 (0.40)	12.8 (0.9)	0.40 (0.05)	27.8 (1.9)	2.61 (0.46)	1.04 (0.17)	0.23 (0.05)	0.45 (0.09)	2.17 (1.36)	4.01 (2.52)	1.51 (0.21)	0.32 (0.08)
8232-I1[7]	43.0 (2.2)	0.14 (0.03)	2.35 (0.18)	0.54 (0.17)	20.0 (0.8)	0.40 (0.04)	28.3 (1.2)	1.68 (0.50)	0.92 (0.08)	0.09 (0.01)	0.08 (0.00)	0.15 (0.02)	0.27 (0.04)	1.43 (0.05)	0.58 (0.05)
8645-I1	42.3 (0.8)	0.06 (0.01)	1.95 (0.10)	0.50 (0.03)	15.3 (0.4)	0.40 (0.02)	34.3 (0.7)	1.96 (0.25)	0.78 (0.18)	0.09 (0.02)	0.06 (0.01)	0.28 (0.01)	0.48 (0.02)	1.36 (0.08)	0.22 (0.08)
Arm-I1[8]	42.6 (2.5)	0.14 (0.05)	2.81 (0.20)	0.84 (0.24)	14.0 (0.9)	1.07 (0.28)	31.6 (1.7)	3.07 (0.84)	1.57 (0.12)	0.14 (0.06)	0.37 (0.06)	0.05 (0.02)	<0.01	0.41 (0.04)	1.04 (0.19)
Arm-I2[9]	43.9 (0.7)	0.21 (0.03)	2.99 (0.17)	0.77 (0.09)	14.5 (0.6)	0.72 (0.29)	32.6 (0.6)	1.58 (0.12)	1.29 (0.08)	0.15 (0.04)	0.16 (0.01)	<0.01	<0.01	0.77 (0.07)	0.16 (0.07)
Cyn-I1	51.3 (3.4)	0.18 (0.06)	4.35 (0.16)	0.47 (0.10)	10.4 (1.6)	0.36 (0.03)	26.3 (2.0)	3.18 (0.13)	0.52 (0.03)	0.01 (0.00)	0.02 (0.00)	1.03 (0.03)	1.81 (0.05)	0.02 (0.00)	0.01 (0.00)
Dim-I1[10]	46.7 (1.7)	0.22 (0.08)	2.71 (0.33)	0.68 (0.21)	4.72 (0.72)	0.62 (0.21)	36.7 (1.8)	2.30 (0.56)	0.36 (0.12)	0.44 (0.16)	<0.01	0.95 (0.20)	1.41 (0.33)	1.89 (0.18)	0.30 (0.09)
Etr-I1[11]	48.3	0.18	6.66	0.44	12.9	0.32	22.0	3.59	2.83	0.47	1.69	0.06	0.11	0.25	0.04

	(2.2)	(0.02)	(0.52)	(0.10)	(0.8)	(0.03)	(1.4)	(0.15)	(0.27)	(0.10)	(0.06)	(0.00)	(0.00)	(0.02)	(0.00)
Glk-I1	47.7 (2.2)	0.23 (0.12)	2.87 (0.21)	0.79 (0.15)	14.1 (0.9)	0.49 (0.17)	27.4 (1.1)	2.51 (0.22)	0.85 (0.34)	0.12 (0.05)	0.03 (0.00)	0.59 (0.08)	<0.01	2.15 (0.04)	0.18 (0.01)
Jgo-I1	38.7 (0.5)	0.07 (0.01)	3.87 (0.16)	1.12 (0.05)	13.5 (0.5)	0.48 (0.15)	27.4 (0.4)	1.12 (0.06)	1.53 (0.07)	0.17 (0.04)	0.29 (0.01)	0.49 (0.01)	0.87 (0.02)	8.09 (0.59)	2.25 (0.89)
Khr-I1	41.1 (0.7)	0.07 (0.03)	3.66 (0.21)	0.24 (0.04)	15.1 (1.3)	0.29 (0.09)	34.2 (0.9)	2.58 (0.19)	0.24 (0.10)	0.01 (0.01)	<0.01	0.46 (0.05)	0.79 (0.09)	1.06 (0.09)	0.14 (0.03)
KrC-I1	46.8 (2.0)	0.3 (0.05)	4.92 (0.71)	0.53 (0.12)	13.7 (0.5)	0.38 (0.02)	28.2 (0.9)	3.45 (0.50)	1.31 (0.26)	0.04 (0.02)	<0.01	0.07 (0.01)	<0.01	0.15 (0.01)	0.14 (0.03)
Lut-I1[12]	48.5 (1.7)	0.23 (0.12)	3.81 (0.90)	0.44 (0.17)	9.95 (0.88)	0.18 (0.13)	31.3 (1.2)	2.89 (0.73)	0.82 (0.25)	0.06 (0.06)	0.04 (0.00)	<0.01	<0.01	1.51 (0.01)	0.08 (0.00)
McK-I1[13]	41.0 (0.5)	0.14 (0.05)	3.57 (0.20)	0.34 (0.08)	19.1 (0.3)	0.40 (0.03)	31.0 (0.4)	2.56 (0.26)	0.42 (0.03)	0.02 (0.00)	0.05 (0.02)	0.36 (0.12)	0.52 (0.18)	0.40 (0.02)	0.08 (0.01)
McK-I2[14]	45.5 (1.3)	0.09 (0.09)	3.66 (0.28)	0.77 (0.20)	15.6 (0.7)	0.38 (0.22)	30.3 (0.8)	2.24 (0.24)	0.43 (0.02)	0.03 (0.01)	0.04 (0.00)	0.26 (0.16)	0.46 (0.28)	0.22 (0.00)	0.01 (0.00)
MET-I1[15]	50.2 (0.4)	0.09 (0.02)	2.82 (0.26)	0.70 (0.12)	9.30 (0.84)	0.52 (0.10)	32.6 (0.7)	2.66 (0.32)	0.39 (0.08)	0.02 (0.01)	<0.01	<0.01	<0.01	<0.01	0.64 (0.17)
MET-I2[16]	45.4 (1.1)	0.24 (0.05)	3.19 (0.32)	0.93 (0.17)	7.84 (3.99)	0.55 (0.11)	30.6 (1.3)	2.35 (0.41)	1.42 (0.20)	0.99 (0.17)	<0.01	0.70 (0.01)	1.21 (0.03)	1.85 (0.21)	2.74 (1.68)
MET-I3	46.3 (0.9)	0.02 (0.01)	2.75 (0.28)	0.69 (0.09)	12.9 (1.2)	0.31 (0.03)	31.1 (0.8)	3.66 (0.68)	0.10 (0.02)	0.01 (0.02)	<0.01	0.40 (0.01)	1.23 (0.04)	0.35 (0.01)	0.07 (0.01)
Obl-I1[17]	39.4 (0.8)	0.02 (0.02)	1.12 (0.13)	0.15 (0.06)	24.2 (0.5)	0.45 (0.03)	33.7 (0.6)	0.41 (0.05)	0.48 (0.06)	0.03 (0.01)	0.04 (0.00)	<0.01	<0.01	0.01 (0.00)	0.01 (0.00)
Obl-I2[18]	47.0 (0.6)	0.24 (0.10)	2.06 (0.18)	0.46 (0.12)	15.2 (0.3)	0.42 (0.12)	30.2 (0.2)	1.85 (0.14)	0.83 (0.08)	0.07 (0.03)	0.20 (0.00)	0.25 (0.00)	0.43 (0.00)	0.51 (0.03)	0.39 (0.11)
Par-I1	43.1 (1.2)	0.22 (0.03)	3.29 (0.45)	0.42 (0.03)	15.7 (0.8)	0.27 (0.03)	32.8 (1.1)	3.03 (0.26)	0.13 (0.03)	<0.01	<0.01	0.06 (0.00)	0.11 (0.00)	0.65 (0.02)	0.18 (0.01)
Par-I2	51.5 (2.0)	0.09 (0.01)	1.55 (0.15)	0.66 (0.10)	14.5 (1.0)	0.54 (0.04)	27.3 (1.2)	1.98 (0.20)	0.63 (0.04)	0.02 (0.00)	<0.01	0.27 (0.05)	0.49 (0.09)	0.42 (0.05)	0.05 (0.01)
Par-I3	47.3 (1.5)	0.17 (0.03)	2.82 (0.24)	0.67 (0.06)	17.6 (0.6)	0.40 (0.08)	26.5 (0.9)	2.74 (0.27)	0.25 (0.06)	0.11 (0.04)	<0.01	<0.01	<0.01	1.16 (0.66)	0.27 (0.19)
PVM-I1[19]	42.5 (1.6)	0.06 (0.03)	2.65 (0.18)	0.46 (0.08)	18.6 (0.7)	0.38 (0.05)	30.9 (1.1)	1.45 (0.29)	1.14 (0.08)	0.12 (0.04)	0.15 (0.01)	0.01 (0.00)	0.02 (0.00)	1.41 (0.24)	0.15 (0.06)
QUE-I1[20]	46.8	0.65	10.1	0.83	9.50	0.37	19.8	9.59	1.20	0.19	0.09	0.07	<0.01	0.40	0.31

	(1.3)	(0.11)	(1.2)	(0.28)	(0.70)	(0.04)	(0.6)	(0.80)	(0.18)	(0.07)	(0.04)	(0.04)		(0.01)	(0.08)
QUE-I3[21]	46.6 (1.1)	0.43 (0.09)	6.11 (0.59)	0.76 (0.15)	9.50 (1.10)	0.48 (0.07)	27.9 (1.1)	7.03 (0.50)	0.82 (0.11)	0.03 (0.00)	0.03 (0.01)	0.01 (0.00)	<0.01	<0.01	0.28 (0.11)
QUE-I4[22]	45.5 (0.5)	0.24 (0.09)	4.35 (0.79)	0.68 (0.18)	9.61 (1.31)	0.55 (0.16)	33.7 (1.4)	3.09 (0.59)	0.81 (0.27)	0.11 (0.04)	<0.01	0.10 (0.00)	0.19 (0.00)	0.28 (0.01)	0.65 (0.30)
Rfd-I1[23]	46.7 (1.3)	0.20 (0.04)	5.54 (0.45)	0.48 (0.05)	10.0 (0.5)	0.17 (0.02)	31.8 (0.6)	4.17 (0.48)	0.25 (0.03)	0.01 (0.00)	<0.01	0.15 (0.04)	0.29 (0.07)	0.17 (0.06)	0.05 (0.02)
Rgl-I1	43.6 (2.8)	0.29 (0.12)	3.56 (0.38)	0.54 (0.14)	16.6 (1.6)	0.27 (0.16)	27.0 (2.6)	2.82 (0.43)	1.90 (0.21)	0.34 (0.30)	0.51 (0.15)	0.12 (0.08)	0.21 (0.14)	2.10 (1.12)	0.12 (0.07)
Tdk-I1	47.9 (1.8)	0.14 (0.06)	1.10 (0.17)	0.40 (0.09)	13.0 (0.6)	0.43 (0.06)	34.4 (1.3)	2.19 (0.32)	0.17 (0.03)	0.02 (0.01)	<0.01	0.07 (0.01)	0.13 (0.02)	0.03 (0.00)	0.02 (0.00)
Tdk-I2	51.0 (0.8)	0.11 (0.06)	4.89 (0.62)	0.50 (0.19)	10.6 (0.5)	0.39 (0.07)	28.5 (0.7)	3.50 (0.46)	0.25 (0.04)	<0.01	0.02 (0.00)	<0.01	<0.01	0.18 (0.00)	0.04 (0.00)

*Totals are 100% within rounding errors. ±1σ errors given in parentheses. Fe(s) = Fe in sulfide (troilite), Fe(m) = Fe in metal.

[1] Includes 0.03 ± 0.02 wt% Cl. [2] Includes 0.01 ± 0.00 wt% Cl and 0.01 ± 0.00 wt% F. [3] Includes 0.03 ± 0.01 wt% Cl and 0.02 ± 0.01 wt% F. [4] Includes 0.01 ± 0.00 wt% V_2O_5 and 0.03 ± 0.01 wt% Cl . [5] Includes 0.01 ± 0.01 wt% Cl. [6] Includes 0.01 ± 0.01 wt% V_2O_5. [7] Includes 0.01 ± 0.00 wt% V_2O_5. [8] Includes 0.28 ± 0.12 wt% Cl. Ni value likely an overestimate. [9] Includes 0.17 ± 0.04 wt% Cl. [10] Includes up to 0.07 ± 0.02 wt% Cl, likely an overestimate. [11] Includes 0.01 ± 0.00 wt% V_2O_5, 0.10 ± 0.01 wt% Cl, 0.08 ± 0.00 wt% F. [12] Includes 0.21 ± 0.12 wt% Cl. Experienced alkali-halogen-P-FeO metasomatism. [13,14] Includes 0.01 ± 0.00 wt% Cl. [15,16,21] Ni likely overestimate. [17] Likely unrepresentative composition. [18] Includes 0.02 ± 0.00 wt% Cl. [19] Includes 0.01 ± 0.00 wt% V_2O_5, 0.02 ± 0.00 wt% Cl. [20] K and S values likely overestimates. [22] Includes 0.13 ± 0.04 wt% Cl. Ni likely overestimate. [23] Includes 0.05 ± 0.06 wt% Cl